

假像消除及影像切割應用於生物及醫學影像

研究生：林志陽

指導教授：荊宇泰 博士

國立交通大學

電機資訊學院

資訊科學研究所

摘要

生物或醫學影像處理的計算機方法改進了診斷或研究工作的效能。在這篇論文裡，我們發展了一些計算機演算法，並且發展了解決問題的工具。這些問題包括：從CR影像裡的格狀假像(Grid Artifact)消除，電泳圖像(Gel Electrophoresis)的自動比對，斑點(ELISA Spot)影像的自動分析，及從血管造影影片(Cine Angiogram)中截取冠動脈樹(Coronary Arterial Tree)等。

數位影像更容易儲存及傳送，不過，他們也包含了假像(Artifact)，例如格狀假像和不均勻的照明造成的假像。這些假像是既有(Inheritance)的問題。格狀假像和網紋圖案是使用Grid所引起的。CR的取像平板(Imaging Plate)在X射線曝光期間會使用Grid來除去不想要的散射(Scatter)。當使用顯示器來顯示所取得的影像時，格狀假像或網紋圖案(Moire)的假像就可能會出現。當影像被顯示在一台低解析度的電腦螢幕上時，將使得格狀假像或網紋圖案更加嚴重。因此當影像的判讀必須用普通的電腦螢幕來達成時，這將成為一個大問題。在這篇論文裡，我們詳細探討這些假像造成的原因。研究顯示這些假像的頻率可以從DICOM標籤(Tag)及GRID的規格等訊息直接計算獲得。因此這些假像也就可以從頻率領域來去除。因為被除去的頻率，與解剖結構無關，所以處理過的影像比未處理前更加清楚。此外不均勻照明也造成另一種假像，不均勻照明將造成在物體上的

光線不均勻，這使得在影像處理時，做門檻(Threshold)運算會有問題。因此除去這些照明的不均勻變化是有必要的。影像上的不均勻照明變化，在頻率領域上，是由低頻部分所組成。因此我們設計了一個濾波器來消除這些變化。影像在除去格狀假像及不均勻照明後，將更容易切割(Segmentation)。此外我們也提出切割的方法來切割消除假像之後的影像，如電泳影像和斑點影像等。我們也顯示，對取像時受污染的影像做去除假像的前處理(Preprocessing)，有助於之後的影像處理工作。

消除CR影像的假像，使得影像更加清楚有助於醫療診斷。電泳圖像及斑點影像的自動比對分析，減少生物學家的苦工，增進他們的研究效能。冠狀動脈樹的萃取，提供了分析動脈疾病很有用訊息。



Image Artifacts Removal and Segmentation

Applied to Biomedical Images

Student: Chih-Yang Lin

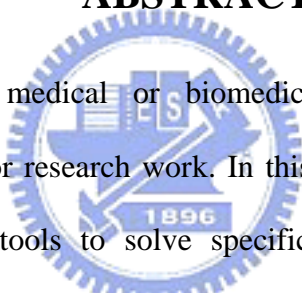
Advisor: Dr. Yu-Tai Ching

Department of Computer and Information Science,

College of Electrical Engineering and Computer Science

National Chiao Tung University

ABSTRACT

The logo of National Chiao Tung University is a circular emblem with a gear-like border. Inside the circle, there is a stylized building and the year '1896' at the bottom. The text 'NCTU' is also visible within the emblem.

Computer methods for medical or biomedical images processing improve the performance of the diagnosis or research work. In this dissertation, we developed computer algorithms and implemented tools to solve specific problems. These problems include removing grid artifacts from Computed Radiograph (CR) images, comparing the lanes in Gel Electrophoresis images, analyzing the ELISA spots images, and extracting the coronary arterial tree from cine angiogram.

Digital CR images are easier to store and transfer from one place to another. However, CR images contain grid artifacts and moiré pattern that are the inheritance problems due to the using of grids to remove scattering. In this dissertation, the causes of these artifacts are investigated in detail. We show that the frequencies of these artifacts are fixed and can be estimated from the DICOM tags and grid specification. The artifacts can then be removed in the frequency domain. Because the removed frequency does not relate to the anatomical structure, the resulting images are clearer than before.

Variable illumination is another kind of artifacts. Variable illumination artifact occurs

when the ELISA Spots images were taken. This artifact causes a problem that the intensity threshold cannot be applied. In this dissertation, we design a filter to eliminate such variation. A sequence of image processing techniques is then applied to segment the ELISA spots. A tool was implemented based on the algorithm. This work helps to save biologist efforts in analyzing the ELISA spots image.

Grid artifacts also occur in Gel Electrophoresis image. Gel Electrophoresis is an important tool in biology research area. To identify the same lane pattern is the goal. In this dissertation, we remove the artifacts before segmentation process are applied. We then convert a lane into the position vector for comparison. The presented method could reach 97% accuracy and thus save research effort of the biologist.

The last work we studied was to segment the coronary arterial tree from cine angiogram. The artifacts were the backgrounds such as ribs and lung texture. We proposed to eliminate the backgrounds in time direction. Matched filter and wavelet techniques were then applied to segment the arterial tree. GVF snake is then applied to calculate the width of the vessel. The segmented arterial tree is fairly complete and the calculated width is accurate.

ACKNOWLEDGMENTS

I would like to express my sincere appreciation to my advisors, Professor Yu-Tai Ching, for their kind patience and guidance throughout the course of this dissertation as well as the invaluable training during my study. Thanks are also due to Doctor Wen-Jeng Lee, Professor Yun-Liang Yang, Professor Betty A.Wu-Hsieh, and Professor James Chen for their helpful discussions and suggestions. Special appreciation is given to father-in-law and mother-in-law for marrying me their treasure daughter at this moment. I am deeply grateful in my heart for my wife's support and encouragement for many years. I also deeply appreciate the assistance from the colleagues in the Department of Electrical Engineer at Ta-Hwa Institute of Technology.

Finally, I would dedicate this dissertation to my parents and my wife and thank them for their encouragement, support, and love.

本篇論文得以完成，首先要感謝我的指導教授荊宇泰老師多年來的悉心指導及研究訓練，也要感謝李文正醫師，楊昀良老師，伍安怡老師及陳序勇老師的幫忙及建議，再來要感謝父母親及家人的鼓勵支持，尤其母親總是適時地給予關愛及支持。從碩士到博士多年的研究生生涯裡，也歷經了經濟最拮据的時期，感謝妹妹-修華總是適時地伸出援手，讓我無後顧之憂，得以專心於學業上。也感謝我的岳父-周敬南先生及岳母-周林含笑女士，願意在此時將他們的寶貝女兒嫁給我。內人多年來默默的支持及鼓勵更是銘感於心。

感謝大華技術學院電機系盧豐彰主任、謝振中主任、謝劍書主任、江士貞小姐及同仁們，在工作上諸多幫忙及支持，讓我有較多的時間能專心於學業上。也感謝所有關心愛護我的師長及朋友：林芳甫叔叔、簡素香老師、家源、亭君、亭瑩、世瑋、靜瑩 等。要感謝的人實在是很多，無法一一列出，最重要的是要感謝佛菩薩的庇祐讓我生活順遂所做皆辦。

謹將本論文獻給我敬愛的父親-林吉郎先生、母親-呂惠堅女士、內人-周淑媛小姐及妹妹-林修華小姐。

TABLE OF CONTENTS

ABSTRACT IN CHINESE	I
ABSTRACT IN ENGLISH	III
ACKNOWLEDGMENTS	V
TABLE OF CONTENTS	VI
LIST OF FIGURES	IX
LIST OF TABLES	XIV
CHAPTER 1 INTRODUCTION	1
1. MOTIVATION.....	2
2. RELATED STUDIES.....	4
2.1 Literature Review of Grid Artifacts Elimination in Computed Radiographic Images.....	4
2.2 Literature Review of Spot Segmentation	6
2.3 Literature Review of Extraction of Coronary Arterial Tree	6
3. OVERVIEW OF THE PROPOSED METHODS.....	7
3.1 Grid Artifacts Elimination in Computed Radiographic Images	7
3.2 An Automatic Method to Compare the Lanes in Gel Electrophoresis (GE) Images....	7
3.3 A Computer Method for ELISA Spot Assay Analysis.....	8
3.4 Extraction of Coronary Arterial Tree Using Cine X-Ray Angiograms	8
4. DISSERTATION ORGANIZATION.....	8
CHAPTER 2 A STUDY OF GRID ARTIFACTS FORMATION AND ELIMINATION IN COMPUTED RADIOGRAPHIC IMAGES	10

1. INTRODUCTION	11
2. THEORY	12
2.1 Case 1, $\theta = 0$	16
2.2 Case 2, $\theta \neq 0$, The Moiré Pattern	20
2.3 Displaying an Image Containing Artifacts on a Monitor	22
3. METHODS	23
3.1 Estimating the Artifact Frequency	23
3.2 Locating the Frequency f_{t_i} :	24
3.3 Remove the Frequency:	25
4. RESULTS	26
4.1 FROC Study	37
5. CONCLUSIONS AND DISCUSSION	39
CHAPTER 3 AN AUTOMATIC METHOD TO COMPARE THE LANES IN GEL ELECTROPHORESIS (GE) IMAGES	41
1. INTRODUCTION	41
2. METHOD	43
2.1 Background Removal	43
2.2 Lanes and Bands Identification	49
2.3 Calculate the Lane Position Vectors	57
2.4 Position Vectors Normalization	62
3. RESULTS	64
CHAPTER 4 A COMPUTER METHOD FOR ELISA SPOT ASSAY ANALYSIS	74
1. INTRODUCTION	74
2. METHOD	76

2.1 Variable Illumination Removal.....	77
2.2 Color Space Conversion	79
2.3 Train the System and Obtain an Image of the Color Differences.....	80
2.4 Matched Filter for Spots Segmentation	81
2.5 Compute the Binary Image.....	83
3. A SOFTWARE TOOL	84
4. RESULTS	84
5. CONCLUSIONS	86
CHAPTER 5 EXTRACTION OF CORONARY ARTERIAL TREE USING CINE	
X-RAY ANGIOGRAMS.....	89
1. INTRODUCTION	89
2. METHODS.....	91
3. RESULTS	103
4. CONCLUSION	104
APPENDIX	1
1. Grid Artifacts Removal Using Bucky.....	1
REFERENCES	1
VITA	1
PUBLICATION LIST OF CHIH-YANG LIN	1



LIST OF FIGURES

Fig. 2-1. An X-ray imaging system. The X-ray passes through the patient and is collimated by the grid to eliminate the scattering effect.	13
Fig. 2-2. (a) Vertical grid artifacts. (b) Horizontal grid artifacts. (c) Crisscross grid artifacts.	13
Fig. 2-3. This figure shows the cross section of a grid, and some grid specifications related to this work.	15
Fig. 2-4. There is an angle θ between the sampling signal (UV -coordinate) and the grid (XY -coordinate).....	16
Fig. 2-5. Along a horizontal scan line, the vertical stripe signal is a square wave.....	17
Fig. 2-6. A low frequency aliasing occurs (the wave plotted as a bold curve).....	18
Fig. 2-7. Moiré pattern caused by two periodical functions.....	21
Fig. 2-8. A change in an angle θ from 0° to 2° will cause the stripe angle in the moiré pattern to change from 0° to 24°	22
Fig. 2-9. (a) Mammography Quality Control Phantom (Phantom No.C104, Fuji, Japan) image with grid artifacts. (b) A selected region in (a) is shown in the original resolution. The artifacts are easily seen. (c) The same region, with grid artifacts eliminated. Note that many details such as the vertical stripes can be clearly distinguished. (d) The spectrum of a 1D Fourier transform of the image shown in (a). The y-axis is logarithmic. The frequency of the grid artifact is highlighted with a circle. (e) The spectrum after grid artifacts are removed. (f) An image of the Mammography Quality Control Phantom scaled down 17% to a resolution of 540 by 658 pixels. It shows a very serious artifact (the moiré pattern). (g) The moiré pattern was eliminated using the proposed method.....	31
Fig. 2-10. (a) A patient with left lower lobe consolidation due to pneumonia. Grid pattern can be seen on CR chest image (b) The portion that is highlighted in white in (a). (c) The grid	

pattern was removed using the proposed method. (d) The spectrum of a 1D Fourier transform of the image shown in (a). The y-axis is logarithmic. The frequency of the grid artifact is highlighted with a circle. (e) The spectrum after grid artifacts are removed. ...34

Fig. 2-11 . (a) The original image with grid textures. (b) The grid textures were removed using the proposed method. (c) The grid textures were removed using the blur kernel proposed by Barski. (d) The grid pattern was removed using a notch filter proposed by Belykh... 36

Fig. 2-12. The portion of the mammography quality control phantom used to evaluate observers' performance.....37

Fig. 2-13. The FROC curves for the observers studying the original image size. Observers could achieve perfect performance regardless of the presence of the grid lines.38

Fig. 2-14. The FROC curves for observers studying reduced-size images. The performance is better when the grid lines are removed.....39

Fig. 3-1. The imaging system, there is a grid between the CCD camera and the gel box.....43

Fig. 3-2. The grid collimates the light.....44

Fig. 3-3. (a) Original image. (b) Zoom in an area of the original image. (c) After removing the grid. (d) The same zoom in area with the grid-texture removed.46

Fig. 3-4. (a) The spectrum of $f(x,y)$. There are two peaks within the two pairs of red lines. The gray scale is logarithmic for visualization purposes. (b) Histogram of $f(x,y)$ (c) Spectrum after eliminating the grid-texture frequency. The gray scale is also logarithmic. (d) Histogram after eliminating the grid-texture.48

Fig. 3-5. An image after background removal.....49

Fig. 3-6. The intensity profile of the scan line for a lane50

Fig. 3-7. The result from applying the matched filters.....52

Fig. 3-8. The intensity profile of a lane scan line after filter matching54

Fig. 3-9. The watershed algorithm.....54

Fig. 3-10. Result from applying the 1-D watershed segmentation algorithm to Fig. 3-7. The break-points are highlighted in the red circles.	55
Fig. 3-11. (a) Vertical projection of the points in Fig. 3-10. (b) Horizontal projection of the points in Fig. 3-10.....	56
Fig. 3-12. The result of segmentation of lanes.	57
Fig. 3-13. The end point detection masks.....	58
Fig. 3-14. (a) Skeleton of a band. (b) Dilation of (a).....	59
Fig. 3-15. Broken band result from recovering and removing the areas that are not in the lanes.	60
Fig. 3-16. Final segmented bands and lanes.....	61
Fig. 3-17. The result is shown superimposed on the original image.....	61
Fig. 3-18. Three vector removal results shown using a green bar superimposed onto the original image.	66
Fig. 3-19. (a) Original Image (b) Result from applying a time-variant matched filter (c) Result from applying the 1-D watershed segmentation algorithm to (b). (d) Final Segmented Bands and Lanes. (e) The result is shown superimposed onto the original image.....	69
Fig.3-20. A report generated by the proposed method	70
Fig. 3-21. The software system shows the differences between the selected lane and the other lanes in the images. (a) Using the mouse to select lane 5. (b) Lane 3 is identical to lane 5 in (a). (c) Lane 6 is also identical to lane 5 in (a)	73
Fig. 3-22. A screen shot from the developed software system.	73
Fig. 4-1. The pseudo code for the proposed method	77
Fig. 4-2 (a) The high-pass filter spectrum. (b) A cross-section of the high-pass filter as a function of the polar angle and frequency. In these figures $r = \sqrt{\omega_x + \omega_y}$, $r_L = 1/(1 + e^{s\omega_0})$, and $r_H = 1 + A$	78

Fig. 4-3 (a) A portion of the color difference map. The white line denotes a cross section. (b) The gray-level profiles of the cross section in (a). The x -coordinate denotes the pixels along the cross section. The y -coordinate denotes the gray-level.	82
Fig. 4-4. 2-D matched filters used in our proposed method. The radius size is (a) 4, and (b) 8.	83
Fig. 4-5. (a) The original image. (b) Image after applying the Sobel filter. (c) After circle detection. (d) Remove the region outside the circle.	87
Fig. 4-6. A screenshot of the software system.	87
Fig. 4-7. First row, the three tested images from the proposed method. Second row, the color difference maps. In these images, the pixels with less difference are shown in the brighter intensity. Third row, the results after applying the matched filters. The 4 th row, the final results. The last row, the original images overlying the results obtained in the images shown in 4 th	88
Fig. 5-1. Multi-level wavelet (a) decomposition and (b) reconstruction for a 1-D case.	94
Fig. 5-2. A 2-D 3-stage discrete wavelet transformation.	95
Fig. 5-3. A 3-D 3-stage discrete wavelet transformation.	96
Fig. 5-4. Six matched filters ($\sigma = 1, 2, \dots, \text{and } 6$) with zero orientation.	99
Fig. 5-5. (a) The cine angiograms of a left coronary artery (LCA). (b) The cine angiograms of a right coronary artery (RCA).	105
Fig. 5-6. The typical example of one frame in the cine angiograms of Fig. 5-5 (a).	105
Fig. 5-7. One of the resultant images after the background removal process.	106
Fig. 5-8. The resultant image after applying the DWT de-noise process and applying the matched filter.	106
Fig. 5-9. The resultant binary image after the 2-D stencil masking process where the black pixel is denoted by zero and the white pixel is denoted by 1.	107

Fig. 5-10. The projection onto xyt -plane along θ -axis	107
Fig. 5-11. The final segmentation results on a sequence of X-ray angiographic images on Fig. 5-5.....	108
Fig. 5-12. Two segmented results. (a) The last image in Fig. 5-11 (a). (b) The last image in Fig. 5-11 (b).	109
Fig. 5-13. The original images are overlying the results obtained in Fig. 5-12.	110
Fig. 5-14. The magnitude of GVF in Fig. 5-12 (b).....	111
Fig. 5-15. Initial snake for finding the medial axis of vessel.	112
Fig. 5-16. The result of the centerline of vessel with widths for some selected points on the medial axis marked.....	112



LIST OF TABLES

Table 4-1. The important statistical values..... 85

Table 4-2. Comparison of our inspection method and human..... 85

Table 5-1. Values of the Gaussian Function 97



CHAPTER 1

INTRODUCTION

Computer methods for medical or biomedical images analysis are helpful for diagnosis or researches in biomedical area. In this dissertation, we design computer methods for different applications. We have:

1. Designed and implemented a tool for artifacts removal in computed radiograph (CR) image,
2. Designed and implemented a tool for comparing lanes in gel electrophoresis images,
3. Designed and implemented a tool for analyzing the ELISA spot images,
4. Designed an algorithm to extract the coronary arterial tree from cine angiogram.

There are grid artifacts in CR image. The artifacts are contaminated in the imaging system. The grid artifacts could be a more serious problem when displaying the images in a low-resolution computer terminal. We carefully studied the causes of the artifact and design an algorithm to eliminate the artifacts.

Gel electrophoresis is an important tool in the area of biology research. An image consists of 7 to 10 "lanes". Each lane is a fragment of DNA that represented as several "bands". Two lanes (DNA fragments) are considered the same if these two lanes have the same pattern. Biologists using this tool could have hundreds of images and they are looking for the identical lanes from the images. We developed a tool that converts a lane into a "position vector". A position vector is a set of integers representing the location of the band in the lane. Comparing the lane becomes comparing the position vector.

ELISA spot assay is also an important tool in the research area of biology. The experiment ends up with analyzing an image. The image is a color image that containing spots in it. Biologist needs to calculate the number of the spots, the mean and the standard deviation

of the spots. This is a tedious and time-consuming task. We have developed a tool to accurately obtain the required statistics for the biologist.

Coronary artery narrowing is one of the major heart diseases that cause death of the human. Angiogram is still the most important tool for the diagnosis of the narrowing of the vessel. It is important to segment the vessel from the image and estimate the width of the vessel. In this work, we propose to eliminate the background by using the temporal information available in cine angiogram. Followed by a sequence of steps, we can accurately compute the width of the vessel.

In this dissertation, we report that factors in images formation step are important to the image-processing step. In CR image and gel electrophoresis images formation, grids were used to remove scattering effect. In ELISA spot image, illumination changes over the images because the light source could not be in the top of the sample. Removing these factors could achieve the best segmentation results. We also report that "cocktail approach" could reach the best processing results.



In the rest of this chapter, the motivations are first introduced in Section 1. In Section 2, we shall review the previous researches in these areas. In Section 3, we present the overview of the proposed methods. The organization of this dissertation is stated in Section 4.

1. MOTIVATION

Very often, there are artifacts in the medical or biology system which are caused in the very beginning of the imaging system. Grid artifact appeared in Computed radiography (CR) and biology images are an example. Computed radiography (CR) has many advantages such as filmless operations, efficiency and convenience. Furthermore, it is easier to integrate with the picture archiving and communication systems (PACS). Another important advantage is that CR images generally have wider dynamic range than conventional screen film.

Unfortunately, grid artifacts and moiré pattern artifacts may be present in CR images. These artifacts become a more serious problem when displaying CR images on a computer monitor for softcopy diagnosis. Using a grid with higher frequency or a Potter-Bucky grid (i.e., a moving grid, Bucky for short) can reduce occurrence but not guarantee elimination of these artifacts.

Another artifacts example is the Gel electrophoresis (GE) in DNA or protein related research. GE image also contains grid artifact and needs to be remove like CR image for the purpose of application of the computer method. Gel electrophoresis (GE) was developed as a means for resolving biological macromolecules, such as DNA, RNA, and protein molecules [24]. There are several different types of GE based on their resolution ranges. One major application of GE is to separate DNA molecules from 0.5 kbp to approximately 10 Mbp. GE is an invaluable tool for gene and genomic analysis and it is routinely used in many applications, such as gene identification, isolation, and purification. GE is used in various fields like biology, molecular biology, biochemistry, biotechnology, medicine and clinical diagnosis.

The third research topic of this dissertation is the segmentation of the ELISA (Enzyme-Linked Immuno-sorbent Assay) Spot Assay image. The ELISA Spot Assay is a method widely used by immunologists to enumerate cytokine-producing cells within a specific cell population. The ELISA results are presented in an image containing numerous colored spots. The ELISA Spot Assay is designed to detect cells that produce cytokines. Cytokines are proteins readily secreted by immune cells upon stimulation by the antigens they recognize or by mitogens. The experimental steps are described as follows. Test wells are coated with anti-cytokine antibody (capturing antibody) before the cells are added. A certain number of cells and antigen are added to the pre-coated wells. During incubation, the cells are stimulated to secrete cytokine. The precoated antibody captures the secreted cytokine.

After washing, a biotinylated secondary anti-cytokine antibody (detecting antibody that recognizes different epitopes on the cytokine from the capturing antibody) and enzyme-avidin complex are added in sequence. A color reaction (red in this case) specific to cytokine-secreting cells occurs as a result of this enzymatic reaction. Each red spot represents one cytokine-secreting cell. To analyze ELISA Spot Assay results, immunologists must know the numbers of spots, the distribution and size of the spots, and the mean and standard deviation of the spot sizes. Because these spots can number in the hundreds in each 70 mm diameter well, counting the spots is labor-intensive work even when one uses a dissecting microscope. To overcome this problem, a computer method, that helps immunologists calculate the important spot statistical values, is needed.

The forth research topic of this dissertation is the Extraction of Coronary Arterial Tree Using Cine X-Ray Angiograms. Coronary angiography is still the most common modality for physicians to assess the severity of vessel narrowing or stenosis during percutaneous coronary intervention procedure. Accurate quantitative analysis of coronary arteries in digital angiographic images is valuable and important to clinical needs. Computer-assisted extraction of a set of major arteries or the entire coronary arterial tree from two-dimensional (2-D) angiograms is regarded as a crucial process. Once the vessels are identified, additional techniques may be applied to obtain quantitative information including severity of stenosis, three-dimensional representation of the vascular tree, motion analysis of the coronary arteries, or blood-flow analysis

2. RELATED STUDIES

In this section, we review some related techniques.

2.1 Literature Review of Grid Artifacts Elimination in Computed Radiographic Images

In a study by Cesar, et al., [1] the authors presented a detailed discussion that focused on

some artifacts that were caused by operator error. However, there are other types of artifacts, such as grid artifacts and moiré patterns, that are not caused by operator error. These artifacts are inherent problems with the CR imaging system. A grid is used routinely during X-ray exposure to remove undesired scattered X-rays. When the CR image plate is exposed with a grid and displayed on a computer monitor, interference or moiré pattern artifacts appear. The grid artifacts and moiré patterns are much more pronounced when the images are displayed on a computer monitor which resolution is lower than the images'.

Previous similar works can be found in several other grid pattern studies [2, 3, 4, 5]. A similar problem in designing a film scanner was studied by Wang and Huang [2]. The objective of the study was to minimize the aliasing artifacts while converting a film into digital form. In another study by Barski and Wang [3], a method consisting of grid frequency detection and adaptive grid suppression was proposed. The grid artifact frequency was detected in the frequency domain after a 1D Fourier Transform. The artifact suppression was achieved by designing appropriate blur kernels in the spatial domain. The artifact frequency in 95.8% of the cases could be correctly detected. However, some images that did not contain grid artifacts were identified incorrectly as containing artifact frequencies. Since a grid artifact is a periodical signal, it cannot be effectively removed by applying simple blur kernels in the spatial domain. Moreover, applying blur kernels to reduce grid artifacts also blurs the image itself. In a grid artifact study by Belykh and Cornelius [4], the same method used Barski and Wang [3] was used to detect grid frequency. A notch filter [6] in the frequency domain was used to suppress the grid textures. Unfortunately, using a notch filter causes rippling or ringing effects. Sasada, et al [5], used a method similar to that by Barski and Wang [3] to locate the artifact frequency. The wavelet approach was then employed to remove grid artifacts. None of these studies evaluated any observers' performance after the grid artifacts were removed.

2.2 Literature Review of Spot Segmentation

Previous related works can be found in [39-40]. In [39], an automatic method for particle detection from electron micrographs was proposed. Distance transform and the Voronoi diagram were used for detection of critical features as well as for accurate location of particles from the images or micrographs. The method could only find fixed size disks. In our case, size of spots is not fixed. In [41], an automatic circular decomposition algorithm applied to blood cells image was proposed. The method used polygonal approximation, curve segmentation, circle modeling, circle adapting, and circle merging to find various sizes of circles. The method needed edge detection as the first step for preprocessing. Unfortunately, in most of the cases, spots do not have obvious edge. In [42], automatic particle detection through efficient Hough transforms was proposed. The method could find various size circles. Nevertheless, this method also needed edge detection before the Hough transform can be applied. In [40] a clustering-based method for particle detection is proposed. This method used a clustering-based method based on the gravitation to classify discrete points into a particle. It worked quite well for detecting particles from images with very low SNR. Before running the clustering algorithm, intensity thresholding is required. Since the boundaries for the spots are not clear, an appropriate threshold value is hard to determine.

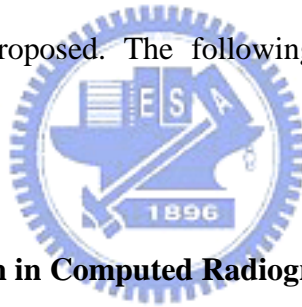
2.3 Literature Review of Extraction of Coronary Arterial Tree

Traditional signal-based edge detection algorithms [69-75] were unable to effectively or accurately detect the desired structures. The existing methods specific to vessel extraction can be categorized into (i) model-based [76-78] (ii) tracking-based [79-81], (iii) classifier-based [82], and (iv) filter-based [83-85] techniques. In model-based methods, the coronary arterial tree is produced based on a pre-defined coronary artery model in the form of a “graph” structure. In tracking-based methods, the process proceeds with an initial

start-of-search location followed by an automatic tracking process by exploiting the spatial continuity of the vessel's centerline, orientation, diameter, and density. In classifier-based methods, a clustering algorithm is employed with properly preprocessed data to differentiate vessel or non-vessel regions. In filter-based methods, the coronary arteries are enhanced and located so that they can be subsequently detected in the image.

3. OVERVIEW OF THE PROPOSED METHODS

In this dissertation, we first study the grid artifacts formation and elimination. We proposed an automatic method to compare the lanes in Gel Electrophoresis (GE) images and propose a computer method for ELISA spot assay analysis. An efficient and robust method for identification of coronary arteries and evaluation of the severity of the stenosis on the routine X-ray angiograms are also proposed. The following subsections briefly introduce these methods.



3.1 Grid Artifacts Elimination in Computed Radiographic Images

We studied the formation of the artifacts. We show that the grid artifacts correspond to a narrow band of frequency in the frequency domain. The frequency can be predetermined, accurately located and thus removed from the frequency domain.

3.2 An Automatic Method to Compare the Lanes in Gel Electrophoresis (GE) Images

We present a computer method designed to compare the lanes and identify identical lanes. This segmentation method, developed using many image-processing techniques, is applied to extract the lanes and bands in GE images. The lanes are then converted into “position vectors” that describe the positions of the bands. This method can accurately identify identical lanes, helping biologists to identify the identical lanes from many lanes with much less effort.

3.3 A Computer Method for ELISA Spot Assay Analysis

We present a method to identify the spots in the image and report on important statistics regarding the spots in the image. The proposed method employs color analysis in the CIE $L^*u^*v^*$ color space and matched filter technique. The system is trained to obtain a standard color for the spots and calculate the color differences between the spots and background in the $L^*u^*v^*$ space. Matched filters are then used to remove noise and enhance the spots in the color difference map. Intensity thresholding is applied to obtain a binary image in which the pixels in the spots have a gray scale of 1 while the gray scale of the other pixels is depicted as 0.

3.4 Extraction of Coronary Arterial Tree Using Cine X-Ray Angiograms

The proposed method consists of two major stages: (a) signal-based image segmentation and (b) vessel feature extraction. The 3D Fourier and 3D Wavelet transforms are first employed to reduce the background and noisy structures in the images. Afterwards, a set of matched filters was applied to enhance the coronary arteries in the images. At the end, clustering analysis, histogram technique, and size filtering were utilized to obtain a binary image that consists of the final segmented coronary arterial tree. To extract vessel features in terms of vessel centerline and diameter, a gradient vector-flow based snake algorithm is applied to determine the medial axis of a vessel followed by the calculations of vessel boundaries and width associated with the detected medial axis.

4. DISSERTATION ORGANIZATION

In the remainder of the dissertation, “A Study of Grid Artifacts Formation and Elimination in Computed Radiographic Images” is presented in Chapter 2. “An Automatic Method to Compare the Lanes in Gel Electrophoresis (GE) Images” is proposed in Chapter 3. In Chapter 4, we propose “A Computer Method for ELISA Spot Assay Analysis”. “Extraction

of Coronary Arterial Tree Using Cine X-Ray Angiograms” is proposed in Chapter 5. Finally, the conclusions and suggestions for future works appear in Chapter 6.



CHAPTER 2

A Study of Grid Artifacts Formation and Elimination in Computed Radiographic Images

Computed radiography (CR) has many advantages such as filmless operations, efficiency and convenience. Furthermore, it is easier to integrate with the picture archiving and communication systems (PACS). Another important advantage is that CR images generally have wider dynamic range than conventional screen film. Unfortunately, grid artifacts and moiré pattern artifacts may be present in CR images. These artifacts become a more serious problem when displaying CR images on a monitor for softcopy diagnosis if the monitor does not have high enough resolution. Using a grid with higher frequency or a Potter-Bucky grid (i.e., a moving grid, Bucky for short) can reduce occurrence but not guarantee elimination of these artifacts. In this chapter, the formation of the artifacts is studied. We show that the grid artifacts correspond to a narrow band of frequency in the frequency domain. The frequency can be determined, accurately located and thus removed from the frequency domain. The Free-Response Receiver Operating Characteristic (FROC) experiment was performed to evaluate the performance of the observers when the artifacts are removed. The results show that observers can achieve perfect performance regardless of the presence of artifacts when full size images are available. However, if a reduced image size is required, the observers' performance is improved when the artifacts are removed. Comparing the results obtained from the proposed method against the results obtained using previous computer methods. Our method can achieve better image quality.

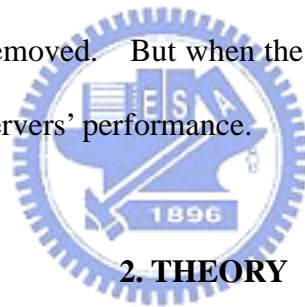
1. INTRODUCTION

The PACS system has become a hospital standard. In a PACS system, the clinical images are presented in digital form. Digital images are easier to store and transfer from one place to another. However, they also contain artifacts. In a study by Cesar, et al., [1] the authors presented a detailed discussion that focused on some artifacts that were caused by operator error. However, there are other types of artifacts, such as grid artifacts and moiré patterns, that are not caused by operator error. These artifacts are inherent problems with the CR imaging system. A grid is used routinely during X-ray exposure to remove undesired scattered X-rays. When the CR image plate is exposed with a grid and displayed on a computer monitor, interference or moiré pattern artifacts appear. The grid artifacts and moiré patterns are much more pronounced when the images are displayed on a computer monitor which resolution is lower than the images'.

Previous similar works can be found in several other grid pattern studies [2, 3, 4, 5]. A similar problem in designing a film scanner was studied by Wang and Huang [2]. The objective of the study was to minimize the aliasing artifacts while converting a film into digital form. In another study by Barski and Wang [3], a method consisting of grid frequency detection and adaptive grid suppression was proposed. The grid artifact frequency was detected in the frequency domain after a 1D Fourier Transform. The artifact suppression was achieved by designing appropriate blur kernels in the spatial domain. The artifact frequency in 95.8% of the cases could be correctly detected. However, some images that did not contain grid artifacts were identified incorrectly as containing artifact frequencies. Since a grid artifact is a periodical signal, it cannot be effectively removed by applying simple blur kernels in the spatial domain. Moreover, applying blur kernels to reduce grid artifacts also blurs the image itself. In a grid artifact study by Belykh and Cornelius [4], the same method used Barski and Wang [3] was used to detect grid frequency. A notch filter [6] in the

frequency domain was used to suppress the grid textures. Unfortunately, using a notch filter causes rippling or ringing effects. Sasada, et al [5], used a method similar to that by Barski and Wang [3] to locate the artifact frequency. The wavelet approach was then employed to remove grid artifacts. None of these studies evaluated any observers' performance after the grid artifacts were removed.

In this chapter, the causes of grid artifacts are investigated in detail. We show that the artifact frequency can be estimated directly from the DICOM tag and grid specifications. The frequency can be accurately located in the frequency domain. Finally, a band-stop Gaussian filter is designed to remove the frequency. The FROC test [7] is used to evaluate the observers' performance when the grid artifacts are removed. The results show that observers could achieve perfect performance when full size images were available, regardless of whether the artifacts were removed. But when the image sizes are reduced, removing the grid artifacts improves the observers' performance.



2. THEORY

There are two major X-ray scattering effects, Rayleigh scattering and Compton scattering, that affect the quality of an X-ray image [7]. Scattering is a very complex phenomenon. A grid is employed to eliminate or reduce scattering. In Fig. 2-1, both the collimator and the grid serve to limit the scattered photons from striking the imaging plate. Using the grid improves the sharpness of the CR images.

A variety of X-ray grids are available [8]. Different grids produce different grid textures in the image plate. These grid textures can be vertical stripes, horizontal stripes, or a combination of the two, as shown in Fig. 2-2. In this chapter, only the case of vertical stripes is discussed. The other two cases are similar.

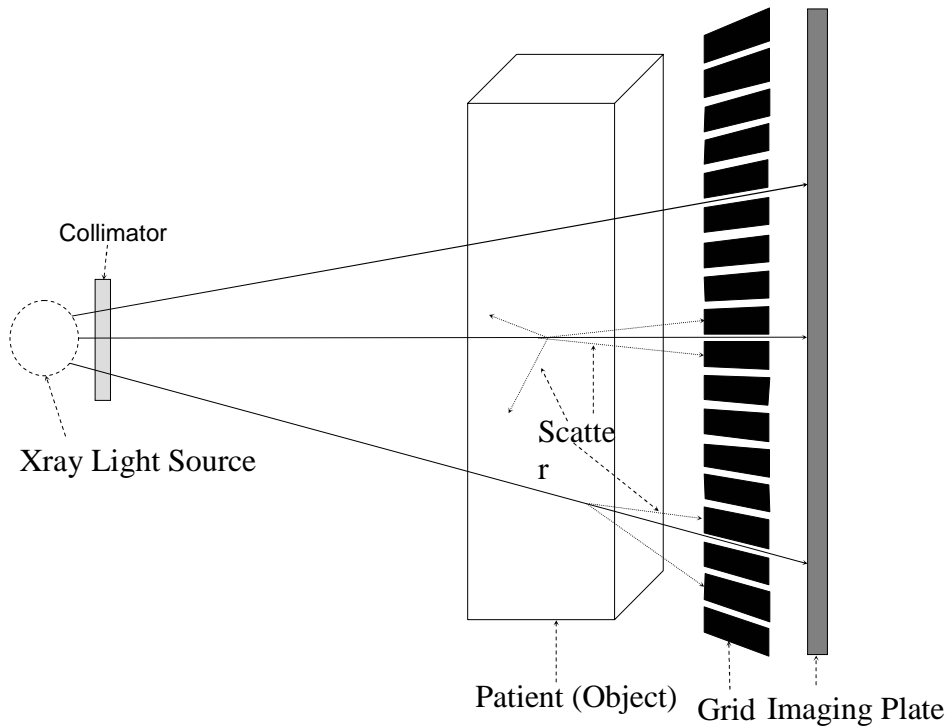


Fig. 2-1. An X-ray imaging system. The X-ray passes through the patient and is collimated by the grid to eliminate the scattering effect.

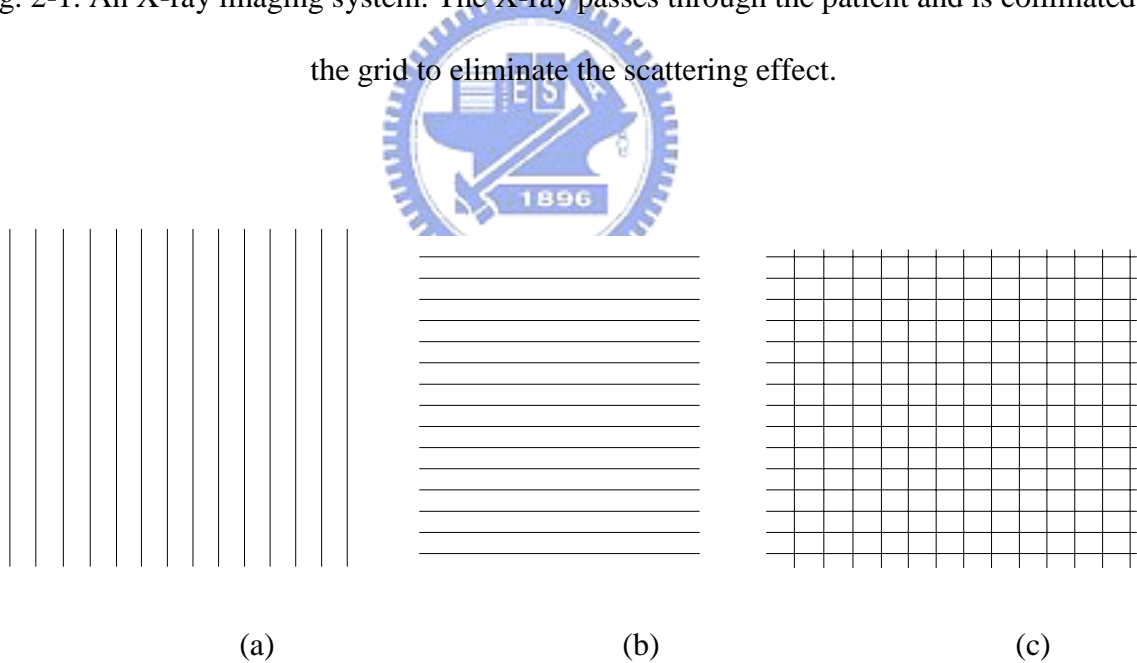


Fig. 2-2. (a) Vertical grid artifacts. (b) Horizontal grid artifacts. (c) Crisscross grid artifacts.

A CR image is recorded by an imaging plate coated with photostimulated storage phosphors [9-12]. When the coating is exposed to X-rays, the electrons in the phosphor crystals are excited and trapped in a semi-stable, higher-energy state. To read this energy

state, a plate reader scans the imaging plate using a laser beam [9]. The laser energy releases the trapped electrons, causing emitted visible light that is captured and converted into pixels in the digital image. Suppose that there are vertical stripes recorded in the image plate, and the vertical stripes are sampled by sampling signal $g_s(u, v)$. Interference between the two signals occurs.

There are two points on the path from the image formation to the display in a raster device at which artifacts occur. The first point is demonstrated by sampling the image plate containing grid texture patterns by using a plate reader. We show that the artifacts are either the grid texture itself or the interference between the grid texture and the plate reader sampling signal. The second point is demonstrated by outputting an image containing artifacts to a raster output device. In this situation, the artifacts are sampled by the pixels of the output device again, so that more serious artifacts are produced.

Fig. 2-3 shows some important grid parameters related to the interference between the two signals. The grid frequency, denoted as f_{grid} , is expressed as the number of lines per centimeter (or per inch). T_{grid} is the distance between consecutive vertical stripes. Thus $T_{grid} = 1/f_{grid}$. As the frequency becomes higher, the grids become thinner and there is less grid texture obstruction in the image. Most of the grids have an f_{grid} between 80 and 152 lines per inch. Two less important parameters to this work are the space between the lead stripes, d and the thickness of lead, s . Note that $T_{grid} = s + d$.

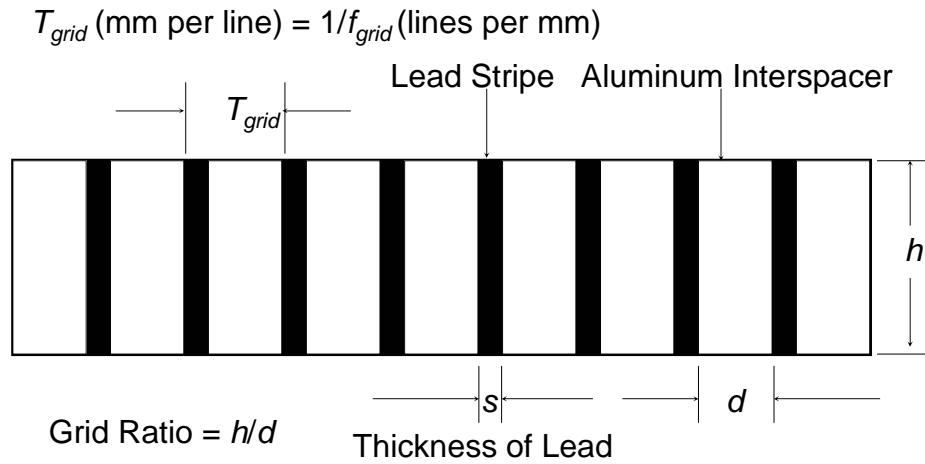


Fig. 2-3. This figure shows the cross section of a grid, and some grid specifications related to this work.

Given a 2D signal $h_g(x, y)$ in an XY -coordinate system, the signal is sampled by a grid function $g_s(u, v)$ in the UV -coordinate system. Consider the case in which $h_g(x, y)$ consists of vertical stripes in the XY -coordinates. Depending on the angle, θ , between the XY - and UV - coordinate systems, there are two cases. The first case is that the XY -coordinate coincides with the UV -coordinate, i.e., $\theta=0$. The second case involves a nonzero angle θ between the XY -coordinates and the UV -coordinates (Fig. 2-4).

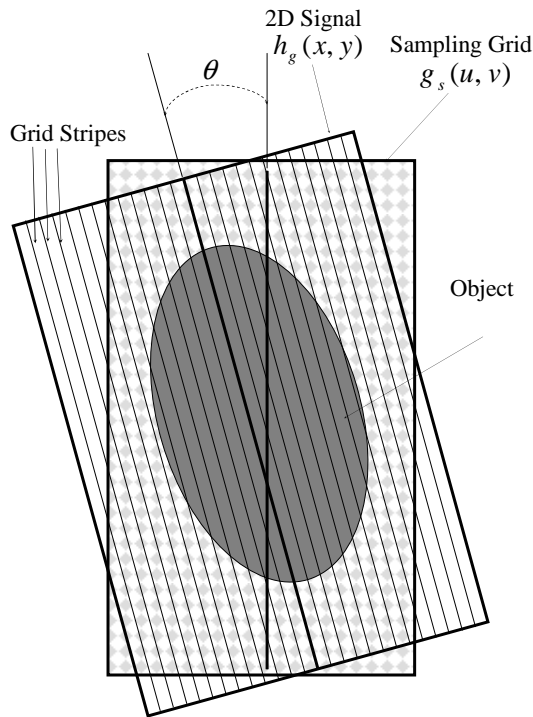


Fig. 2-4. There is an angle θ between the sampling signal (UV -coordinate) and the grid (XY -coordinate).



2.1 Case 1, $\theta = 0$

If the XY -coordinate coincides with the UV -coordinate, only the sampling signal along a horizontal line is considered. Along a horizontal sampling line, the vertical stripe signal is a square wave, as shown in Fig. 2-5. Let the 1D square wave be denoted $h_g(x)$. Recall that T_{grid} is the period of $h_g(x)$, and d and s are, respectively, the space between the lead stripes and the thickness of lead. We have $h_g(x + T_{grid}) = h_g(x)$ and

$$h_g(x) = \begin{cases} 1, & -\frac{d}{2} \leq x \leq \frac{d}{2} \\ 0, & -\frac{s}{2} - \frac{d}{2} < x < -\frac{d}{2} \quad \text{or} \quad \frac{d}{2} < x < \frac{d}{2} + \frac{s}{2} \end{cases}.$$

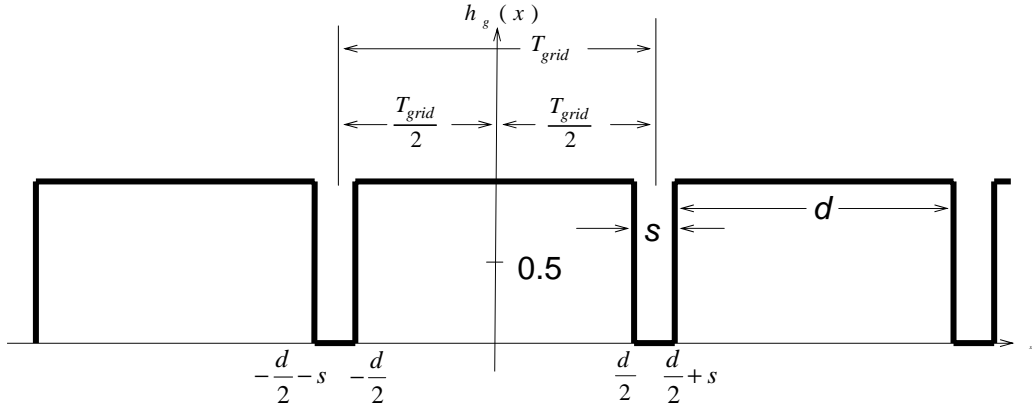


Fig. 2-5. Along a horizontal scan line, the vertical stripe signal is a square wave.

The periodical square wave can be expanded using the Fourier expansion [13], shown in the following equation:

$$h_g(x) = a_0 + \sum_{i=1}^{\infty} \left(a_i \cos \frac{2i\pi x}{T_{grid}} + b_i \sin \frac{2i\pi x}{T_{grid}} \right), \text{ where}$$

$$a_0 = \frac{1}{T_{grid}} \int_{-\frac{T}{2}}^{\frac{T}{2}} h_g(x) dx$$

$$a_i = \frac{2}{T_{grid}} \int_{-\frac{T}{2}}^{\frac{T}{2}} h_g(x) \cos \frac{2i\pi x}{T_{grid}} dx .$$

$$b_i = \frac{2}{T_{grid}} \int_{-\frac{T}{2}}^{\frac{T}{2}} h_g(x) \sin \frac{2i\pi x}{T_{grid}} dx,$$
(1)

The Fourier coefficients obtained by the integration are

$$a_0 = \frac{2d}{T_{grid}}$$

$$a_i = \frac{1}{i\pi} \sin \frac{2i\pi x}{T_{grid}} \Big|_{-\frac{d}{2}}^{\frac{d}{2}} .$$

$$b_i = 0, \quad i \geq 1$$
(2)

All of a_0 , a_i , and b_i are constants. Thus, the Fourier expansion for $h_g(x)$ can be rewritten as

$$h_g(x) = \frac{d}{T_{grid}} + \sum_{i=1}^{\infty} (a_i \cos(2i\pi x f_{grid})). \quad (3)$$

$h_g(x)$ can be separated into a DC (Direct Current) term, a fundamental wave and infinite harmonics. In Eq. (3), the first term, $\frac{d}{T_{grid}}$, is the DC term. The second term is the fundamental wave, $h_{g_1}(x) = a_1 \cos(2\pi x f_{grid})$. Note that the magnitude of $h_{g_1}(x)$ is a_1 and the frequency of $h_{g_1}(x)$ is $f_{g_1} = f_{grid}$. All of the following terms are the harmonics, denoted $h_{g_m}(x), m = 2, \dots, \infty$. The frequency of each harmonic term $h_{g_m}(x)$ is denoted as f_{g_m} . These harmonics have a higher frequency but a lower magnitude than the fundamental wave.

Let the sampling grid function $g_s(u, v)$ have a sampling frequency f_s on a horizontal line. According to the Nyquist Sampling Theorem, if

$$f_s \geq 2f_{g_i}, \quad i = 1, \dots, \infty, \quad (4)$$

then f_{g_i} can be reconstructed without aliasing. Otherwise, aliasing occurs. In Fig. 2-6, f_{g_i} is plotted as a thin curve. The bold dots are the samples obtained based on the image plate sampling frequency, f_s . Since f_s does not satisfy the Nyquist Sampling Theorem, low frequency aliasing occurs (the wave plotted as a bold curve).

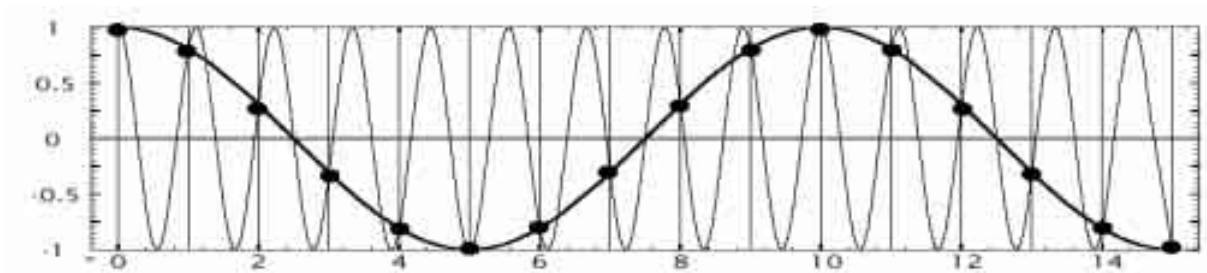


Fig. 2-6. A low frequency aliasing occurs (the wave plotted as a bold curve)

Let $f_{aliased_i}$ denote the aliasing frequency. $f_{aliased_i}$ can be obtained using Eq. (5) [14],

$$f_{aliased_i} = \begin{cases} k_1 f_s - f_{g_i} \\ f_{g_i} - k_2 f_s \end{cases}, \quad (5)$$

where k_1 and k_2 are integers and must be chosen to meet one of the inequalities in Eq. (6),

$$\begin{aligned} (k_1 - \frac{1}{2})f_s < f_{g_i} < k_1 f_s \\ k_2 f_s < f_{g_i} < (k_2 + \frac{1}{2})f_s \end{aligned}. \quad (6)$$

If the sampling frequency, f_s , is very close to f_{g_i} , according to Eqs. (4)-(6), $f_{aliased_i}$ is a low frequency signal that has a much lower frequency than f_{g_i} . Because human eyes are sensitive to low frequency signals, the artifacts are easily seen on a monitor. This phenomenon explains why the grid artifacts occur especially when the images are taken from high-resolution machines. If f_s meets the Nyquist Sampling Theorem, then the grid textures in the image plate can be fully reconstructed.

The above discussion is valid when there is grid texture in the image plate. The presence of a grid texture depends on the Point Spread Function (PSF) [15] of the imaging system. In a system with poor PSF, the grid texture is blurred such that the grid artifacts are not visible. Thus, the image sharpness is not improved.

When a CR image is acquired using a grid that is perfectly aligned with the image plate reader, there are the following cases.

1. There are no visible artifacts. This occurs if the PSF response of the system is poor. However, this is not the desired approach for removing the grid texture.
2. There are grid textures in the image plate. Let the grid artifacts frequency be f_{t_i} . There are two sub-cases,
 - a. f_s satisfies the Nyquist Sampling Theorem, thus the grid artifacts are the grid

textures in the image plate. In this case f_{t_i} is equal to f_{g_i} .

b. f_s does not satisfy the Nyquist Sampling Theorem. In this case f_{i_i} is equal to

$$f_{\text{aliased}_i}.$$

2.2 Case 2, $\theta \neq 0$, The Moiré Pattern

If there is an angle between the XY -coordinates and the UV -coordinates, there is an artifact called the moiré effect (Fig. 2-7). Many physicians have learned from experience that the grid orientation determines the moiré pattern [16]. The following discussions explain this phenomenon.

The vertical stripes $h_g(x, y)$ in the XY -coordinate perpendicular to the X -axis with period T can be presented as Eq. (7),

$$h_g(x, y) = h_g(x + T_{\text{grid}}, y). \quad (7)$$

$h_g(x, y)$ is sampled using the sampling signal $g_s(u, v)$ in the UV -coordinate system. $g_s(u, v)$ is a set of grids formed by lines perpendicular to the U -axis. These vertical stripes in the UV -coordinate system have a period T_s . It can be written as

$$g_s(u + T_s, v) = g_s(u, v). \quad (8)$$

Let the angle between the XY - and UV - coordinate systems be θ , as shown in Fig. 2-7. Points in the XY -coordinate system and UV -coordinate system can be related using the transformation

$$\begin{pmatrix} x \\ y \end{pmatrix} = R(-\theta) \begin{pmatrix} u \\ v \end{pmatrix}. \quad (9)$$

The phases of any point in both coordinate systems are given as

$$\phi = \frac{x}{T_{\text{grid}}} \text{ and } \phi_s = \frac{u}{T_s}. \quad (10)$$

Using Eq. (9), Eq. (10) is rewritten in the form

$$\phi = \frac{x}{T_{grid}} \text{ and } \phi_s = \frac{u \cos(\theta) - v \sin(\theta)}{T_s}.$$

The loci of the points for a particular phase difference $\Delta\phi$ is given by

$$\Delta\phi = \frac{u}{T_s} - \frac{\cos(\theta)u - \sin(\theta)v}{\frac{T_s}{\varepsilon}}, \quad (11)$$

where $\varepsilon = \frac{T_s}{T_{grid}}$. The condition for the points to have the same phase in both coordinate systems is

$$\Delta\phi = n, \quad n \in \{0, \pm 1, \pm 2, \dots\}. \quad (12)$$

Combining Eqs. (11) and (12) yields

$$v = -\left(\frac{1 - \varepsilon \cos(\theta)}{\varepsilon \sin(\theta)}\right)u + \frac{\varepsilon n T_s}{\varepsilon \sin(\theta)}. \quad (13)$$

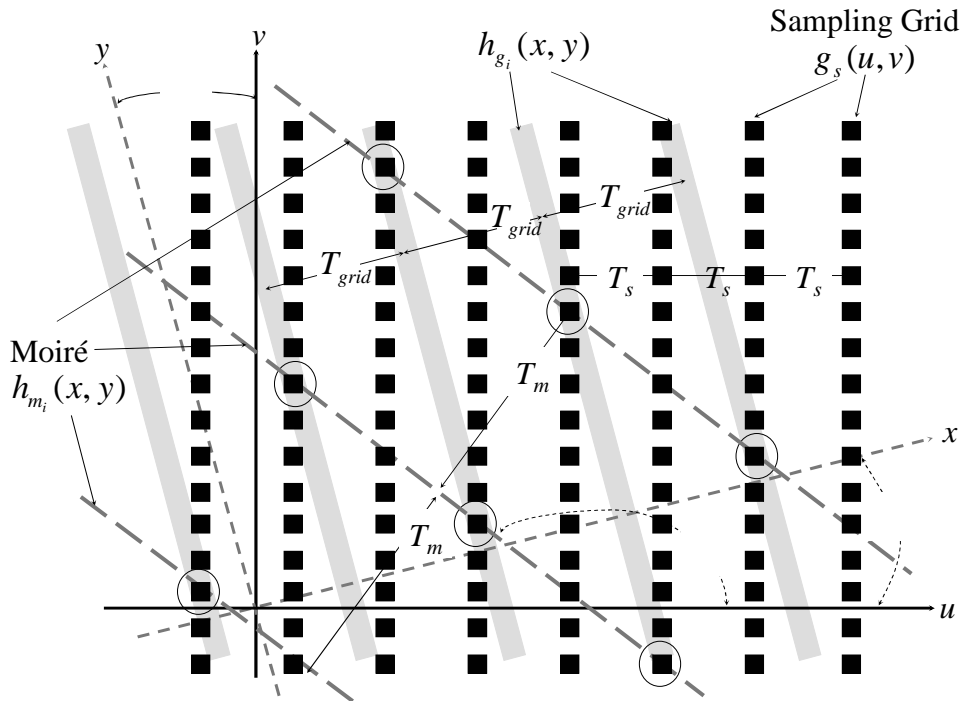


Fig. 2-7. Moiré pattern caused by two periodical functions.

Eq. (13) is a line with slope $-(1 - \varepsilon \cos(\theta))/(\varepsilon \sin(\theta))$. The set of dashed lines shown in

Fig. 2-7 is the moiré pattern. Observe that the slope $-(1-\varepsilon\cos(\theta))/(\varepsilon\sin(\theta))$ is a significantly large number for a very small angle θ . Fig. 2-8 shows that even a small angle, θ , causes a very large moiré pattern angle. Furthermore, the frequency of the moiré pattern can be obtained using Eq. (5). As discussed previously, this frequency is much lower than the frequency of the vertical stripe or the sampling frequency. Thus, the moiré pattern is perceptually clear.

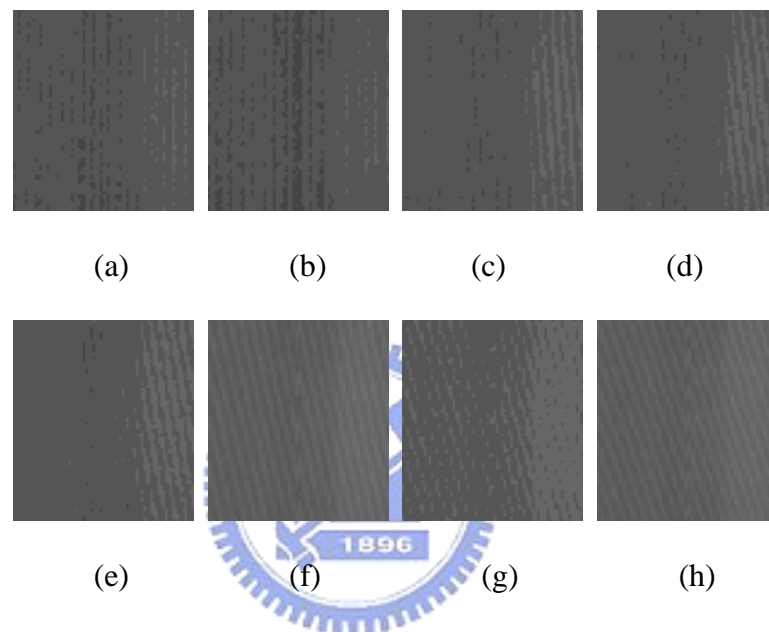


Fig. 2-8. A change in an angle θ from 0° to 2° will cause the stripe angle in the moiré pattern to change from 0° to 24° .

2.3 Displaying an Image Containing Artifacts on a Monitor

A typical clinical-grade monitor has a resolution of approximately 2560 by 2048 pixels [17]. The resolution of CR images could be higher than a monitor's. For example, the resolution of the image shown in Fig. 2-9 is 3062 by 3730 pixels. It is necessary to reduce the size of a high-resolution CR image to allow it to fit on a monitor. Suppose there are grid artifacts in the image. Sampling the artifacts by the low-resolution monitor pixels, according to Eqs. (5) and (6), produces lower frequency artifacts.

3. METHODS

There are two traditional methods used to remove artifacts [18-19]. The first uses a grid with a high enough frequency to blur the artifacts. The second method uses a Bucky to blur the grid artifacts.

The grid artifacts can be eliminated by increasing the grid frequency so that the grid becomes invisible under the sampling frequency of the plate reader. Unfortunately, the grid frequency cannot be increased indefinitely. Another method for grid artifact removal is by using a Bucky. A grid that moves quickly during CR image production is called a Bucky. If the exposure time is long enough and the Bucky speed is high enough, the grid artifacts are blurred or even removed completely. A detail discussion of the effect of the Bucky can be found in the Appendix. However, the movement speed is limited by the mechanical structure. Therefore, using a Bucky can reduce, but cannot guarantee the elimination of artifacts.

In this section, a simple method to remove the artifacts is presented. Recall that the artifacts are produced at two points on the image producing path:

1. The first point is achieved by sampling the grid texture in the image plate.
2. The second point is achieved by sampling the image containing grid artifacts by using an output device.

If the cause in the first point can be removed, then all the artifacts are removed. Artifact removal consists of three major steps: (1) estimating the artifact frequency, (2) accurately locating that frequency, and (3) removing the frequency using a Gaussian band-stop filter in the frequency domain.

3.1 Estimating the Artifact Frequency

The sampling frequency f_s is recorded in DICOM tag (0018:1164) [20-22]. In DICOM

standard, this tag is the “Imager Pixel Spacing”, T_s , that is $\frac{1}{f_s}$. The grid frequency f_{grid} is available from the grid specification. Thus the fundamental wave and harmonics, h_{g_i} , and their frequencies, f_{g_i} , are obtained using Eq. (3). Let the frequencies of the artifacts be denoted as $f_{t_i}, i \geq 1$. $f_{t_i}, i \geq 1$ is estimated using the following rules:

1. Sampling frequency f_s satisfies the Nyquist Sampling Theorem, i.e., $f_s \geq 2f_{g_i}, i \geq 1$.

Since the grid can be totally reconstructed, the estimated aliased frequency f_{t_i} is equal to f_{g_i} .

2. Sampling frequency f_s does not satisfy the Nyquist Sampling Theorem, i.e., $f_s < 2f_{g_i}$.

The estimated aliased frequency f_{t_i} is obtained using Eqs. (5) and (6).

3.2 Locating the Frequency f_{t_i} :

Let $I_r(x,y)$, $0 \leq x \leq M-1$ and $0 \leq y \leq N-1$, be an image containing grid artifacts. Let $l_r(x)$ be a row of $I_r(x,y)$. The 1D discrete Fourier transformation pairs for x -axis are

$$L_r(u) = \sum_{k=0}^{M-1} l_r(x) e^{-j2\pi kx/M}, 0 \leq u \leq M-1, \text{ and} \quad (14)$$

$$l_r(x) = \sum_{k=0}^{M-1} L_r(u) e^{j2\pi kx/M}, 0 \leq x \leq M-1. \quad (15)$$

The spectrum is

$$|L_r(u)| = (L_r(u) \cdot L_r^*(u))^{0.5}, \quad (16)$$

where “*” means conjugate.

We assume the power of the grid artifact has a Gaussian distribution (Eq. (17)) in the spectrum:

$$G(u) = \frac{1}{\sigma\sqrt{2\pi}} e^{-\frac{(u-\mu)^2}{2\sigma^2}}. \quad (17)$$

By estimating μ and σ of the Gaussian distribution, we can construct the band-stop Gaussian filter, $B(u)$. The reason for choosing a Gaussian filter is that the Fourier transform of a Gaussian function is a Gaussian function. Using a Gaussian filter will not produce ripple effect. To design an accurate band-stop Gaussian filter, μ should be equal to f_{t_i} . But due to the imperfections that sometimes result during the manufacturing of the grid or the grid is not perfectly aligned, there could be a small deviation. The accurate mean is obtained by calculating the mean of the interval from $f_{t_i} - (f_{t_i}/10)$ to $f_{t_i} + (f_{t_i}/10)$ in the spectrum. The standard deviation, σ , is also computed from the interval when the accurate mean is located. The image in Fig. 2-9 (a) contains grid artifacts. The 1D Fourier transform in x direction is shown in Fig. 2-9 (d). Fig. 2-9 (d) shows the power spectrum after taking a logarithmic operation. The circle shown in Fig. 2-9 (d) is the frequency of the grid artifacts.

3.3 Remove the Frequency:

Since the harmonics have a higher frequency but a much lower magnitude than the fundamental wave, the effect of harmonics is small and can be ignored. In this study, only the fundamental wave is removed. It is removed by using Gaussian band-stop filter for each row in the image as shown in Eq. (18),

$$B(u) = \frac{1}{\sigma\sqrt{2\pi}} - \frac{1}{\sigma\sqrt{2\pi}} e^{-\frac{(u-\mu)^2}{2\sigma^2}}, \quad u = 1 \dots M. \quad (18)$$

The accurate mean and standard deviation are substituted into Eq. (18) to construct the Gaussian band-stop filter $B(u)$. We multiply $L_r(u)$ by $B(u)$ to obtain $L'_r(u)$ shown in Eq. (19),

$$L'_r(u) = L_r(u) \cdot B(u), \quad u = 1 \dots M. \quad (19)$$

Taking the 1D inverse Fourier transform (Eq. (15)) of $L'_r(u)$, we obtain a grid texture free row, $l'_r(x)$. We apply the process stated above for each row in $I_r(x,y)$ to obtain an image, $I'_r(x,y)$. $I'_r(x,y)$ is free of grid artifacts, as shown in Fig. 2-9 (f).

4. RESULTS

Both clinical and phantom images were used to evaluate the proposed method. Fig. 2-9 (a) shows an image of a mammography quality control phantom (Art No. 6652348, Phantom No. C104, Fuji, Japan). The image resolution is 3062 by 3730 pixels. A 40 lines/cm grid was used while acquiring the image. The sampling rate was 8.77193 pixels/mm (0.114 mm/pixel). Thus, f_{g_1} is 4 lines/mm (40 lines/cm) and f_s is 8.77193 pixels/mm. Since $f_s > 2f_{g_1}$, the sampling frequency satisfies the Nyquist Sampling Theorem. Therefore, the grid textures in the image plate can be reconstructed and the grid artifact frequency is 4 lines/mm. Since the sampling frequency is $f_s = 8.77193$ lines/mm, the grid artifact frequency is estimated to be 0.461 of the sampling frequency, as shown in Fig. 2-9 (d). By applying the Gaussian Filter, the artifact frequency is removed. Fig. 2-9 (b) shows a selected region in Fig. 2-9 (a) in the original resolution. Fig. 2-9 (c) shows the image in which the artifact is eliminated. Fig. 2-9 (e) shows a zoomed out image of the mammography phantom image in Fig. 2-9 (a). The resolution was scaled down from 3062 by 3730 pixels to 540 by 658. The moiré pattern is significant. Fig. 2-9 (f) shows an image in which the artifact was eliminated by applying the proposed method.

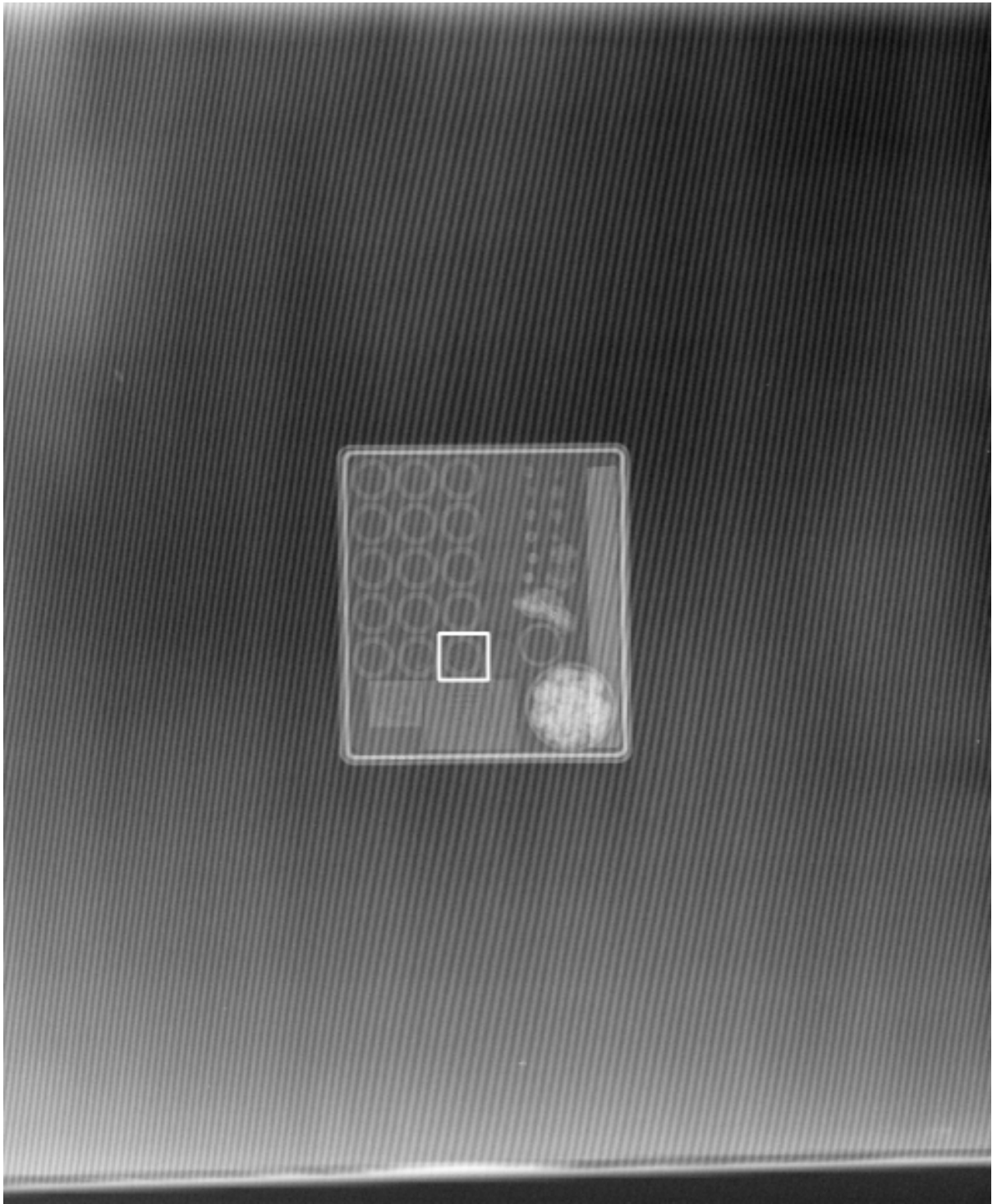
Fig. 2-10 (a) is a CR chest image with resolution 2048 by 2494 pixels. A 3.3 lines/mm ($f_{g_1} = 85$ lines/inches) grid was used while acquiring the image. The sampling frequency, f_s , is 5.8 pixels/mm. This case does not satisfy the Nyquist Sampling Theorem ($f_s < 2f_{g_1}$). The artifact frequency $f_{\text{aliased}} = kf_s - f_{g_1} = 2.59$ (lines/mm), where $k=1$. Since the sampling

frequency is $f_s = 5.8$ lines/mm, the estimated frequency of the artifact appears to be 0.45 of the sampling frequency (Fig. 2-10 (d)). Fig. 2-10 (b) shows a selected region in Fig. 2-10 (a) in the original resolution. Fig. 2-10 (c) is an image in which the artifact was removed.

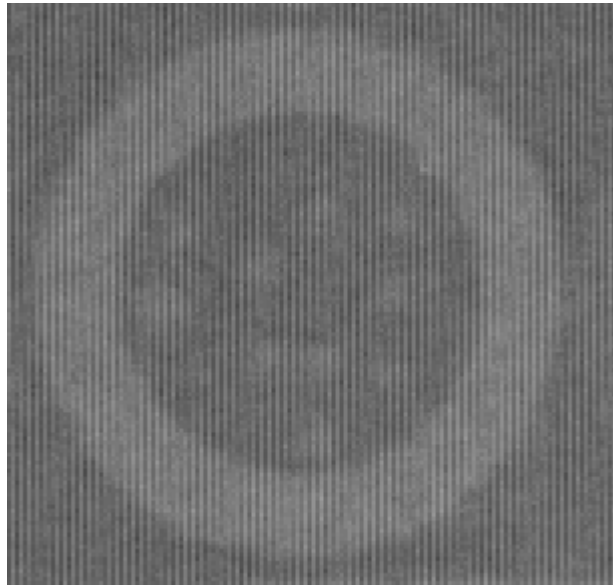
Fig. 2-10 (e) shows the spectrum after the grid artifacts were removed.

In order to compare the proposed method against the previous computer methods for artifact removal, we used an image containing three characters as shown in Fig. 2-11 (a). Although these are not clinical images, using geometric shaped characters is the best way to demonstrate the effect of the applied methods. Fig. 2-11. (a) is the original image containing grid artifacts. Fig. 2-11. (b) shows the grid artifacts removed using the proposed method. Fig. 2-11 (c) shows the grid artifacts removed using the blur kernel proposed by Barski [3]. When compared to the result obtained by the proposed method, the sharp edges in Fig. 2-10 (c) are blurred. Grid artifacts in Fig. 2-11 (d) were removed using a notch filter proposed by Belykh [4]. Although the sharp edges are preserved, there are ripples after the artifacts are removed.

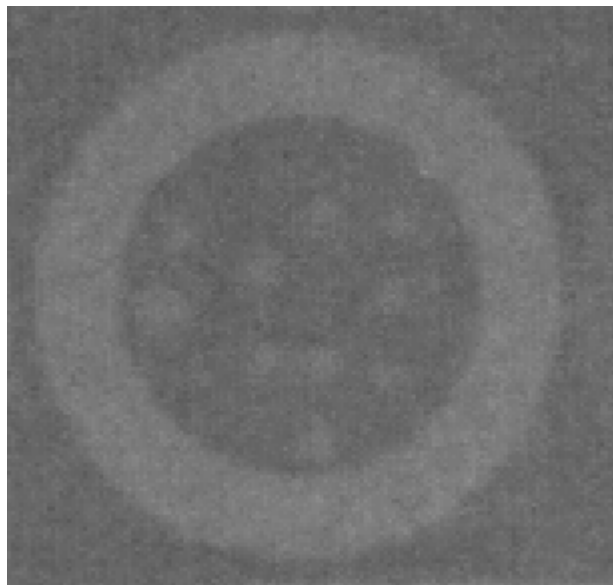




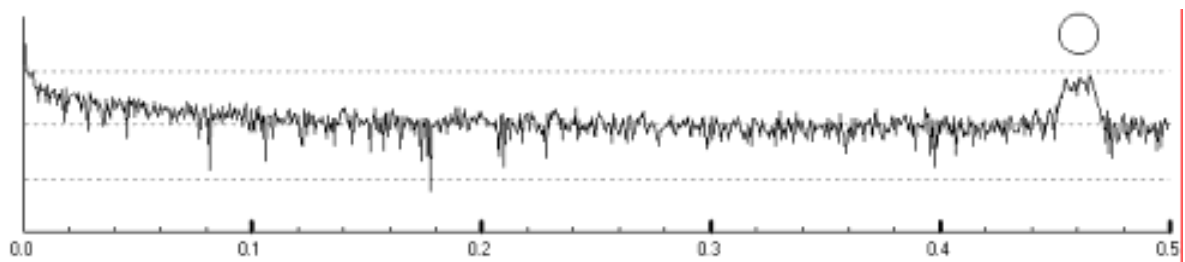
(a) 3062 x 3730 pixels



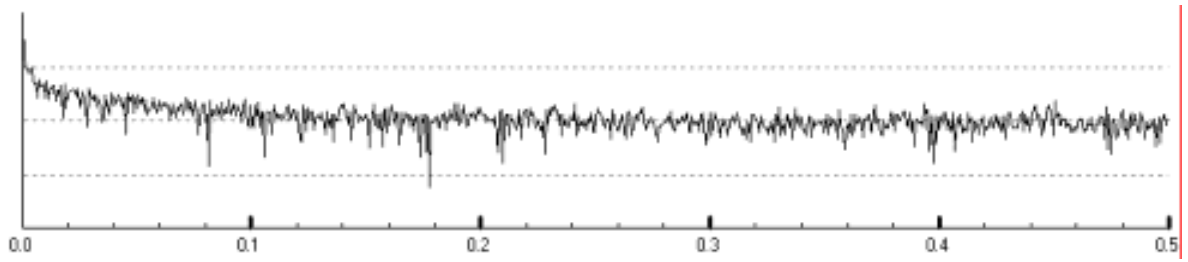
(b) Selected area from (a), showing grid artifacts.



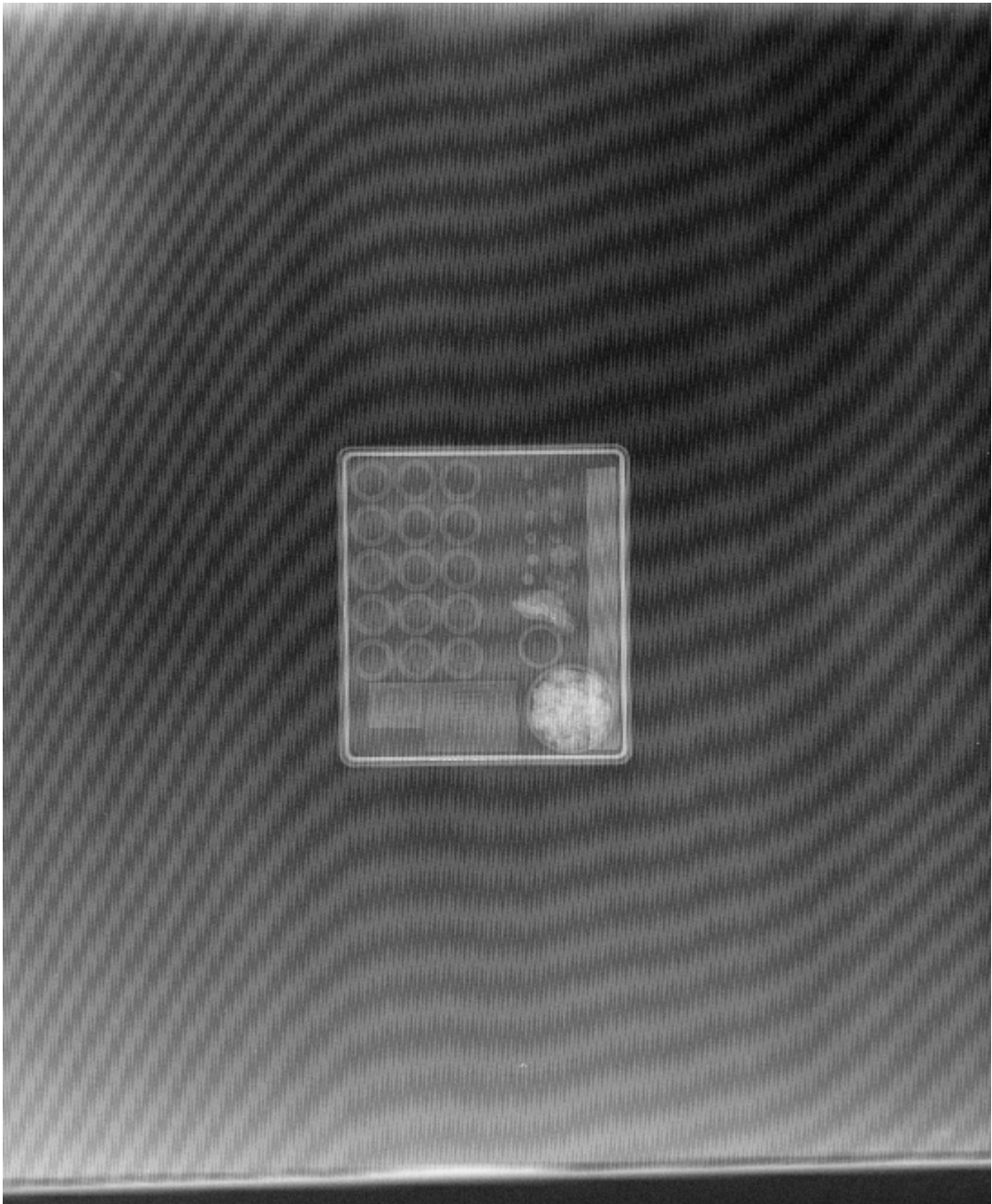
(c) Selected area from (a), with grid artifacts removed.



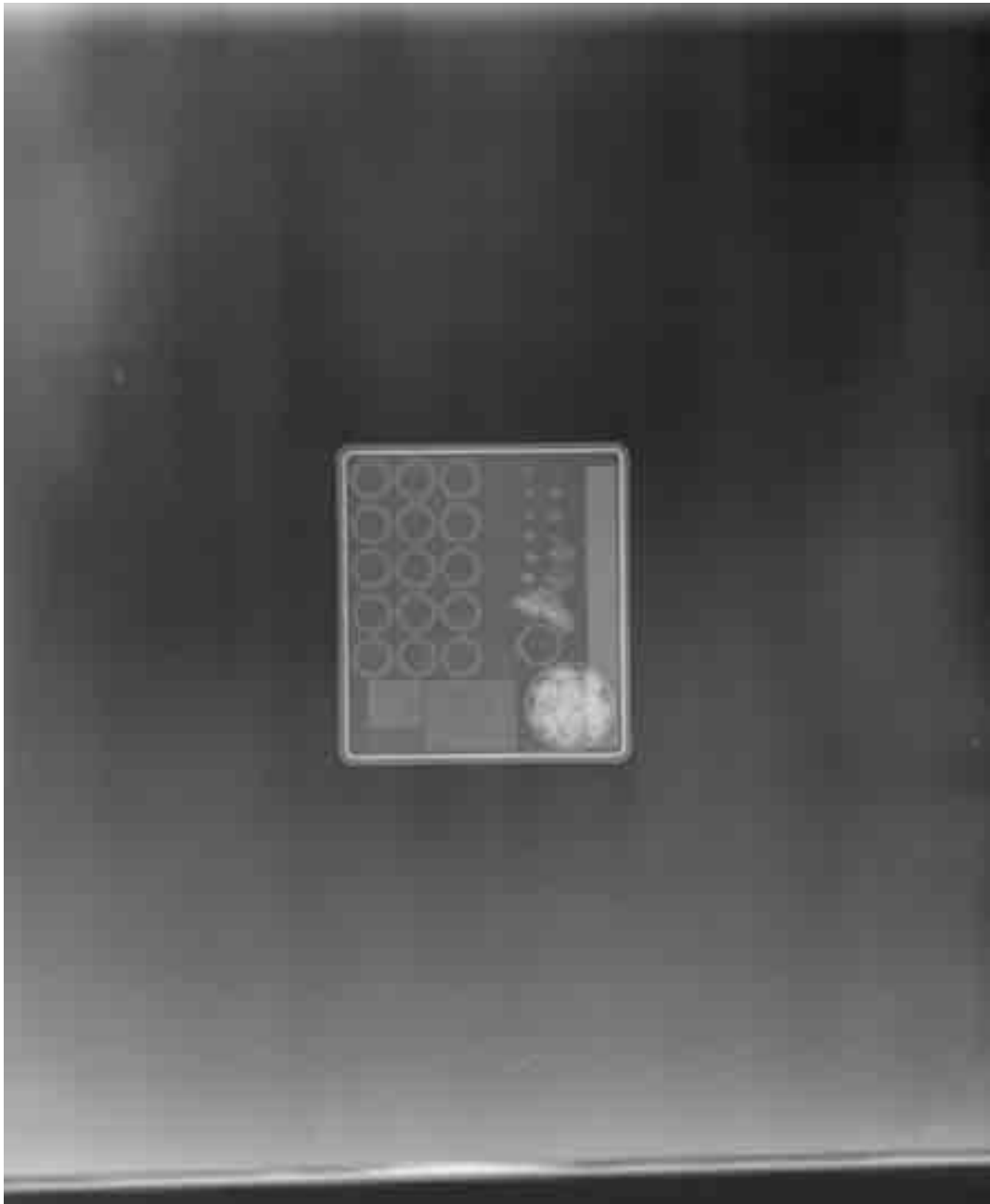
(d) 1D Fourier transform of the image in (a). Grid artifact frequency indicated by the circle.



(e) The spectrum after grid artifacts removed.



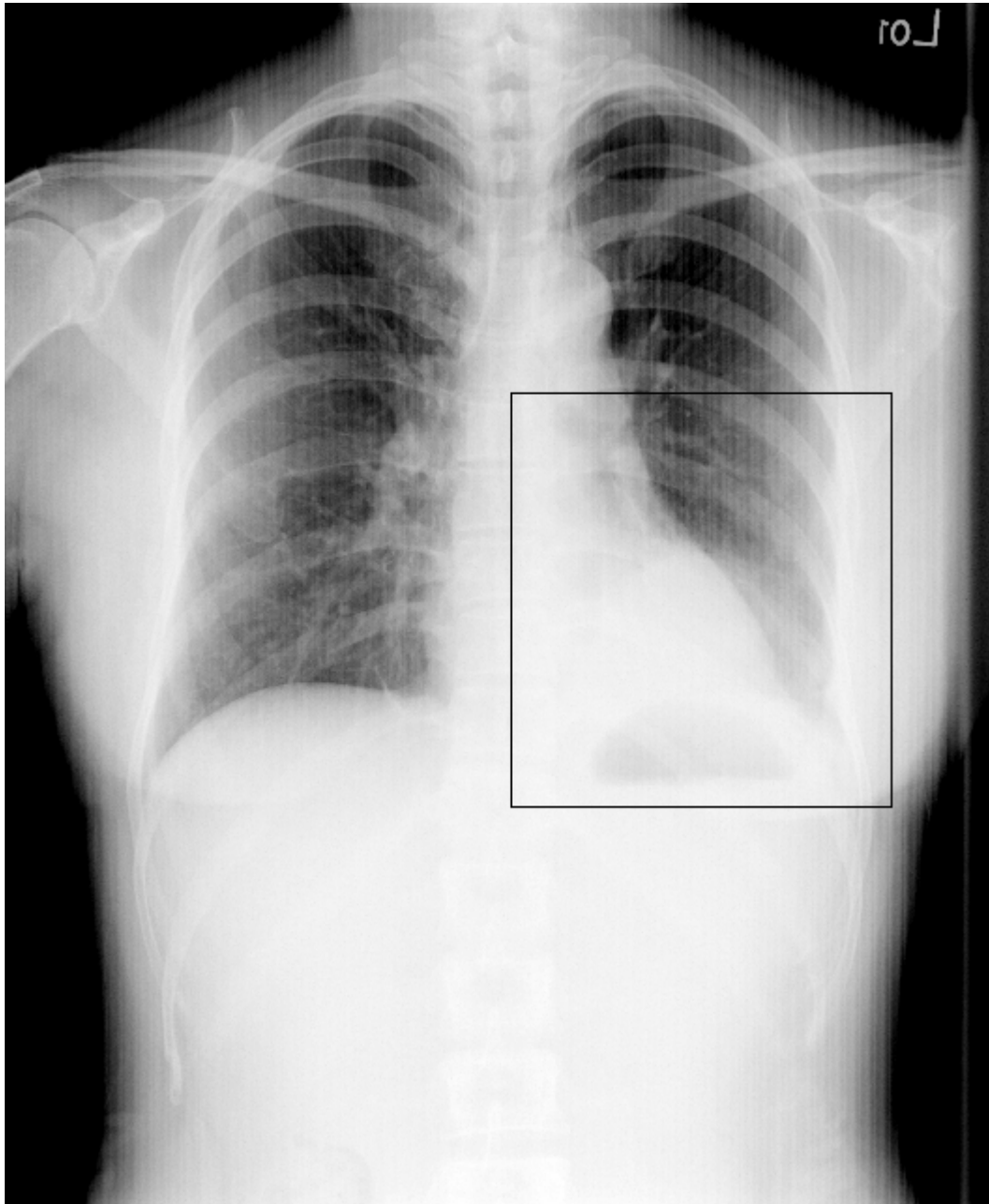
(f) 540 x 648 pixels



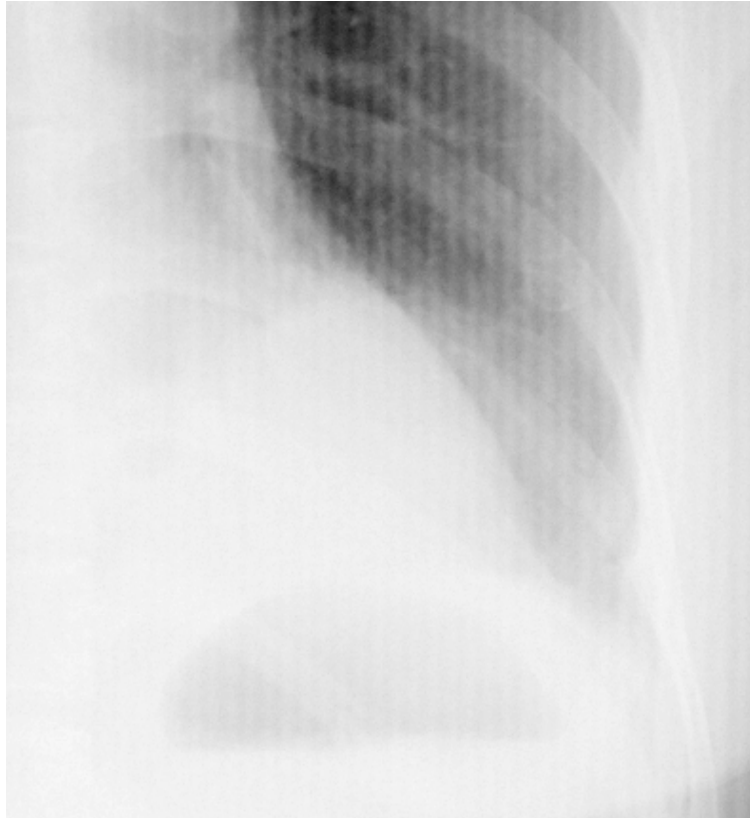
(g) 540 x 648 pixels, with grid artifact removed.

Fig. 2-9. (a) Mammography Quality Control Phantom (Phantom No.C104, Fuji, Japan) image with grid artifacts. (b) A selected region in (a) is shown in the original resolution. The artifacts are easily seen. (c) The same region, with grid artifacts eliminated. Note that many details such as the vertical stripes can be clearly distinguished. (d) The spectrum of a 1D Fourier transform of the image shown in (a). The y-axis is logarithmic. The frequency of the grid artifact is highlighted with a circle. (e) The spectrum after grid artifacts are removed.

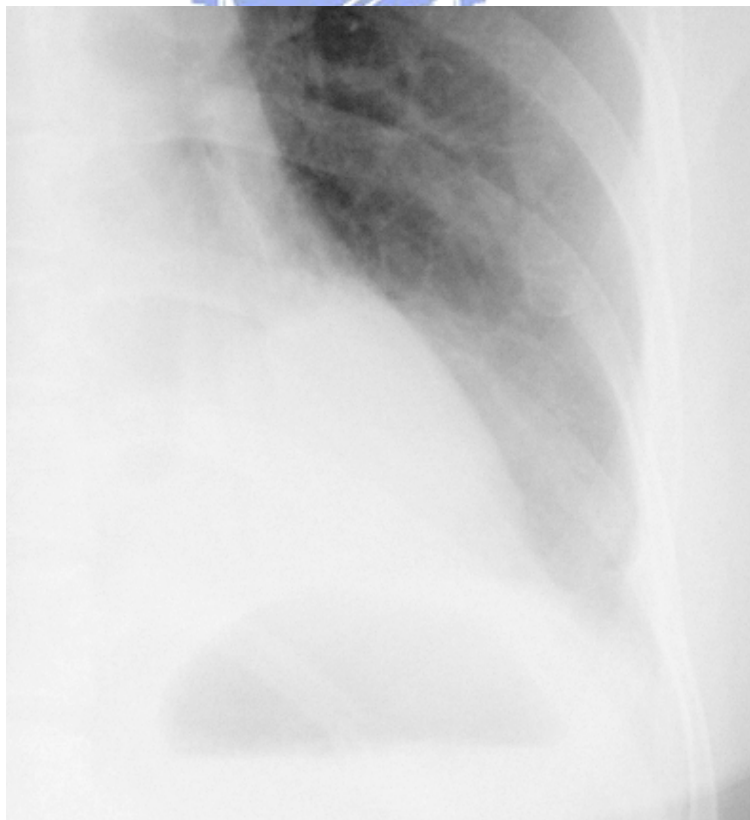
(f) An image of the Mammography Quality Control Phantom scaled down 17% to a resolution of 540 by 658 pixels. It shows a very serious artifact (the moiré pattern). (g) The moiré pattern was eliminated using the proposed method.



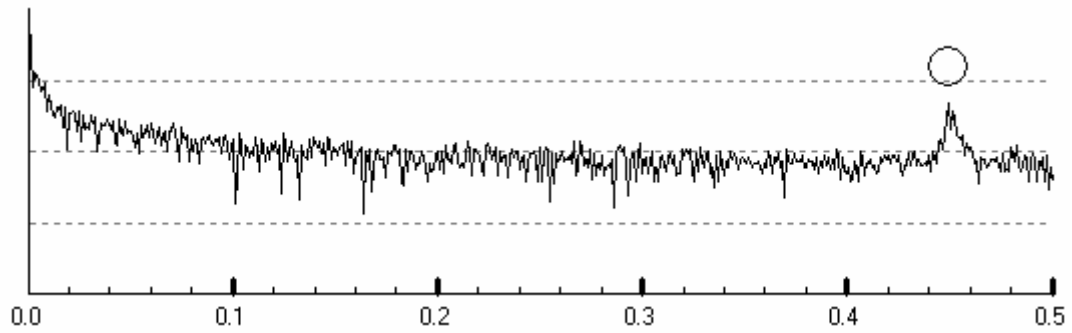
(a) 2048 x 2494 pixels



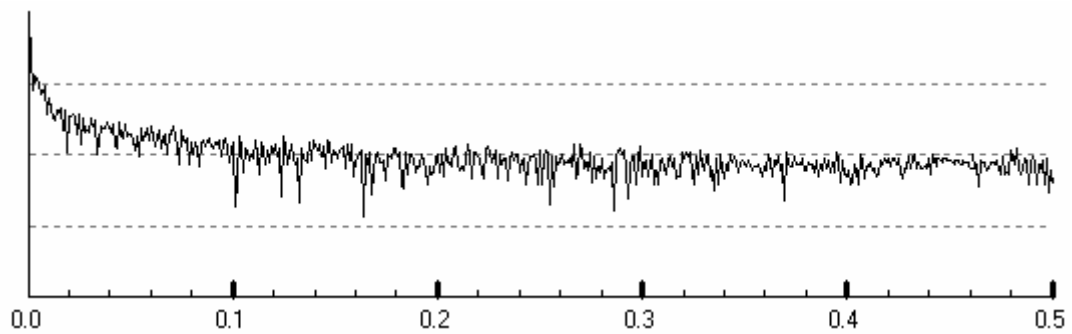
(b) Selected area from (a), enlarged. It contains fine vertical stripes.



(c) Selected area from (a), with grid artifacts removed.

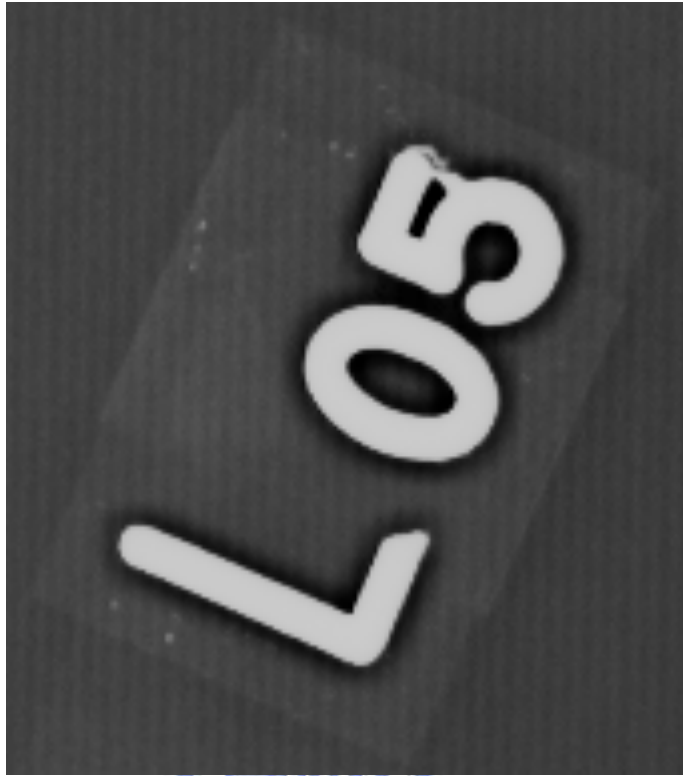


(d) 1D Fourier transform of the image in (a). Grid artifact frequency indicated by the circle.

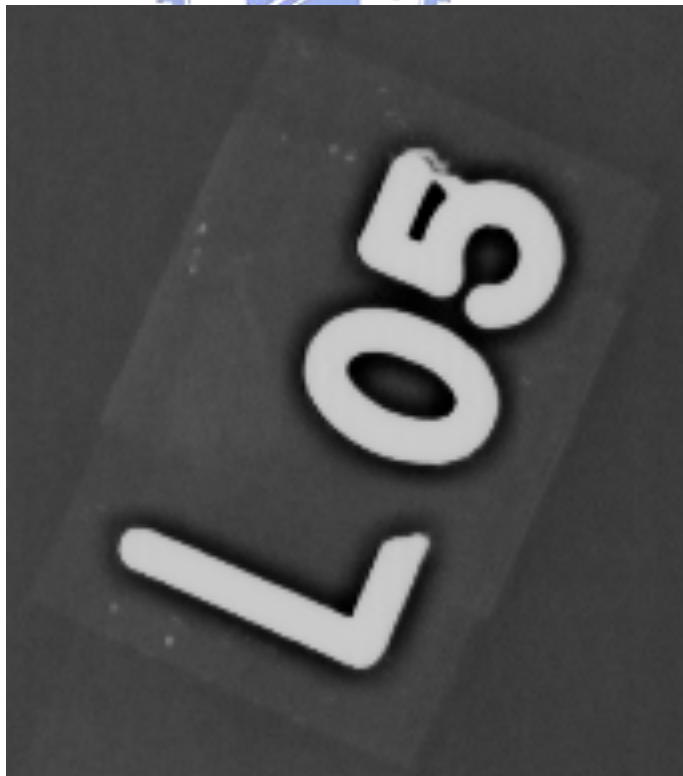


(e) The spectrum after grid artifacts are removed.

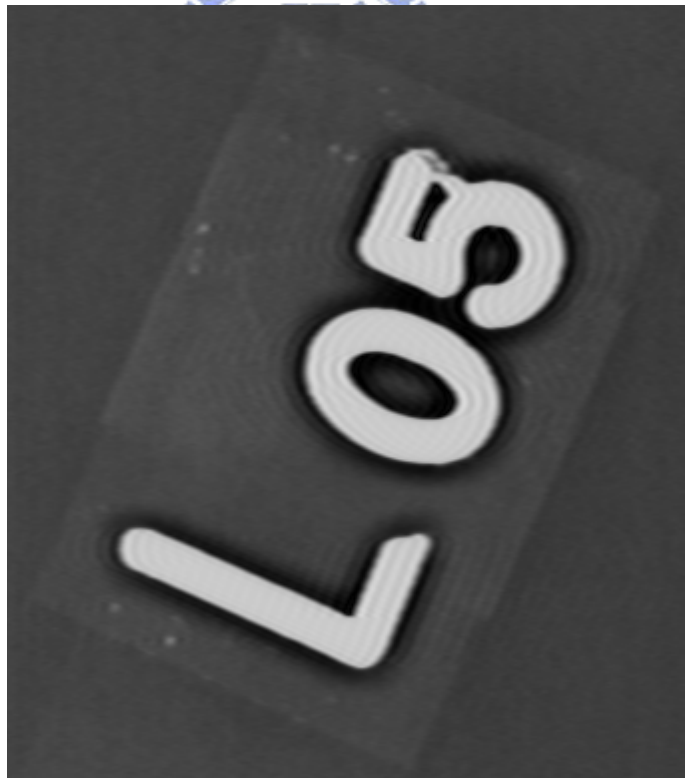
Fig. 2-10. (a) A patient with left lower lobe consolidation due to pneumonia. Grid pattern can be seen on CR chest image (b) The portion that is highlighted in white in (a). (c) The grid pattern was removed using the proposed method. (d) The spectrum of a 1D Fourier transform of the image shown in (a). The y-axis is logarithmic. The frequency of the grid artifact is highlighted with a circle. (e) The spectrum after grid artifacts are removed.



(a)



(b)



(d)
Fig. 2-11 . (a) The original image with grid textures. (b) The grid textures were removed using the proposed method. (c) The grid textures were removed using the blur kernel proposed by Barski. (d) The grid pattern was removed using a notch filter proposed by Belykh.

4.1 FROC Study

A study was designed to evaluate observers' performance in the detection of detailed structures in images before and after grid artifact removal. Physicians were asked to determine the presence of microcalcification in a portion of the mammography quality control phantom (C104, Fuji, Japan), shown in Fig. 2-12. The phantom images were taken with a grid, under three conditions.

1. Images were taken using an Agfa ADC CR system. The image resolution was 3062 by 3730 pixels and the image size was 35 cm by 43 cm.
2. Images were taken using an Agfa ADC CR system. The image resolution was 2048 by 2494 pixels and the image size was 35 cm by 43 cm.
3. Images were taken using a Fuji 5502D CR system. The image resolution was 2000 by 2510 pixels and the image size was 20 cm by 25 cm.

In all three cases, 0-degree, 90-degree and 180-degree rotations of the images were performed. Thus, nine radiographs were obtained. The proposed method was then applied to each radiograph to remove the grid artifacts, resulting in an additional nine images.

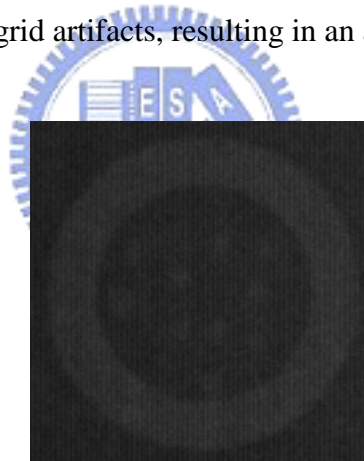


Fig. 2-12. The portion of the mammography quality control phantom used to evaluate observers' performance.

Two board-certified radiologists blinded to the distribution and number of microcalcifications evaluated all eighteen images in random order. Observers were asked to determine the presence of microcalcifications according to a scale of four levels of confidence: 1, probably absent; 2, indeterminate; 3, probably present; 4, definitely present. Because the moiré pattern increases if we display the images on a low-resolution monitor, we also performed another evaluation when the image resolution was reduced to 80% of the original size. The image size reduction method was implemented by taking the averaged intensities of

neighboring pixels of a sampled point to form one pixel in the reduced size image. Another board-certified radiologist, also blinded to the distribution and number of microcalcifications, evaluated these images again.

The Free-Response Receiver Operating Characteristic (FROC) [7] curves were drawn based on the results obtained. The FROC curve describes the tradeoff between the “Microcalcification Localization Fraction” and the “False Positive per Image”. The former is defined as the probability of a microcalcification to be specified, and the latter is defined as the mean number of times a noise was classified as a microcalcification. In the FROC experiment, the observers gave their level of confidence on the presence of microcalcifications for different candidate’s regions. We then plotted the discrete FROC curve by setting different thresholds to the confidence levels, i.e., the candidate was considered to contain microcalcifications only when the confidence level was higher than the threshold. The resulting curves are as shown in Figs. 2-13 and 2-14. As shown in Fig. 2-13, we conclude that observers could achieve perfect performance without any false positives, regardless of the presence of grid artifacts, when the full sized images were available. **Fig. 2-14** shows that when only reduced-size images were available, observers could achieve better performance when the grid lines were removed.

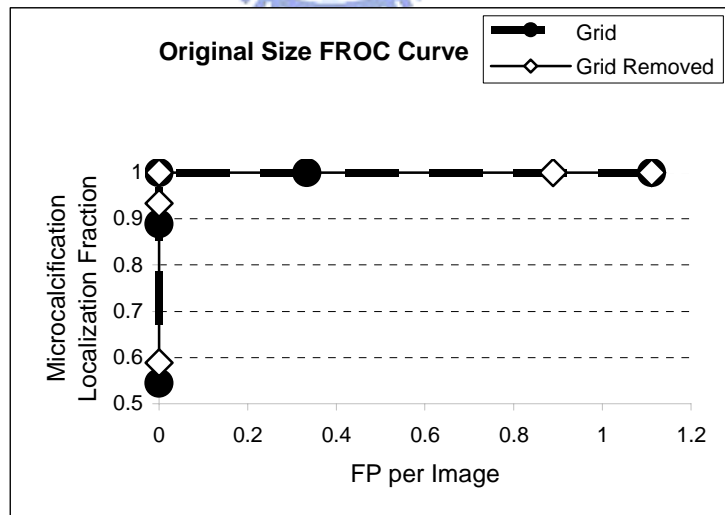


Fig. 2-13. The FROC curves for the observers studying the original image size. Observers could achieve perfect performance regardless of the presence of the grid lines.

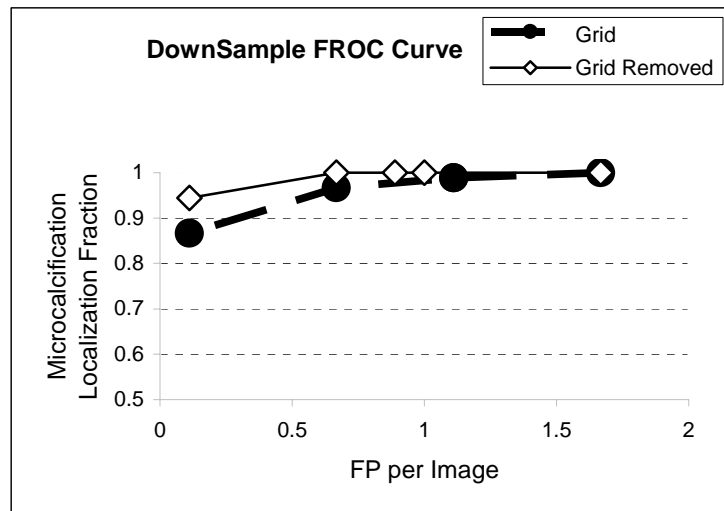


Fig. 2-14. The FROC curves for observers studying reduced-size images. The performance is better when the grid lines are removed.

5. CONCLUSIONS AND DISCUSSION

In this chapter, the formation of grid artifacts in CR images was studied in detail. An automatic method was then presented to remove the grid artifacts. The method was implemented on a PC with a Pentium 4 (2 GHz) CPU running the Windows 2000 operating system. The total execution time for images with different resolutions of 1760 by 2140, 2000 by 2510, and 3520 by 4280 pixels took 10, 12, and 24 seconds, respectively.

Although the grid artifacts can be removed by using a Bucky or a higher frequency grid, there are limitations to these two methods. For example, there are cases in which radiographic images are acquired when a Bucky is not accessible. In addition, as the grid frequency increases, there is relatively more grid material to absorb radiation. This situation requires that the patient be exposed to a higher dose of radiation [23]. Using the proposed method, these problems are overcome, and images that are free of grid artifacts are obtained.

Compared to the results obtained by the methods of Barski and Wang [3] and Belykh and Cornelius [4], the proposed method neither produces ripple artifacts nor blurs the image. The proposed method achieves much better results. An important question is that whether the proposed method improves the accuracy of diagnosis. Rigorous experiments should be done to clarify this point. A problem with the proposed method is the computing time required. Future studies will investigate methods to reduce the computing time.



CHAPTER 3

An Automatic Method to Compare the Lanes in Gel Electrophoresis (GE)

Images

Gel Electrophoresis (GE) is an important tool in genomic analysis. GE results are presented in images. Each image contains several vertical lanes. Each lane consists of several horizontal bands. Two lanes are identical if the relative positions of the bands are the same. We present a computer method designed to compare the lanes and identify identical lanes. This segmentation method, developed using many image-processing techniques, is applied to extract the lanes and bands in GE images. The lanes are then converted into “position vectors” that describe the positions of the bands. This method can accurately identify identical lanes, helping biologists to identify the identical lanes from many lanes with much less effort.

1. INTRODUCTION

Gel electrophoresis (GE) was developed as a means for resolving biological macromolecules, such as DNA, RNA, and protein molecules [24]. There are several different types of GE based on their resolution ranges. One major application of GE is to separate DNA molecules from 0.5 kbp to approximately 10 Mbp. GE is an invaluable tool for gene and genomic analysis and it is routinely used in many applications, such as gene identification, isolation, and purification. GE is used in various fields like biology, molecular biology, biochemistry, biotechnology, medicine and clinical diagnosis.

This technique produces images that consist of several vertical lanes. Each lane contains a number of horizontal bands. The positions of the horizontal bands represent the molecular weights of the bands. Two subjects are the same if their lanes have the same pattern. The goal of this work was to design a computer method that automatically identifies lanes with the same pattern among many lanes.

Previous work regarding the study of this problem can be found in [25]. In [25], the lanes in a GE image were first segmented and converted into a chain code representation. The lane comparison was carried performed by calculating the longest common subsequence (LCS) in two chain codes. The similarity between the lanes was represented by two times the LCS length over the total length of the two chain codes. Two lanes are similar if the result is close to one. This method did not segment the bands in each lane so it could not produce an exact comparison result. It could only eliminate those very different lanes and reduce the number of lanes to be compared. Another disadvantage is that it employed a dynamic programming technique to calculate the LCS for two chain codes. The computation time was thus long.

In this chapter, we present a method that can accurately identify identical lanes. In the proposed method, the bands and lanes are segmented and then converted into a “position vector” that indicates the positions of the bands. Two lanes that have the same position vectors are considered having the same pattern. In this task, accurate lane and band segmentation is crucial to the later comparison step.

Lane and band segmentation is difficult due to the quality of the GE images. There are many factors, such as the applied voltage, field strength, pulse time, reorientation angle, agarose type, concentration and buffer chamber temperature. All of these factors affect the image quality and the patterns in the lanes [26-27]. The images acquired in our system have a grid-texture in the background that contaminates the imaging system. All of these factors make the segmentation task difficult.

The segmentation method presented in this chapter consists of several steps. The first step is the preprocessing step that removes the grid-texture artifacts. The background is then removed so that the bands in the images are enhanced. In the next step, the bands and the lane containing the bands in the image are extracted. The positions of the bands are then normalized and converted into a position vectors. Lane comparison then becomes a

comparison of lane position vectors. The proposed method is described in Section 2. The results are shown in Section 3.

2. METHOD

2.1 Background Removal

There are two tasks in the background removal step. The first is the grid-texture removal. As mentioned previously, the grid-texture is contaminated from the imaging system. Fig. 3-1 shows a typical GE image acquisition system. Because the bands and lanes in gel are not visible under visible light, the gel box is illuminated using a fluorescent UV light source. There is a grid located between the gel box and the CCD camera, as shown in Fig. 3-2. The grid is used to collimate the light to prevent scattering. The grid improves the sharpness of the GE images by trapping most of the scattered light. Unfortunately the grid also causes grid-texture artifacts in the GE image, as shown in Fig. 3-3 (a) and (b).

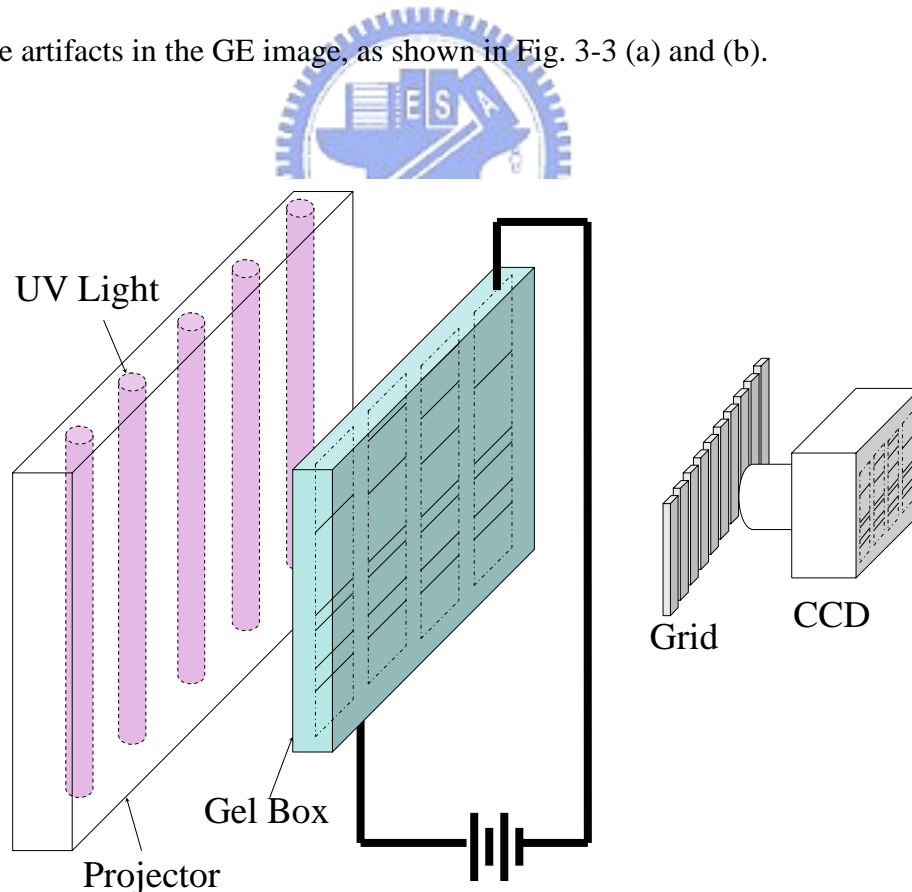


Fig. 3-1. The imaging system, there is a grid between the CCD camera and the gel box.

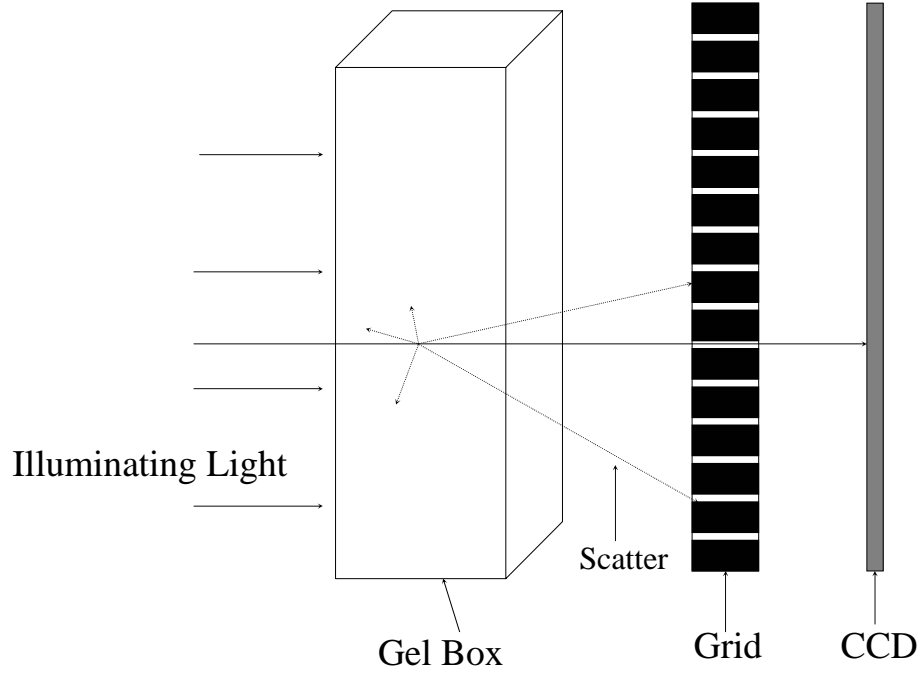


Fig. 3-2. The grid collimates the light.

The grid-texture has a fixed frequency in the frequency domain so that it can be easily removed from the frequency domain. Let $f(x, y)$, $0 \leq x \leq M - 1$ and $0 \leq y \leq N - 1$, denote an M by N GE image. The 1-D discrete Fourier transformation pairs are defined as

$$F(u, y) = \sum_{x=0}^{M-1} f(x, y) e^{-j2\pi kx / M} \quad 0 \leq x \leq M - 1, 0 \leq y \leq N - 1, \text{ and} \quad (20)$$

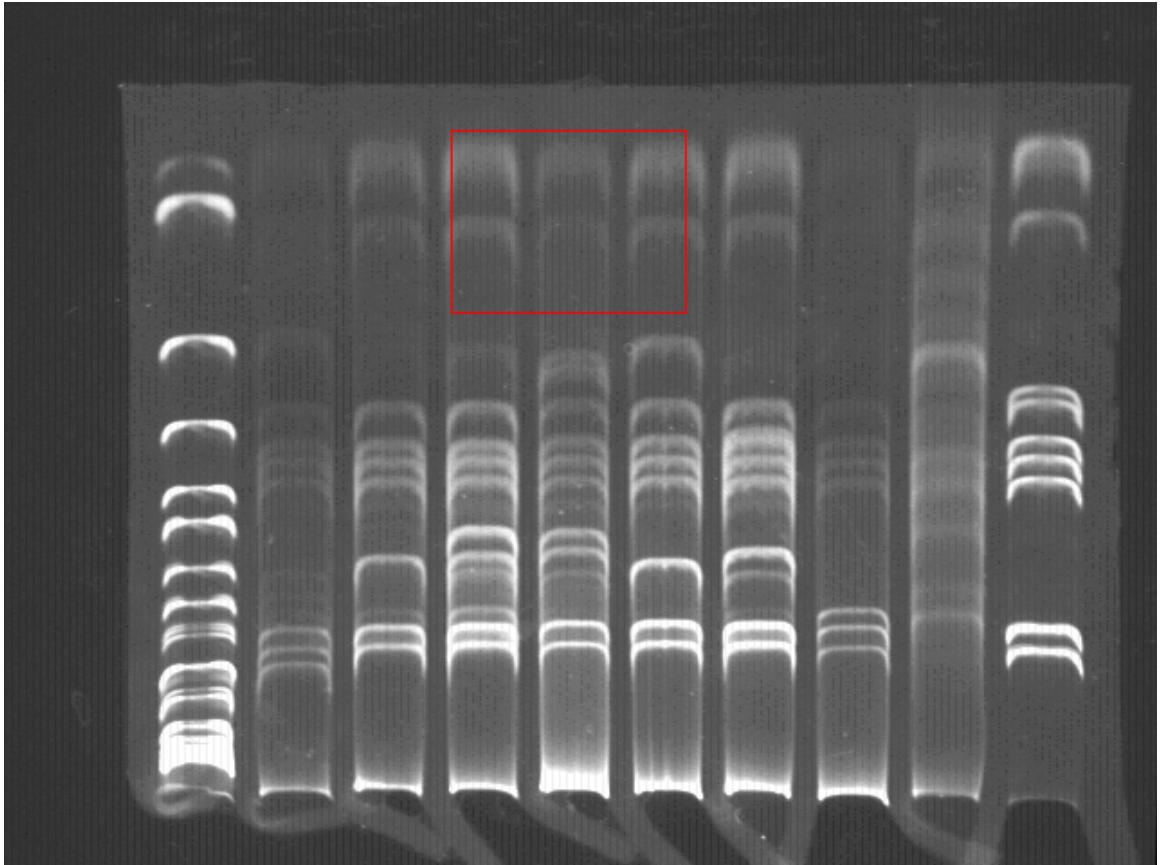
$$f(x, y) = \sum_{u=0}^{M-1} F(u, y) e^{j2\pi kx / M} \quad 0 \leq u \leq M - 1, 0 \leq y \leq N - 1. \quad (21)$$

The 1-D Fourier transform (Eq. (20)) to $f(x, y)$ is applied in direction x to obtain $F(u, y)$ in the frequency domain. Its power spectrum is shown in Fig. 3-4 (a). In this figure a double-sided spectrum was used. The left half is the complex conjugate reflection of the right half. The grid-texture in the spatial domain is transformed into a specific frequency that causes observable peaks on both sides within the red line pairs (Fig. 3-4 (a)). The power of the peak frequencies is many times that of the other frequencies except for those near the DC

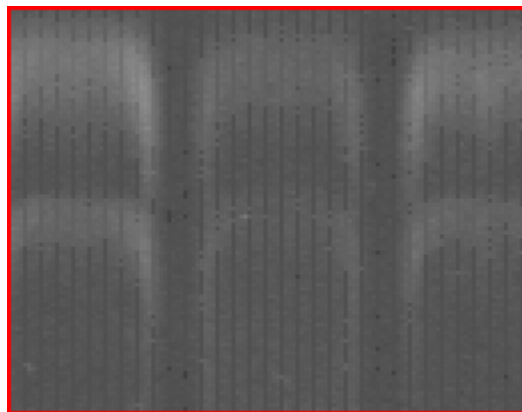
term.

We apply the method propose in Chapter 2 to obtain a grid-texture free image, $f_2(x, y)$.

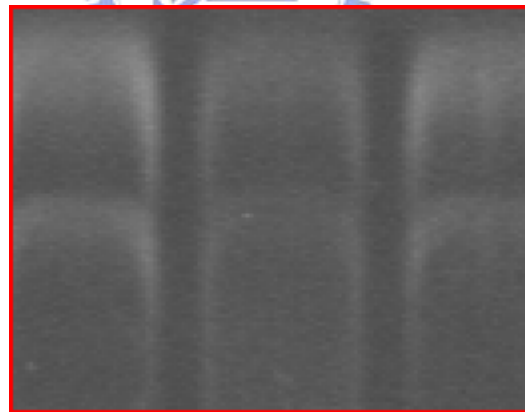
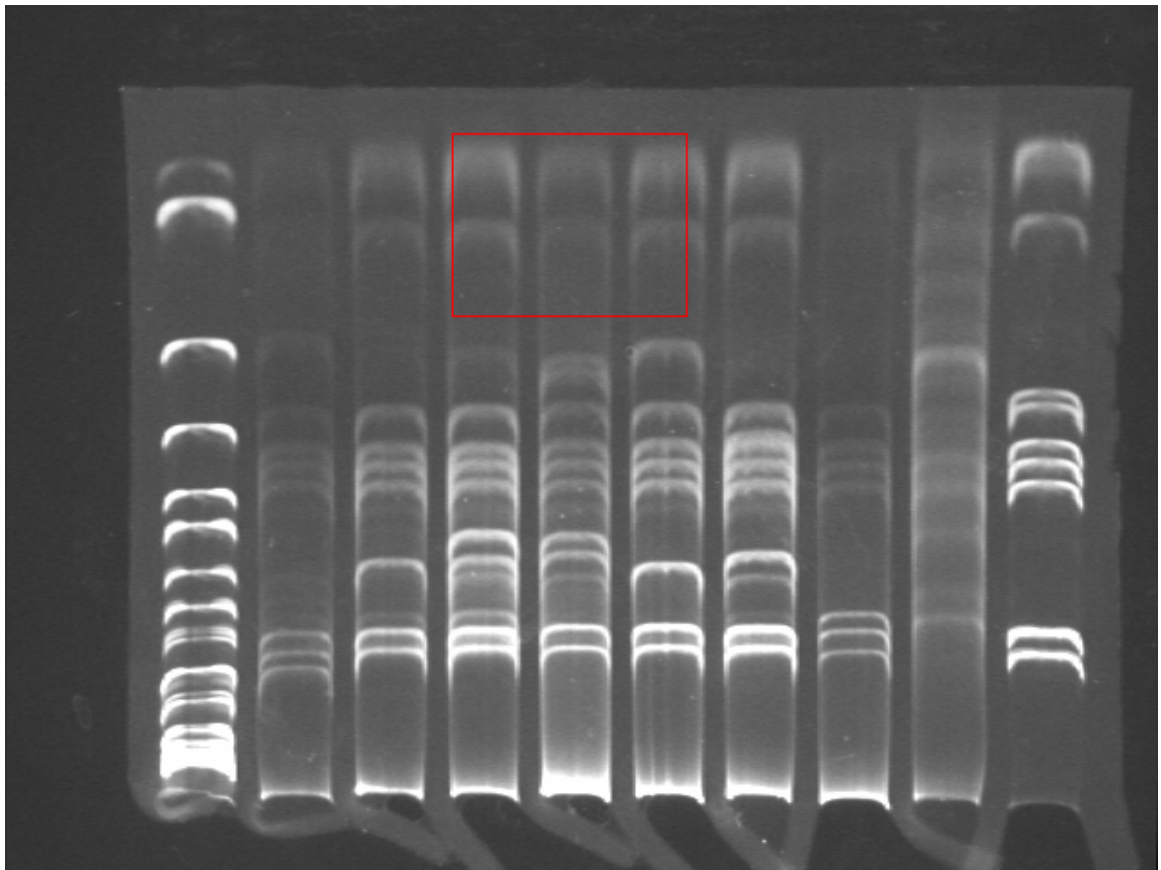
Figs 3-4 (a), (b), (c), and (d) show the spectrum and histogram before and after removing the grid-texture frequency. The resulting image $f_2(x, y)$ is clean and free of grid-texture as shown in Figs 3-3. (c) and (d).



(a)

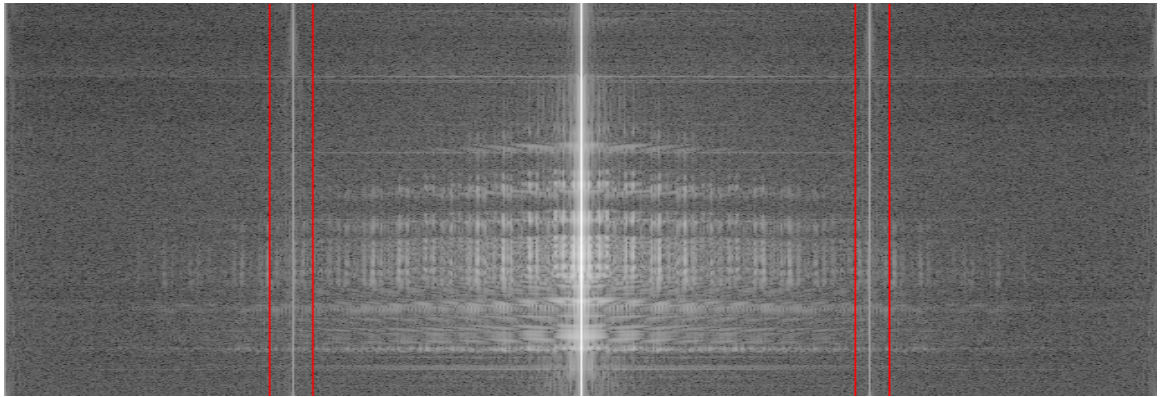


(b)

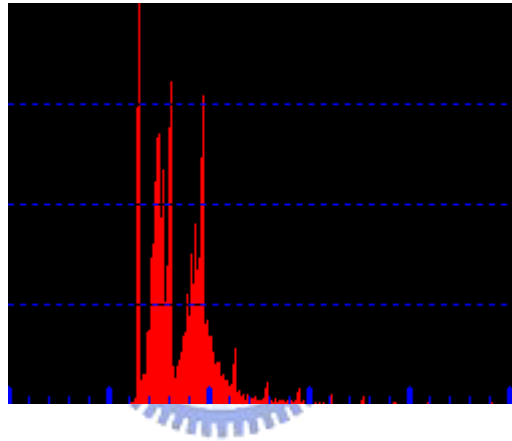


(d)

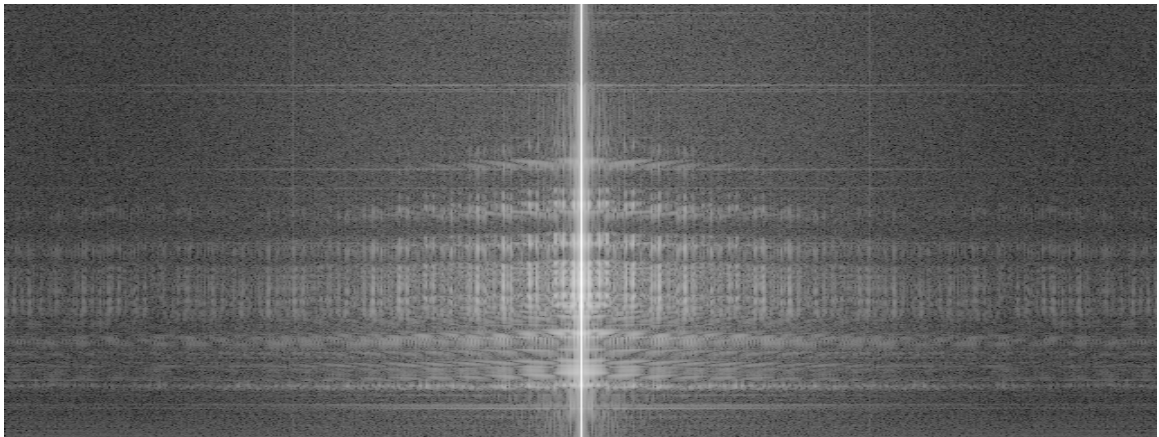
Fig. 3-3. (a) Original image. (b) Zoom in an area of the original image. (c) After removing the grid. (d) The same zoom in area with the grid-texture removed.



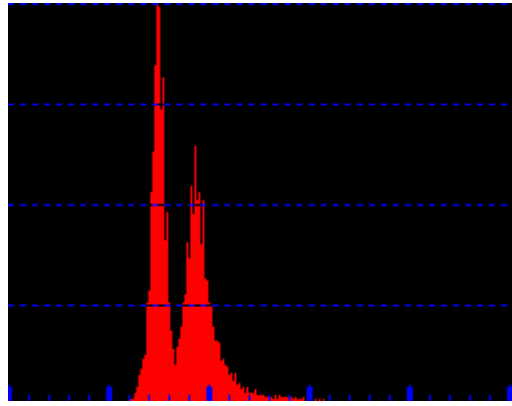
(a)



(b)



(c)



(d)

Fig. 3-4. (a) The spectrum of $f(x,y)$. There are two peaks within the two pairs of red lines. The gray scale is logarithmic for visualization purposes. (b) Histogram of $f(x,y)$ (c) Spectrum after eliminating the grid-texture frequency. The gray scale is also logarithmic. (d) Histogram after eliminating the grid-texture.

The second task in background removal is to set the intensities of those pixels not on the bands to zero. These background pixels generally have lower intensity than the pixels on the bands. In Fig. 3-4 (d), the threshold is set as the closest gray-level corresponding to the minimum probability between the maxima of two normal distributions, which results in minimum error segmentation. An optimal threshold can be solved in [28]. The result after background removal is shown in Fig. 3-5.

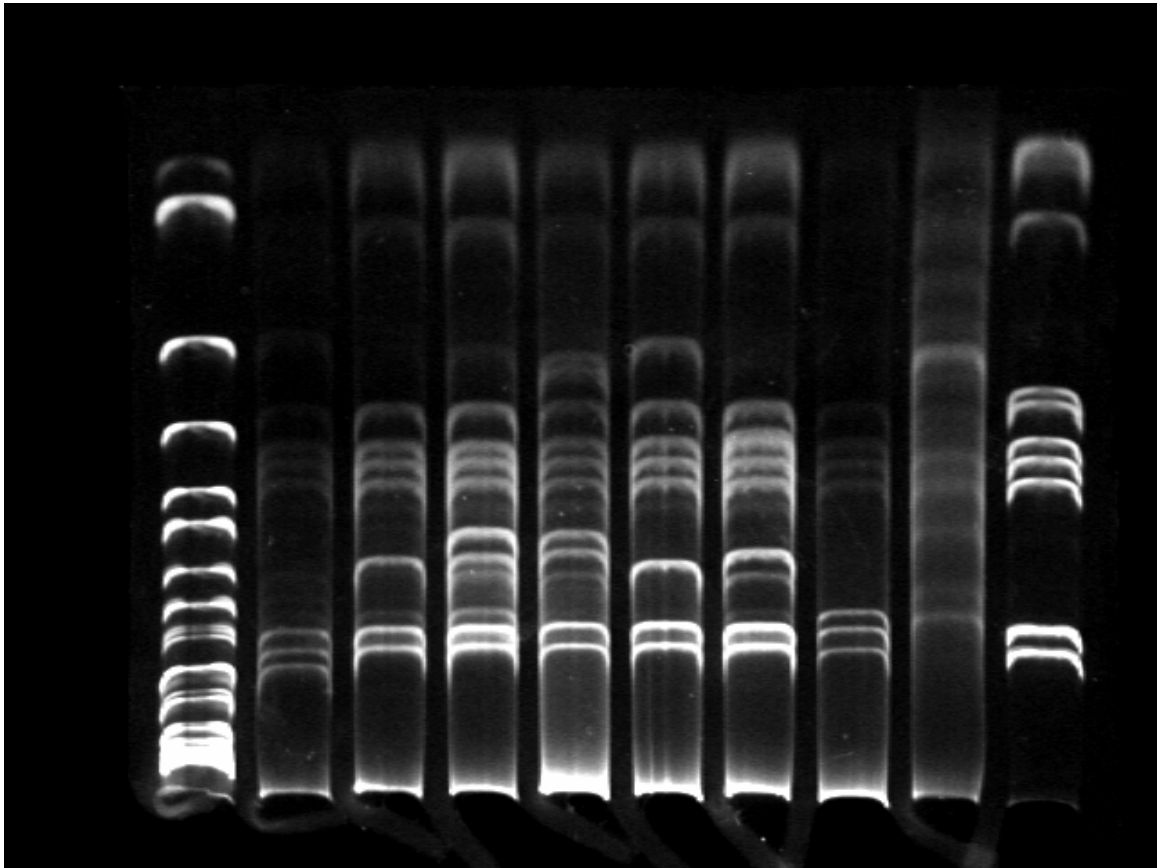


Fig. 3-5. An image after background removal.



2.2 Lanes and Bands Identification

Some observable properties of bands and lanes are presented before presenting the proposed method.

1. The bands close to the top are wider than those close to the bottom of the image.
2. The intensity of the band closest to the bottom is higher than that of the bands closest to the top.
3. The shape of the band is a concave downward curve.
4. The bands on different lanes may have different shapes.
5. The shapes of the bands on the same lanes are similar.
6. Consecutive bands in a lane could be very close in shape.
7. A band could break into several fragments due to noise.

The method for segmenting bands and lanes was designed based on the properties stated above. Band and lane segmentation consists of several steps. The first step is to enhance the bands. The skeleton for each band is then found. Lane segmentation is based on the band skeletons.

The bands are enhanced using the matched filter technique [29-31]. The intensity profile along the vertical line (y-direction) passing through a lane is observed in designing a matched filter (Fig. 3-6). A band profile is bell-shaped and can be approximated using a Gaussian distribution in the y direction, as shown in Eq. (22),

$$D(y) = e^{\frac{-y^2}{2\sigma^2}} \quad -\infty \leq y \leq \infty. \quad (22)$$

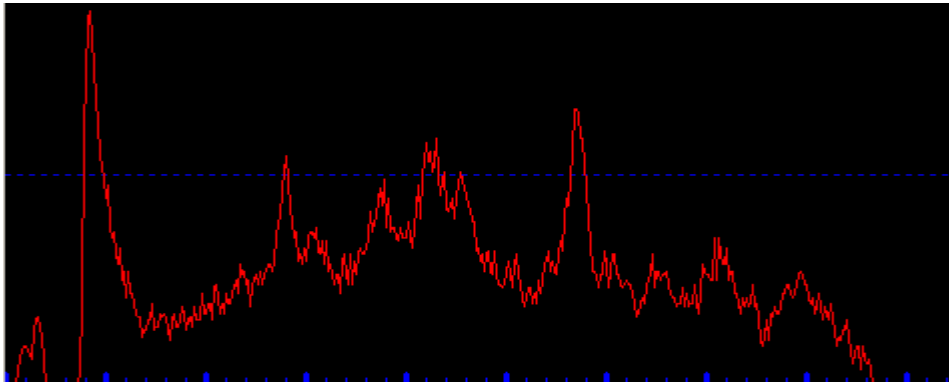


Fig. 3-6. The intensity profile of the scan line for a lane

A 1-D matched filter can be designed to detect the bands because the profile follows a Gaussian distribution.

Because the bands are concave downward curves a 2-D matched filter shown in Eq. (23) is needed.

$$D(x, y) = e^{\frac{-y^2}{2\sigma^2}} \quad -\frac{d_y}{2} \leq y \leq \frac{d_y}{2}, \quad -\frac{d_x}{2} \leq x \leq \frac{d_x}{2}. \quad (23)$$

Two parameters, the width, d_x , and the height, d_y , for the match filter must be determined.

In determining the width, d_x , the bands are not perfectly straight lines and d_x should not be as wide as the length of the bands. The response of a matched filter to a band is small, making the bands difficult to identify. In our experiment, $d_x=5$ is the best value identifying the bands. The height, d_y , of the matched filter depends on the variance, σ^2 , in Eq. (23). After analyzing 350 images (more than 3000 lanes), we concluded that σ varies depending on the location of the band. The bands that are closer to the bottom side have a smaller variance. A traditional matched filter is time-invariant, i.e., σ is a constant. In the case of different σ , a time-variant matched filter is needed. Because the bands that are closer to the bottom side have a smaller σ , and σ increases as the bands are closer to the top of the image, we set σ as a linear function of y , as shown in Eq. (24),

$$\sigma = 1 + c * y / N, \quad (24)$$

where y is the distance between the band and the bottom side of the lane. For a small σ , the Gaussian quickly drops to zero, so d_y is small. Conversely, for a large σ the Gaussian slowly becomes zero, so d_y is large. We used the method in [32] to determine d_y from a given variance. The height is between $-(4\sigma + 3)/2 \leq y \leq (4\sigma + 3)/2$. Based on the above discussions, the matched filter is shown in Eq. (25),

$$D(x, y) = e^{\frac{-y^2}{2\sigma^2}} \quad -\frac{d_y}{2} \leq y \leq \frac{d_y}{2}, \quad -\frac{d_x}{2} \leq x \leq \frac{d_x}{2},$$

$$\sigma = 1 + c * y_1 / N, \quad (25)$$

where $d_y = (4\sigma + 3)/2$, and $d_x = 5$.

Images convolved with the matched filter have enhanced bands. The result after applying the matched filters is shown in Fig. 3-7.

A 2-D convolution operation needs large computing time. The performance can be improved using the convolution theory. The convolution is an associative operation. Thus, the filter

kernel h can be divided into two 1-D kernels

$$h = h_x * h_y. \quad (26)$$

It can be shown that

$$F(f * (h_x * h_y)) = F(f) \cdot F(h_x * h_y) = F(f) \cdot F(h_x) \cdot F(h_y) = F((f * h_x) * h_y), \quad (27)$$

where F denotes the Fourier transform, and '*' denotes the convolution.

In other words, instead of applying the entire kernel h , we apply two 1-D kernels h_x and h_y . If the size of the filter kernel h is K_x by K_y , and the number of pixels in an image is M by N , the 2-D kernel application h needs $K_y K_x MN$ multiplications. When applying two 1-D kernels h_x and h_y separately requires $(K_x + K_y)MN$ multiplications. Thus the computational load can be enormously reduced by splitting a 2-D convolution kernel to two 1-D kernels.

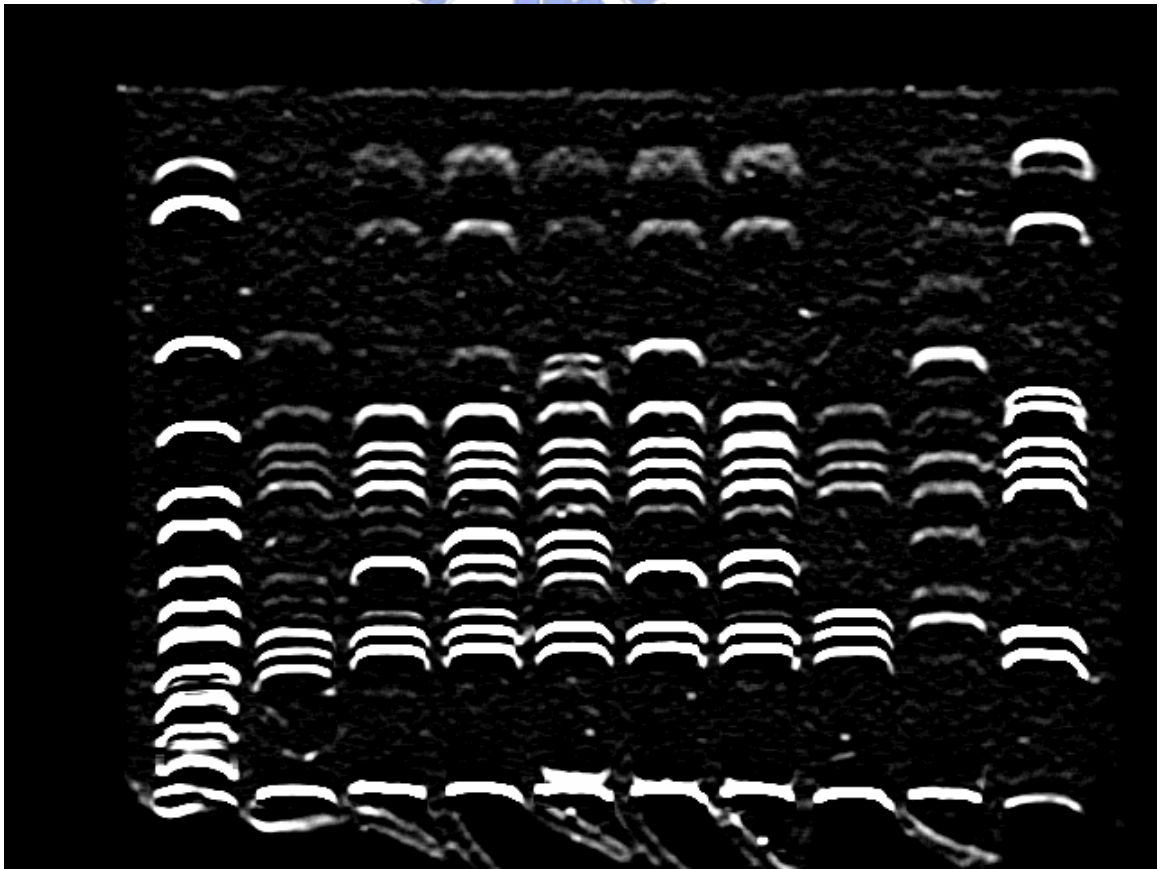


Fig. 3-7. The result from applying the matched filters.

In the images obtained by applying the matched filter the bands close to the top are lighter than the bands close to the bottom. To compensate for this variation, a factor of 5 was used to equalize the pixel intensity. The equalization function is shown in Eq. (28):

$$f_e(x, y) = f(x, y) \cdot \frac{y}{N} \cdot 5 + 1, \quad \forall x, y = 0 \dots N - 1. \quad (28)$$

The method for extracting the bands in the images after the matched filter application is explained in the following step. Given a vertical line passing through a lane, the profile along that vertical line is shown in Fig. 3-8. The center of a band corresponds to a peak on the profile, i.e., the center of a band can be found by determining the local maxima (peaks) on the profile. The intensity threshold is not applicable because the peaks do not have the same height. The *watershed algorithm* [33-34] was used to segment the peaks.

This method is explained using an example. Considering the case shown in Fig. 3-9, there are two objects separated by a peak. To determine the peak that separates the two objects, the image threshold is initially acquired using a low gray level to segment the two objects. The threshold is then gradually increased, like filling water into a container, one gray level at a time. The regions in the object expand as the threshold increases. Because two objects are not allowed to merge, a peak is determined when two objects touch and the final boundaries between adjacent objects are obtained. The process terminates when the threshold reaches the largest gray-level.

The watershed algorithm was used to find the centers of the bands in a lane. After applying Eq. (29), the 1-D watershed algorithm is applied to all of the vertical scan lines in the image. A set of connected peaks is then obtained. Among all of these connected components, most are at the center of the bands while some are just noise. A size filter with a proper threshold is then applied to remove the smaller connected components that are generally noise. The resulting image is a binary image, as shown in Fig. 3-10. Fig. 3-10 shows “broken bands” highlighted

in the red circles. These broken bands will be recovered when the lanes are converted into position vectors.

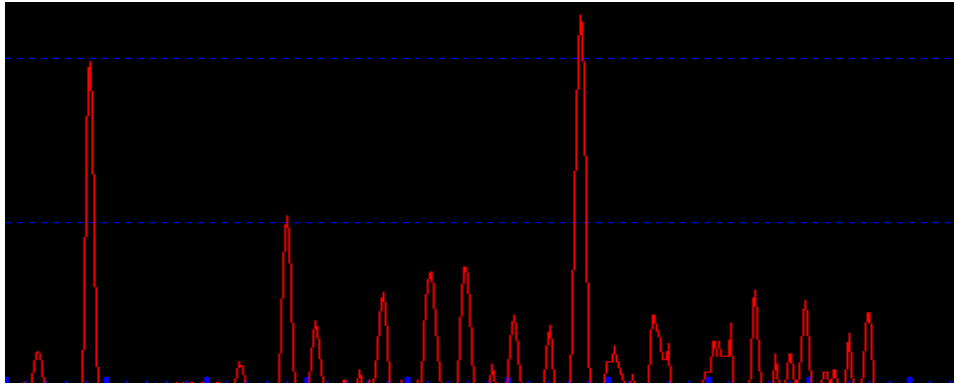


Fig. 3-8. The intensity profile of a lane scan line after filter matching

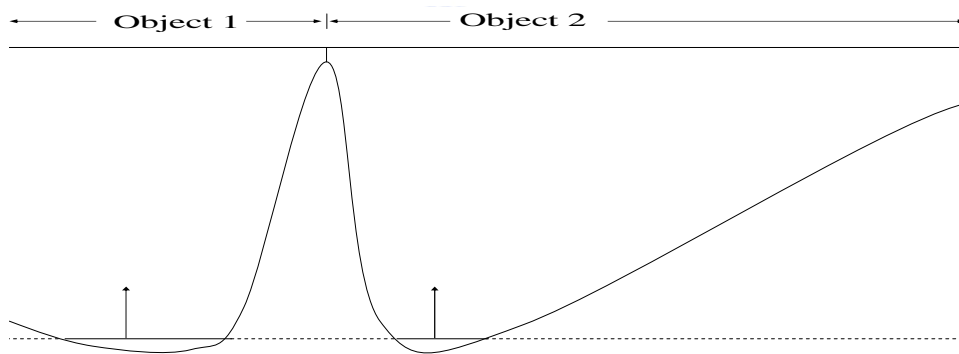


Fig. 3-9. The watershed algorithm.

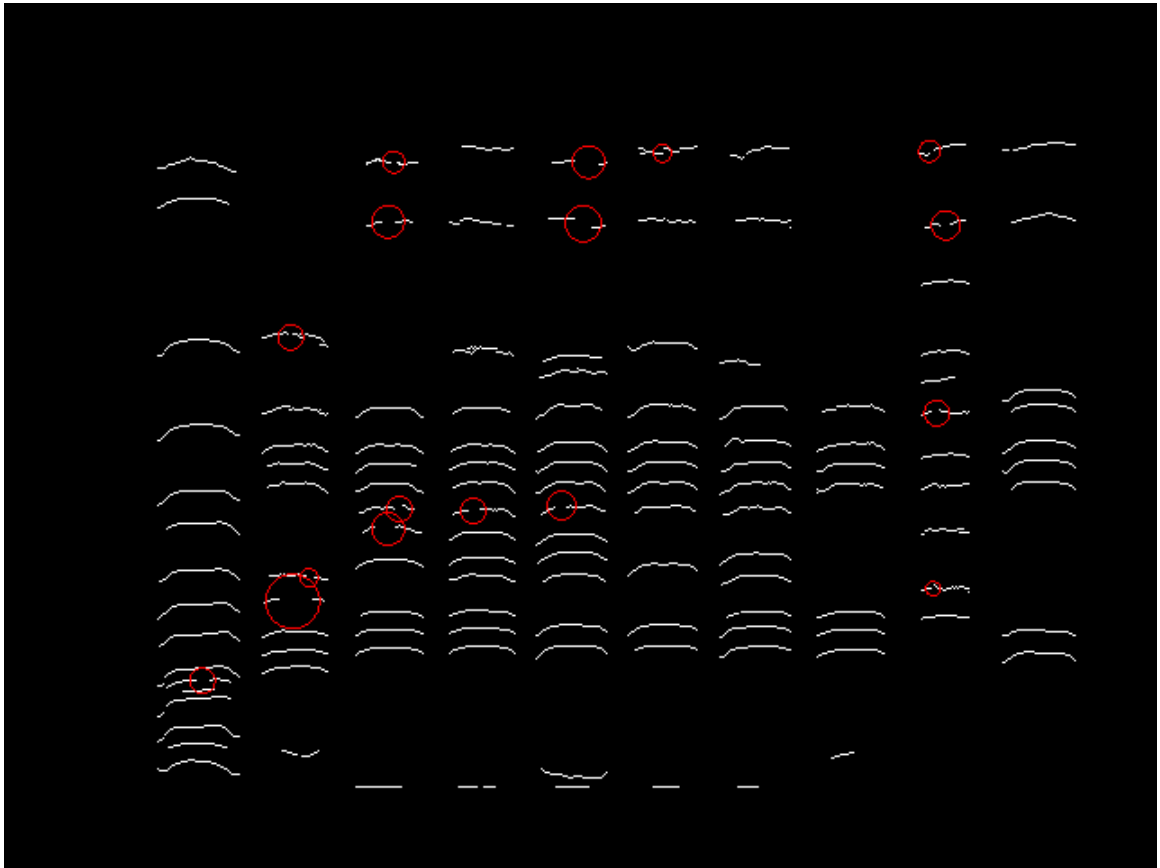


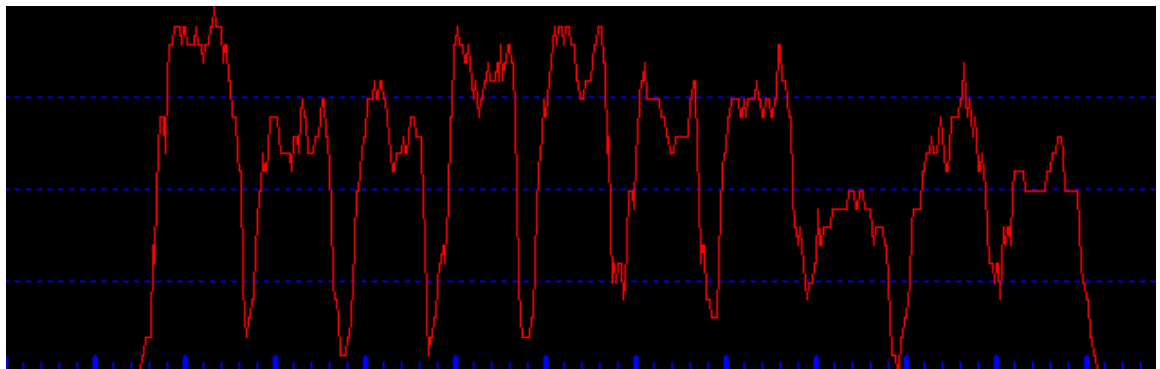
Fig. 3-10. Result from applying the 1-D watershed segmentation algorithm to Fig. 3-7. The break-points are highlighted in the red circles.

In the following the lanes are extracted from the previous obtained segmented bands. To segment the lanes, three parameters are set, TH_{LO} , TH_{HI} , and TH_{Lane} . TH_{LO} is the smallest possible number of bands in a lane. This parameter is set to remove empty lanes from the image. TH_{HI} is a parameter that represents the largest possible number of bands in a lane. The parameter TH_{Lane} defines the smallest lane width.

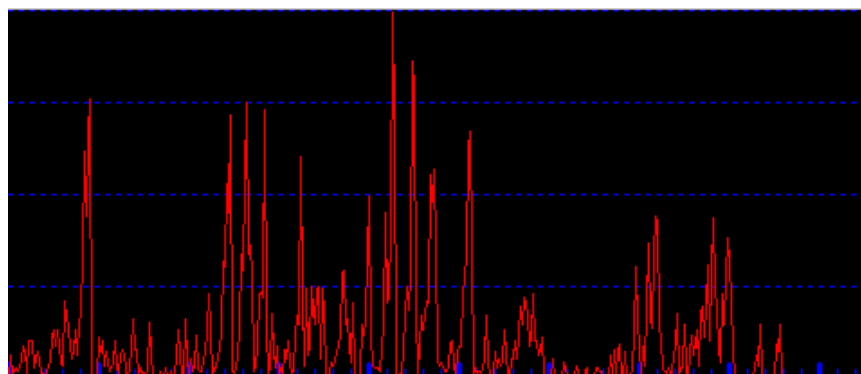
Fig.3-10 is projected into the x -axis first to obtain Fig.3-11 (a). The high-rising portion along the curve of the projection corresponds to a lane. To segment the lanes, we start with the threshold TH_{LO} . This threshold corresponds to a horizontal line $y=TH_{LO}$ that cuts the curve into several connected components formed by the high-rising parts. A connected component is

considered a lane if the width of the connected component is greater than TH_{Lane} . The number of lanes obtained is then counted using this given threshold. The threshold is increased and the steps iterated until the threshold reaches TH_{HI} . The number of lanes obtained is counted each time. The threshold that maximizes the number of lanes is the best threshold.

To determine the top and bottom lane boundaries, the points in Fig. 3-10 are projected horizontally to obtain Fig. 3-11 (b). A threshold is set in which the left most and right most peaks satisfy the thresholds on the top and bottom sides. The lane segmentation result is shown in Fig.3-12.



(a)



(b)

Fig. 3-11. (a) Vertical projection of the points in Fig. 3-10. (b) Horizontal projection of the points in Fig. 3-10.

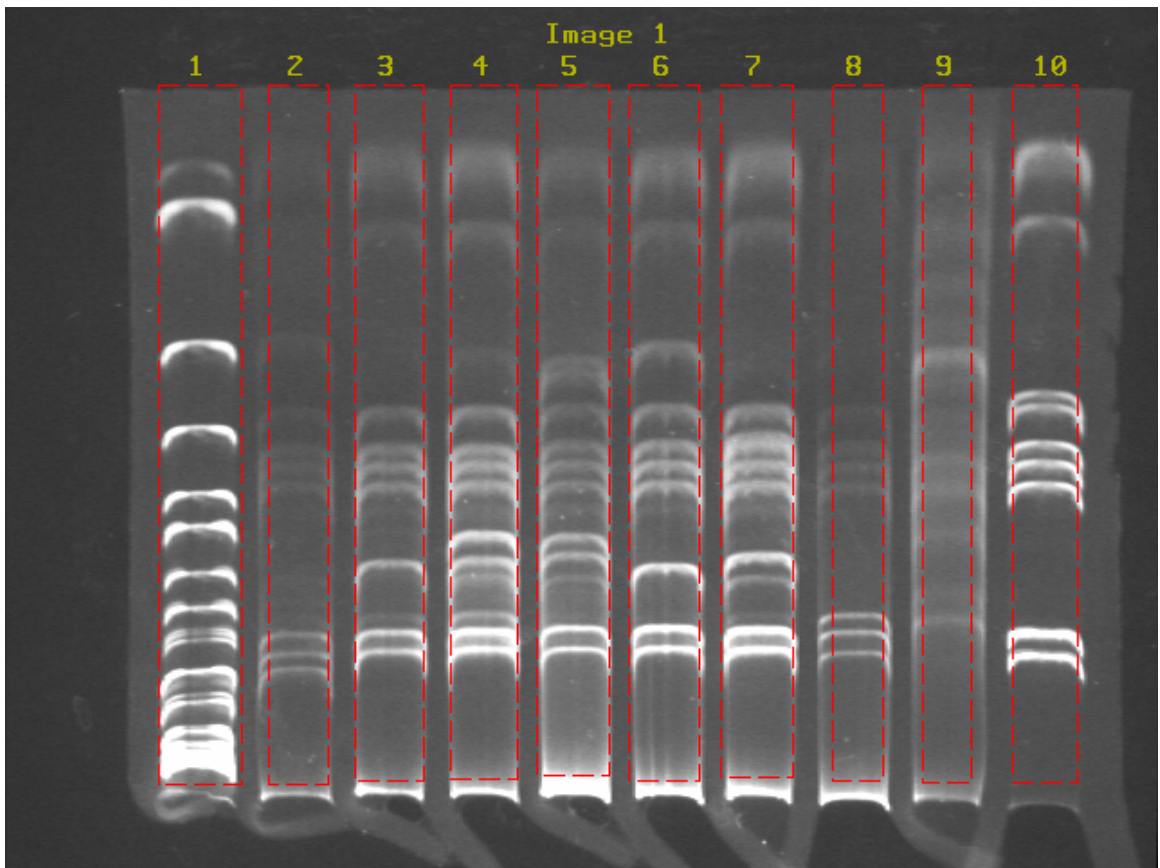


Fig. 3-12. The result of segmentation of lanes.

2.3 Calculate the Lane Position Vectors

On each segmented lane the bands are converted into horizontal line segments. The location vector that describes the location of the bands in this lane is then established. Since there are broken bands, the “break-points” on the band are determined first. The bands are then recovered by connecting the break points. A recovered band should be similar to its original shape. Since we know that the shapes of the bands in a lane are similar, the “average shape” of the bands in a lane can be calculated. A weighted directed graph can then be created from the average shape. Recovering the bands becomes a problem of finding the shortest path in the graph.

To determine the break points, all of the pixels on the lanes are scanned using eight 3 by 3 masks, as shown in Fig. 3-13. If the region covered by the mask is identical to one of the

masks, we say that the pixel in the center is an end point.

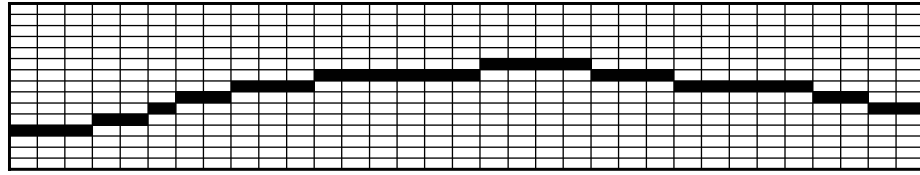
1	0	0	0	1	0	0	0	1	0	0	0
0	1	0	0	1	0	0	1	0	1	1	0
0	0	0	0	0	0	0	0	0	0	0	0
0	0	0	0	0	0	0	0	0	0	0	0
0	1	1	0	1	0	0	1	0	0	1	0
0	0	0	1	0	0	0	1	0	0	0	1

Fig. 3-13. The end point detection masks.

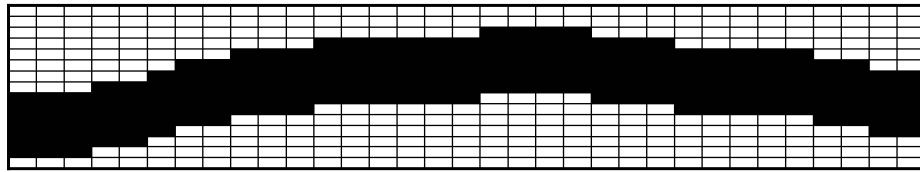
Since the bands in a lane have similar shapes, a mask containing binary values is used to present the “average shape” of the bands in a lane. The method for calculating the average shape is stated in the following.

Suppose that there are n vertical lines passing through a lane. $l_i, i = 1, \dots, n$, are used to denote these n vertical lines from left to right. Let S_i be the set of intersection points of l_i and the skeletons of the bands. Consider a pair of neighboring points, p and q , in a band, p in S_i and q in S_{i+1} . Since the skeleton is 1 point wide, $\overrightarrow{p,q}$ points to one of the following directions, northeast, east, and southeast. The “average direction” from the points in S_i to the points in S_{i+1} is determined using the majority of the directions from the points in S_i to the points in S_{i+1} . The skeleton of the average shape is the sequence of points determined by the sequence of major directions. A skeleton of the average shape of the bands in a lane is shown in Fig. 3-14. (a). The dilation operation was applied to the skeleton in Fig. 3-14 (a) to obtain the average shape shown in Fig. 3-14 (b). The average shape serves as a template mask for scanning the pixels in the lane. If an even number of break points is covered by the mask,

the dynamic programming technique is used to determine the best path to connect the two break points.



(a)



(b)

Fig. 3-14. (a) Skeleton of a band. (b) Dilation of (a).

Suppose that s and t are the break-points in S_i and in S_j to be connected, $i < j$. Let V_k , $k=i+1, \dots, j-1$, be the set of points on l_k covered by the template mask. A weighted directed graph $G = (V, E)$ is then constructed. V is the set of vertices corresponding to the points in the sets V_k , $k=i+1, \dots, j-1$. E is the set of edges that is the union of the following three sets of edges,

$$\left\{ \begin{array}{l} \{ \langle s, v \rangle \mid v \in V_{i+1} \}, \\ \{ \langle v, t \rangle \mid v \in V_{j-1} \}, \text{ and} \\ \{ \langle v_{(p,q-1)}, v_{(p+1,q)} \rangle, \langle v_{(p,q)}, v_{(p+1,q)} \rangle, \langle v_{(p,q+1)}, v_{(p+1,q)} \rangle \mid v_{(x,y)} \text{ is the } x\text{th vertex in } V_x \text{ and } p = i+1, \dots, j-2 \}. \end{array} \right. \quad (29)$$

There are weights on the vertices. The weight of a vertex is the inverse of the intensity of its corresponding pixel in the image after the matched filter enhancement (Fig. 3-7). Given the weighted directed graph G , we can find the shortest path from s to t [35]. Connecting s and t using the shortest path recovers the broken band. The result is shown in Fig. 3-15.

Each band is finally converted into a horizontal line segment that passes through the middle point of a recovered band. The result is shown in Figs. 3-16 and 3-17. The position of the

horizontal line segment is regarded as the position of the band. The position vector of a lane is also obtained.

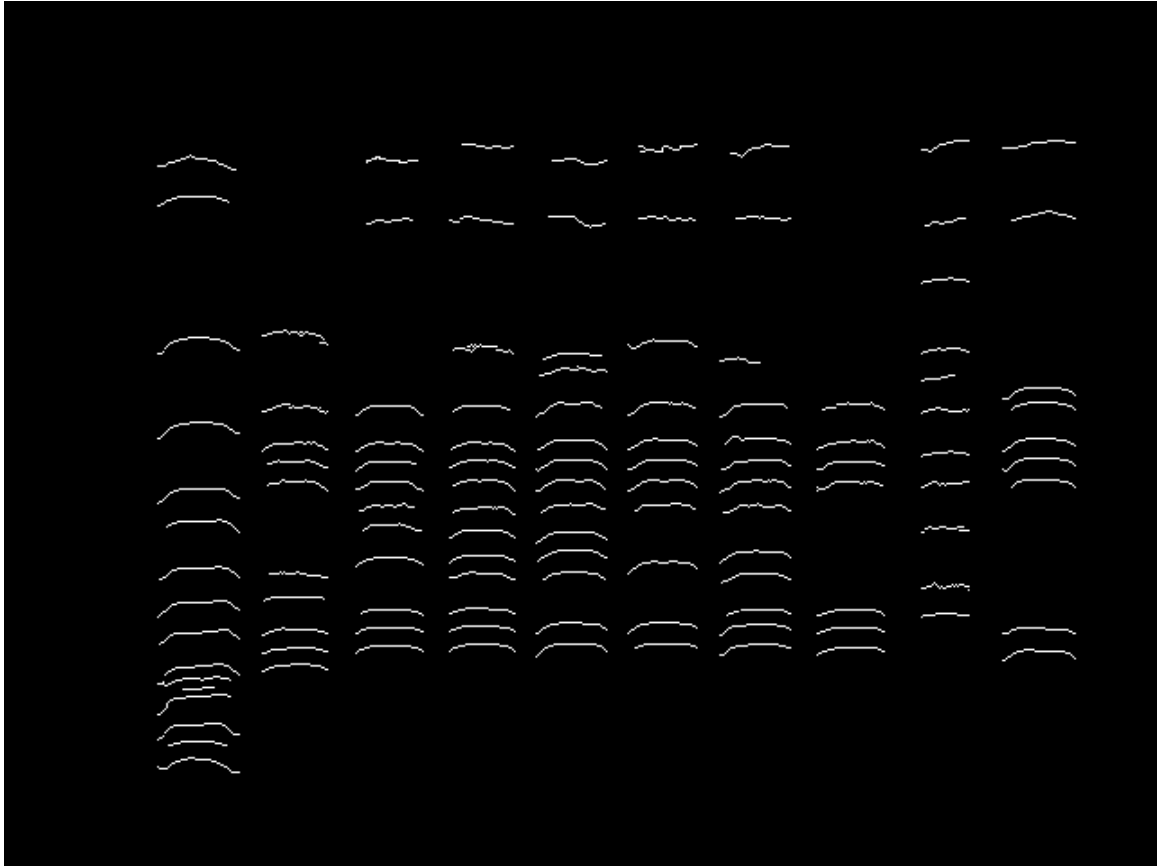


Fig. 3-15. Broken band result from recovering and removing the areas that are not in the lanes.

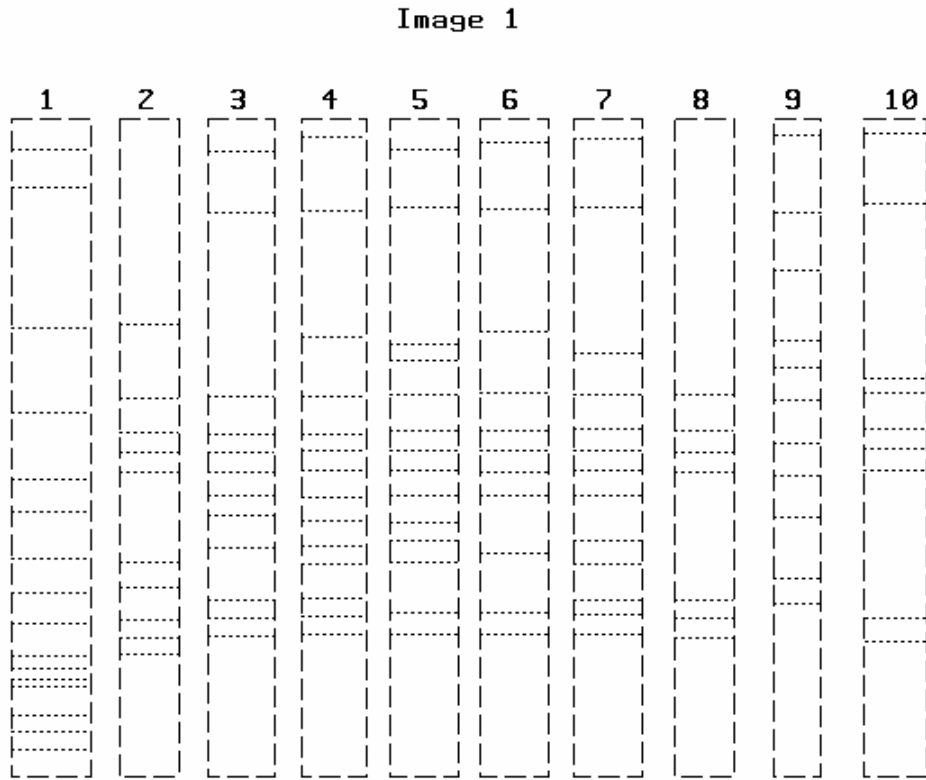


Fig. 3-16. Final segmented bands and lanes.

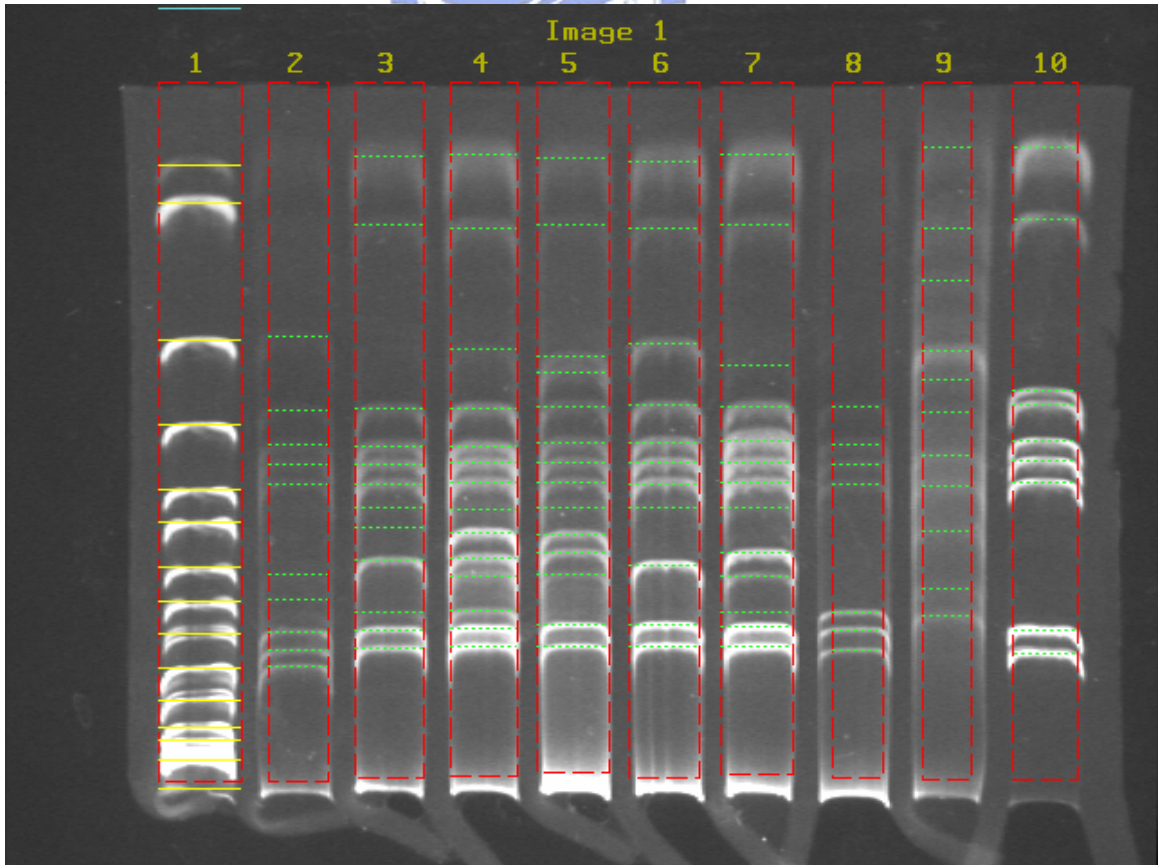


Fig. 3-17. The result is shown superimposed on the original image.

2.4 Position Vectors Normalization

Since there are many factors that affect the relative position between bands and the height of the lane, the position vectors of two identical lanes in different images can be very different. Before lanes can be compared, the position vectors of the lanes must be normalized. There are two parameters that need to be estimated for position vectors normalization, the “offset”, o , and the “scaling factor”, s . The offset and scaling factors for the j th lane in the i th image are denoted o_{i_j} and s_{i_j} .

Since the “Marker” and the “Vector” are common in all images, either the Marker or the Vector can be used to calibrate s and o . In general, the Marker is identical in all images and is the first lane in each image. Furthermore, the Marker generally serves as a reference to justify the variations between two images. The Marker was used to normalize the position vectors between images in this work. The calculated o_i and s_i are then used to normalize the other lanes in the image i . The last lane in an image is called the Vector. All of the lanes contain the subjects in the Vector except the Marker. The Vector subjects were used to normalize the lanes within a GE image in this work.

Since the subjects and their Marker molecular weights are known, the position vector of the Marker can be easily obtained. The position vector of the Marker was normalized in the ranged of 0 to 999 so that the bottom and top side are set at 0 and 999, respectively. We used $\mathbf{v}_{\text{Marker}}$ to denote the normalized Marker.

For a position vector \mathbf{v} , the operations $+$ and $*$ are defined as follows.

1. Let o be a constant, $\mathbf{v} + o = \langle b_1 + o, b_2 + o, \dots, b_m + o \rangle$.
2. Let s be a constant, $\mathbf{v} * s = \langle b_1 * s, b_2 * s, \dots, b_m * s \rangle$.

Let the i th Vector be denoted \mathbf{v}_i and the j th band in the i th lane be denoted b_{i_j} . Given two Vectors \mathbf{v}_1 and \mathbf{v}_2 , two bands b_{1_i} and b_{2_j} are matched if $|d_{(1,2,j)}|$ is less than a given

threshold where $d_{(1,2_j)}$ is the distance between b_{1_i} and b_{2_j} . A best match for \mathbf{v}_1 and \mathbf{v}_2 is obtained using an offset o , such that the number of the matched bands of \mathbf{v}_1 and \mathbf{v}_2+o is maximized and the sum of the differences $d_{(1,2_j)}$ is minimized. If scaling is allowed, the best match for \mathbf{v}_1 and \mathbf{v}_2 is determined as o and s such that the number of matched bands for \mathbf{v}_1 and \mathbf{v}_2*s+o are maximized and the sum of the differences is minimized. To determine the best possible combination of s and o , a brute force approach was used that evaluates all possible combinations of s and o . s is a real number ranging between $1000/N$ and $3000/N$ (N is the number of pixels in the y -direction). The interval is '0.01'. o is a set of real numbers between -500 and 500. The interval is 1. Recall that, bands close to the top have a larger variance than bands close to the bottom. The tolerance for a match varies according to the position of the bands. The following error tolerance function was used to define the threshold,

$$th = th_M + W * \frac{b_{i_0}}{1000}. \quad (30)$$

The error tolerance varies from top to bottom and ranges from th_M to th_M+W . We used 14 and 15 for th_M and W respectively in our experiment.

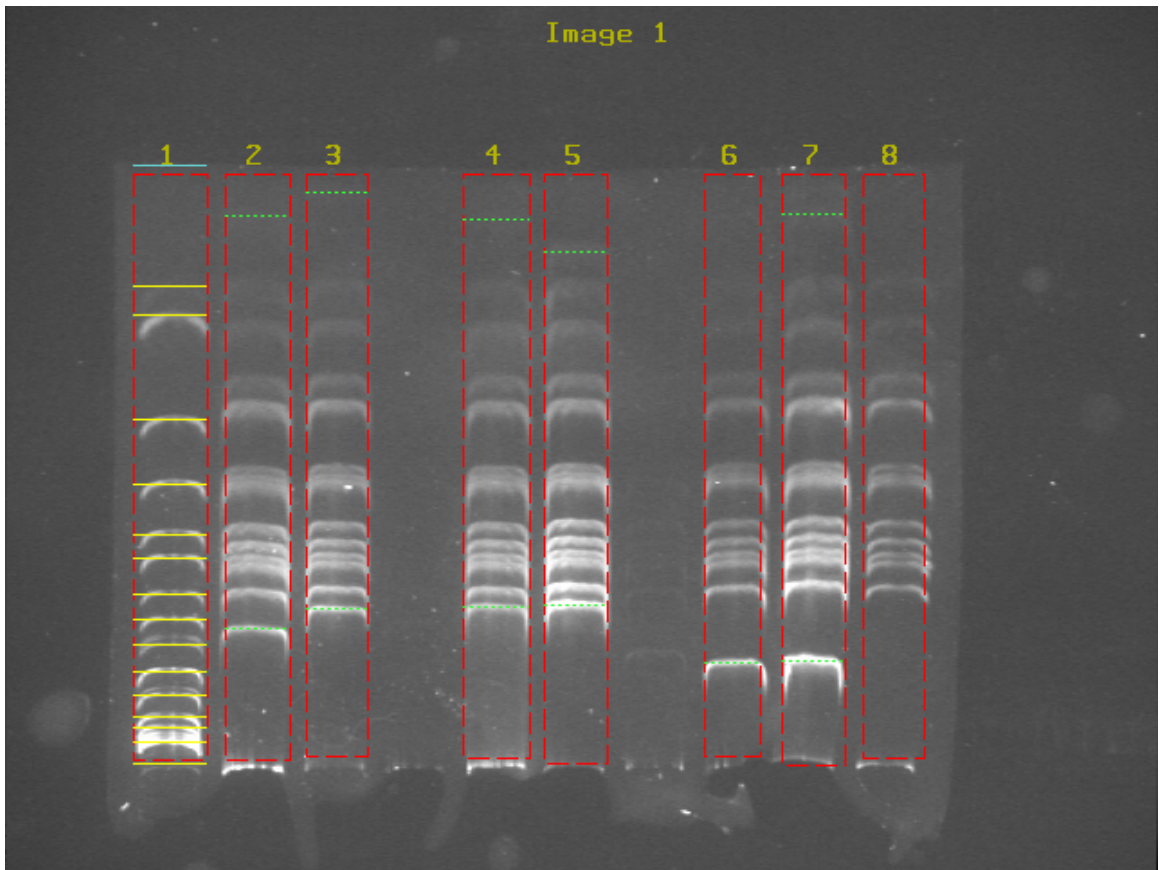
Given a normalized $\mathbf{v}_{\text{Marker}}$ and \mathbf{v}_{i_0} the first lane (the Marker) in i th image, finding the best match between $\mathbf{v}_{\text{Marker}}$ and \mathbf{v}_{i_0} determines the scaling factor s_i and the offset o_i . These factors are applied to normalize all other position vectors in this image. Since there are small variations between the lanes in the same image, the Vector (the last lane) was used to fine-tune the lane normalization in the same image. The normalization procedure is the same as the one mentioned previously except that the ranges for s and o are smaller. The normalized position vectors are ready for lane comparison. Two lanes are identical if and only if all of the bands in one lane have a corresponding match in another lane.

3. RESULTS

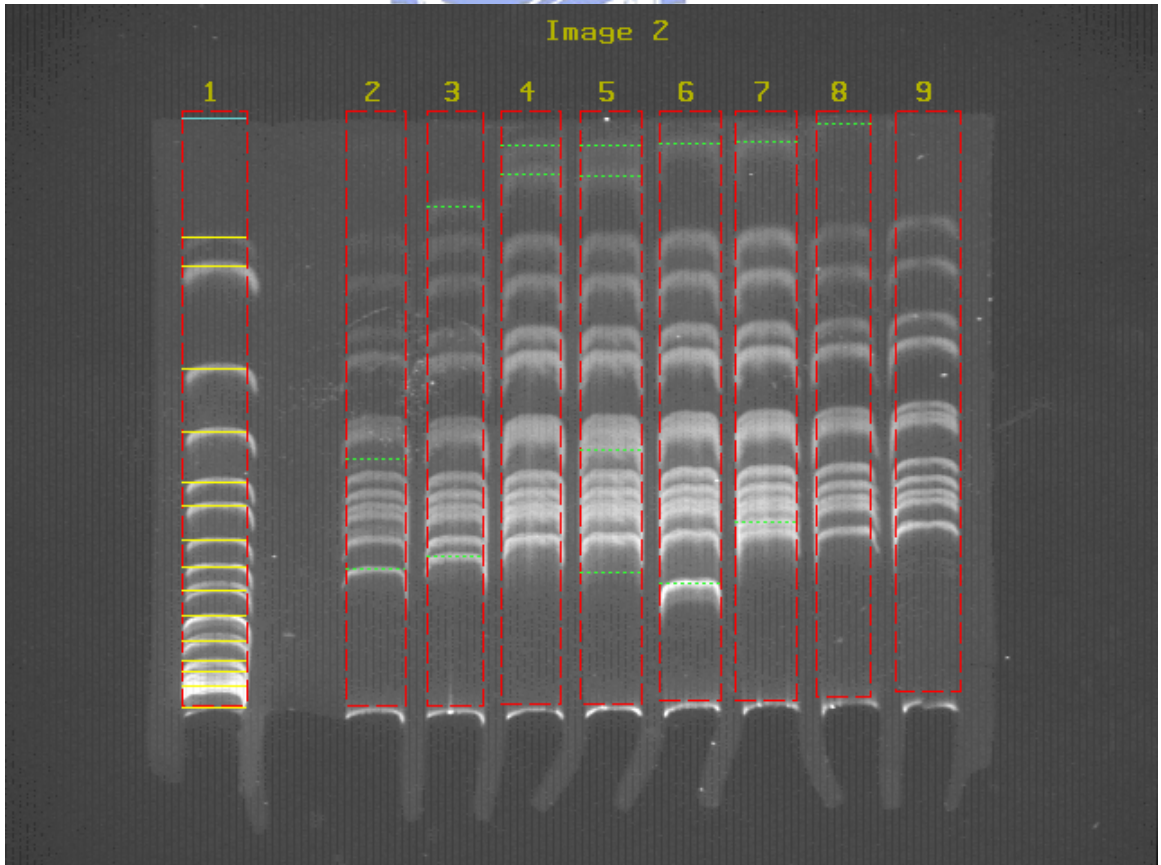
Four sets of test data were used in our experiment. Each set of data contained 47, 47, 131 and 140 images. Each image consisted of about 8 or 9 lanes and there were about 15 bands on each lane including the Vector. These images are the PAGE images used to resolve fragments with sizes less than 20 kb. The subjects are cDNA fragments of fungal genes from an experiment using differential display as the screening method.

The band and lane segmentation results were shown in the previous section. In this section, the vector removal results are presented first. The lane and band segmentation result using a PFGE with *E. coli* genomic sample image is also presented. The lane comparison result is presented last.

The Vector shown in the last lane is common to all other lanes. Removing the Vectors from all of the lanes produces a new lane that contains only the subjects of interest. The threshold defined in Eq. (30) is used to identify the bands in a lane belonging to the Vector. Three Vector removal results are shown in Fig. 3-18. After the Vector is removed only a very few bands are left. The resulting image makes the comparison job easier.



(a)



(b)

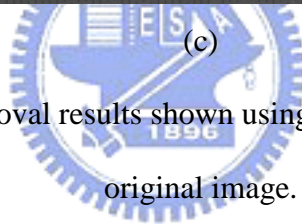
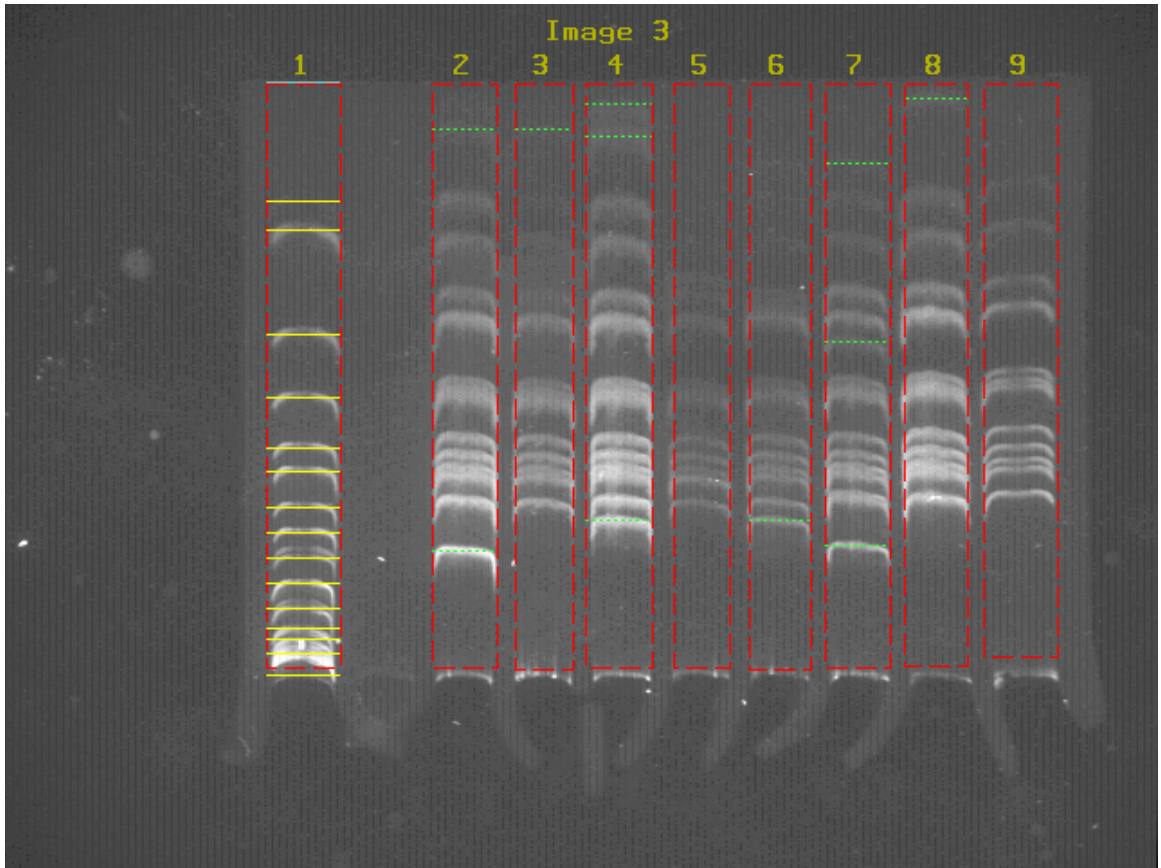
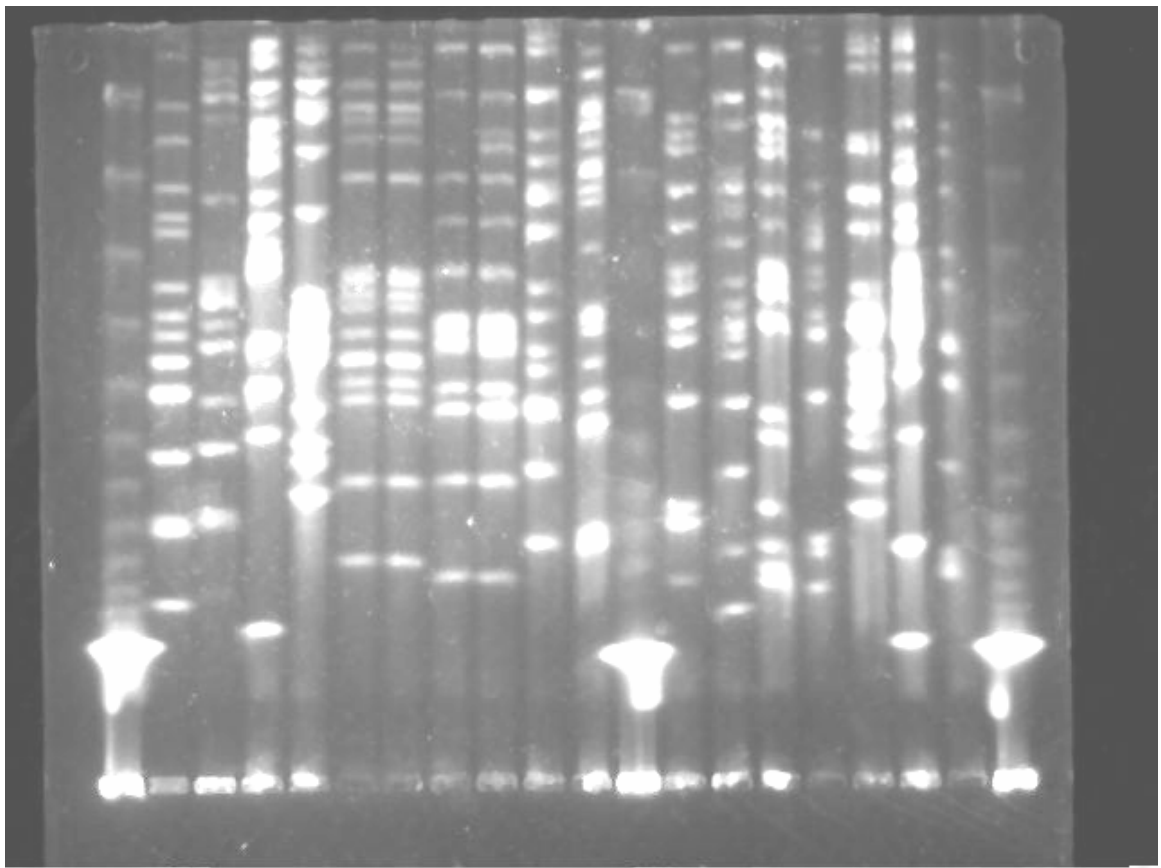
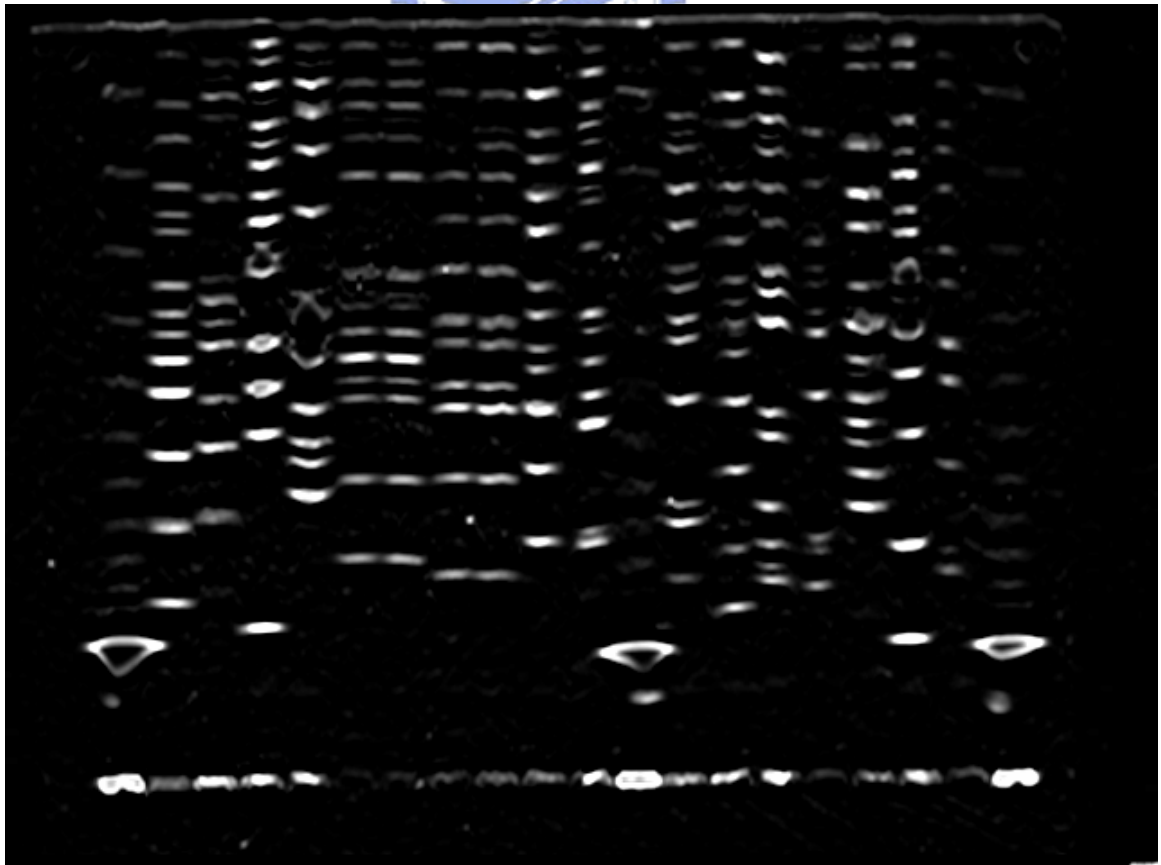


Fig. 3-18. Three vector removal results shown using a green bar superimposed onto the original image.

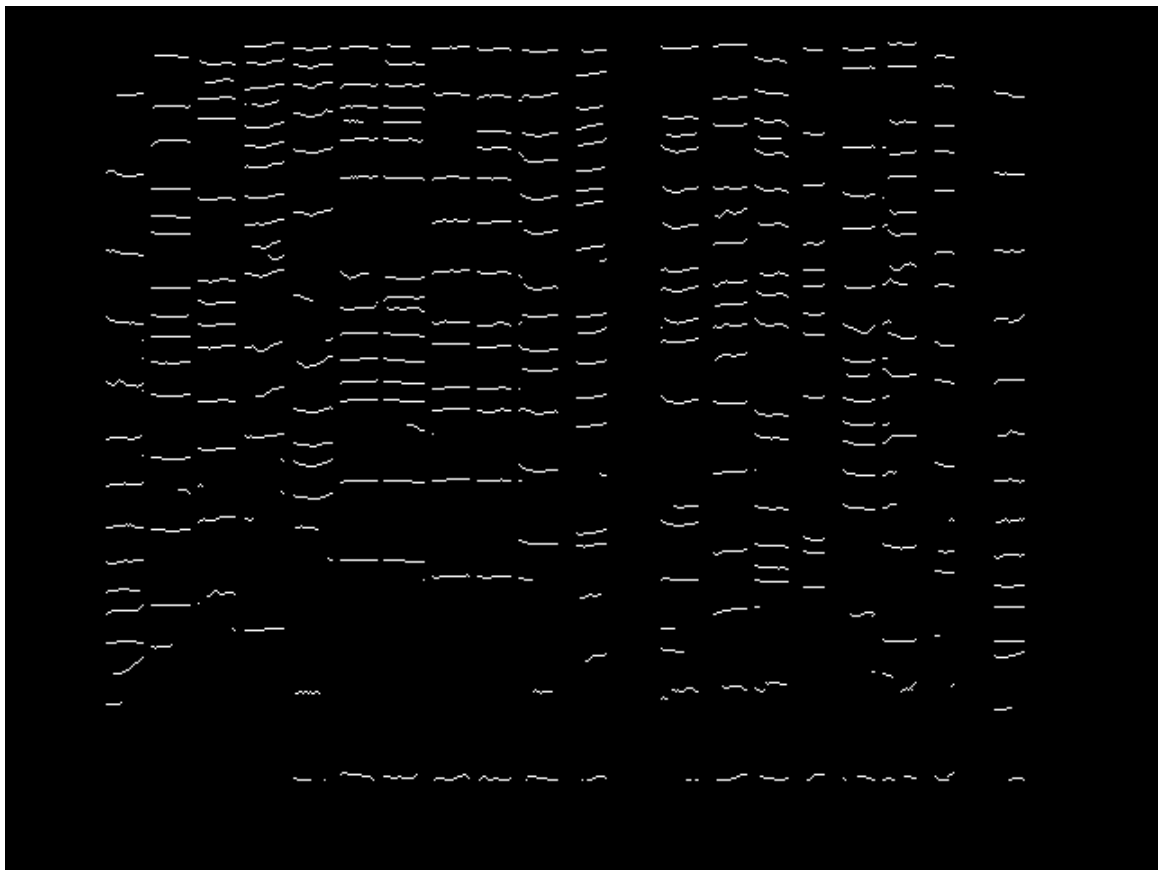
The proposed method was also applied to a PFGE image. This kind of image has a different appearance. The image was obtained from an E.coli genomic study experiment. The set of images is shown in Figs. 3-19 (a) to (f). Fig. 3-19 (a) shows the original image. In (b), the image was obtained by applying a time-variant matched filter. The watershed algorithm was applied to image (b) to obtain (c). The final segmented bands and lanes are shown in (d). Fig. 3-19 (e) shows the result from superimposing the segmented results onto the original image.



(a)



(b)



(c)

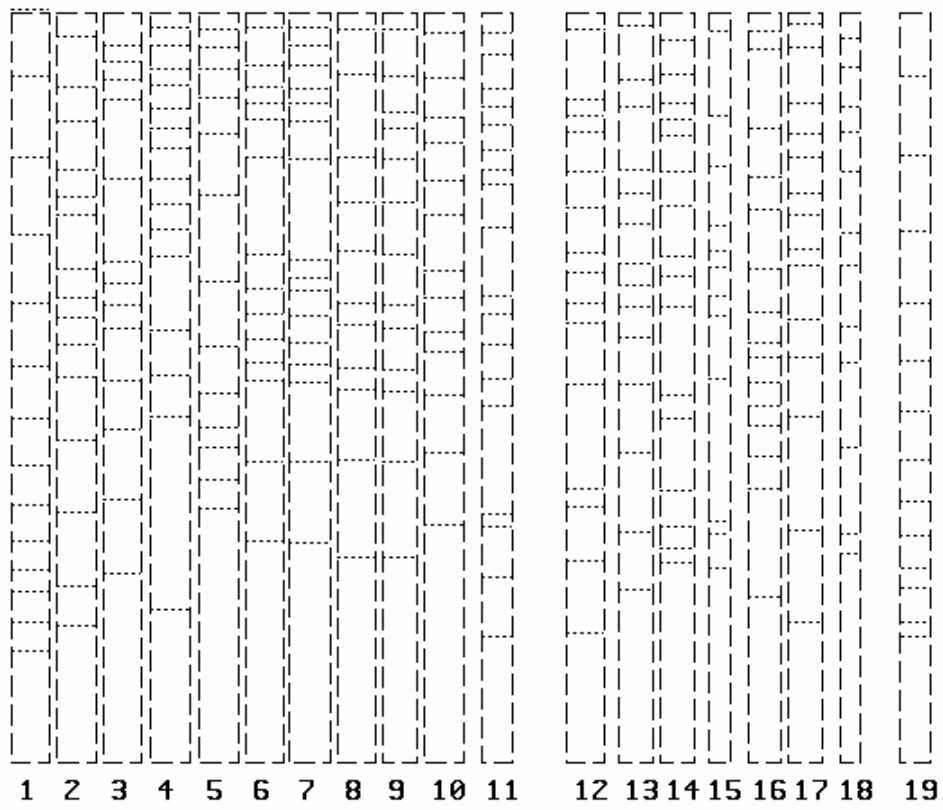
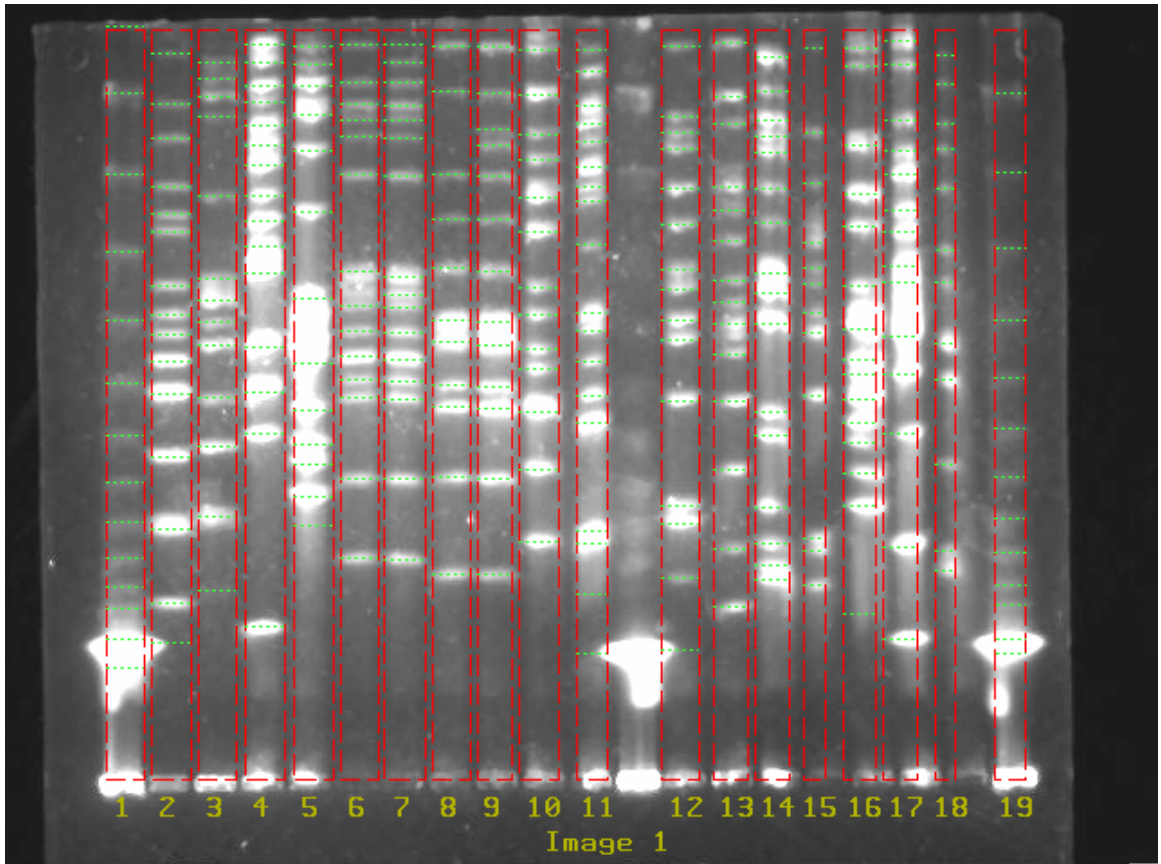


Image 1

(d)



(e)

Fig. 3-19. (a) Original Image (b) Result from applying a time-variant matched filter (c) Result from applying the 1-D watershed segmentation algorithm to (b). (d) Final Segmented Bands and Lanes. (e) The result is shown superimposed onto the original image.

The main goal of this work was to identify identical lanes. After comparing all pairs, our method generates a report, shown in Fig. 3-20. In this report, the identical pairs are listed and the number of differences between the lanes is also shown.

```

less than 0 differenc(es) :
1-5,2-3,3-6,
2-8,3-8,

less than 1 differenc(es) :
1-2 @ 3-3=1,
1-4 @ 3-3=1,3-4=1,
1-5 @ 2-3=0,3-6=0,
1-6 @ 3-5=1,
2-3 @ 1-5=0,3-6=0,
2-4 @ 2-8=1,3-2=1,3-3=1,3-4=1,3-8=1,
2-6 @ 3-2=1,3-8=1,
2-7 @ 2-8=1,3-8=1,
2-8 @ 2-4=1,2-7=1,3-5=1,3-8=0,
3-2 @ 2-4=1,2-6=1,
3-3 @ 1-2=1,1-4=1,2-4=1,3-5=1,
3-4 @ 1-4=1,2-4=1,
3-5 @ 1-6=1,2-8=1,3-3=1,3-8=1,
3-6 @ 1-5=0,2-3=0,
3-8 @ 2-4=1,2-6=1,2-7=1,2-8=0,3-5=1,

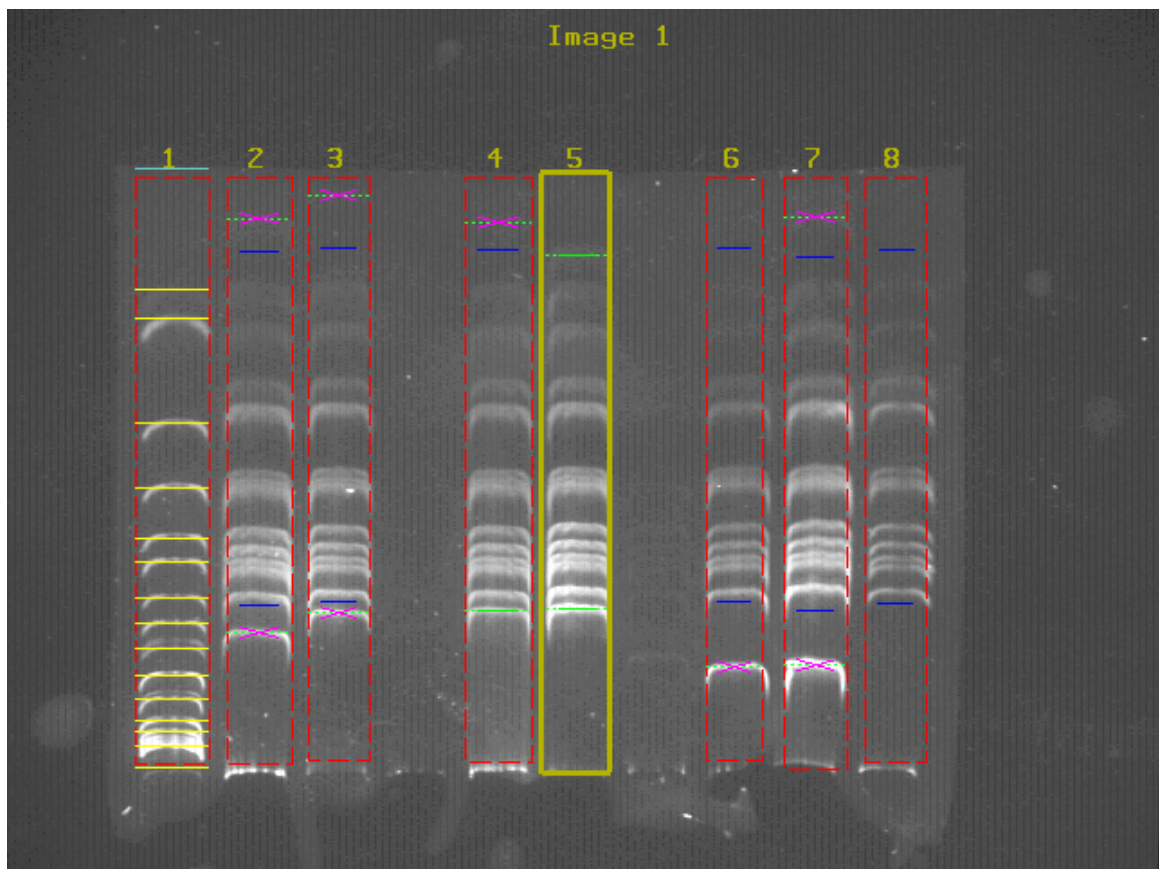
```

Fig.3-20. A report generated by the proposed method

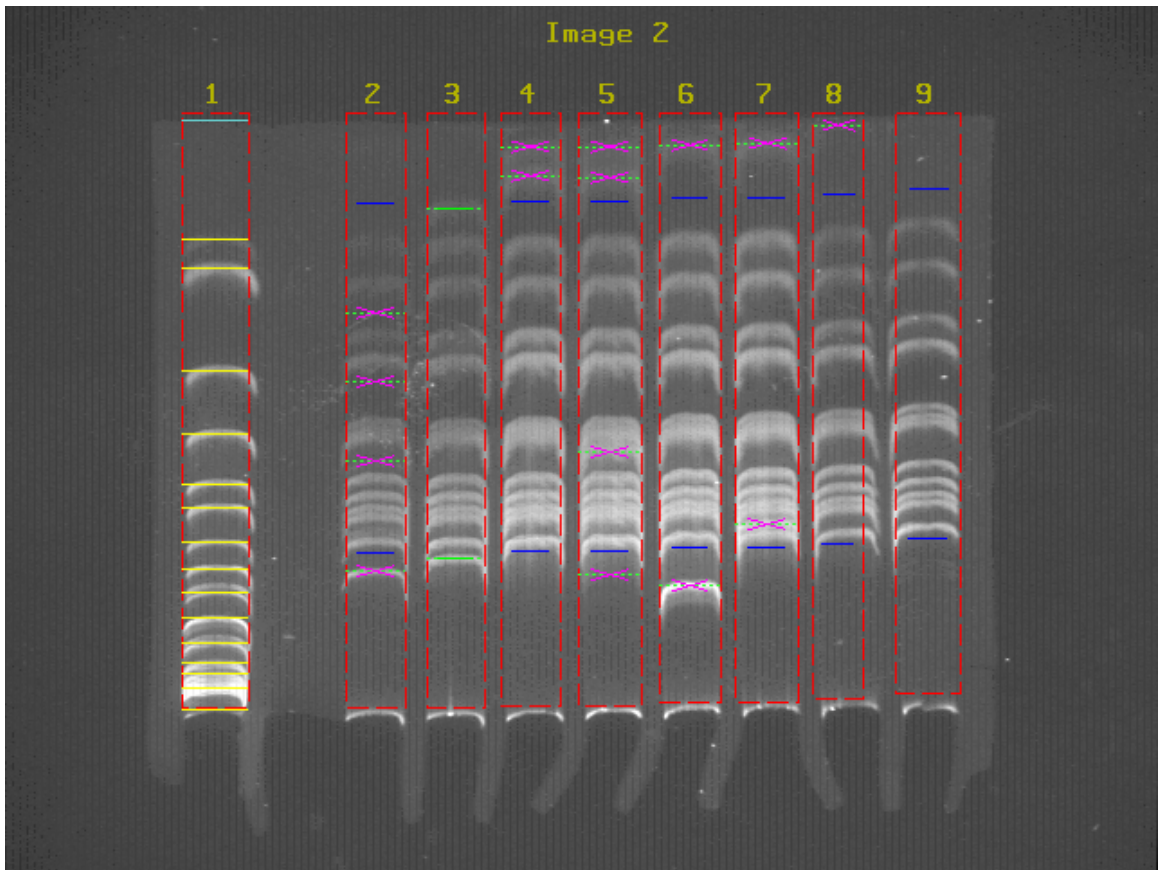
In Fig. 3-20, “*i-j*” means the *j*th lane in image *i*. The report shows that “1-5”, “2-3”, and “3-6” are exactly the same and “2-8” and “3-8” are also identical. “1-2@ 3-3=1” means that there is one different band between “1-2” and “3-3”. “1-4@3-3=1,3-4=1” means that there is one different band between the pairs “1-4” and “3-3”, “1-4” and “3-4”.

A software tool based on the proposed method was developed. This system also provides a way to graphically display the differences. One can use a mouse to select a lane. The software system will show the differences between the other lanes and the selected lane in the images. The matched bands are shown with green bars. The bands that do not match are shown with a violet X over the bands. If there are bands on the selected lane that do not appear in the other lanes, these bands are shown by a blue bar. In Fig. 3-21 lane 5 in image 1 is selected. Lane 5 in the image 1 is highlighted with a bold yellow rectangle. We can see that “1-5”, “2-3”, and “3-6” are exactly the same.

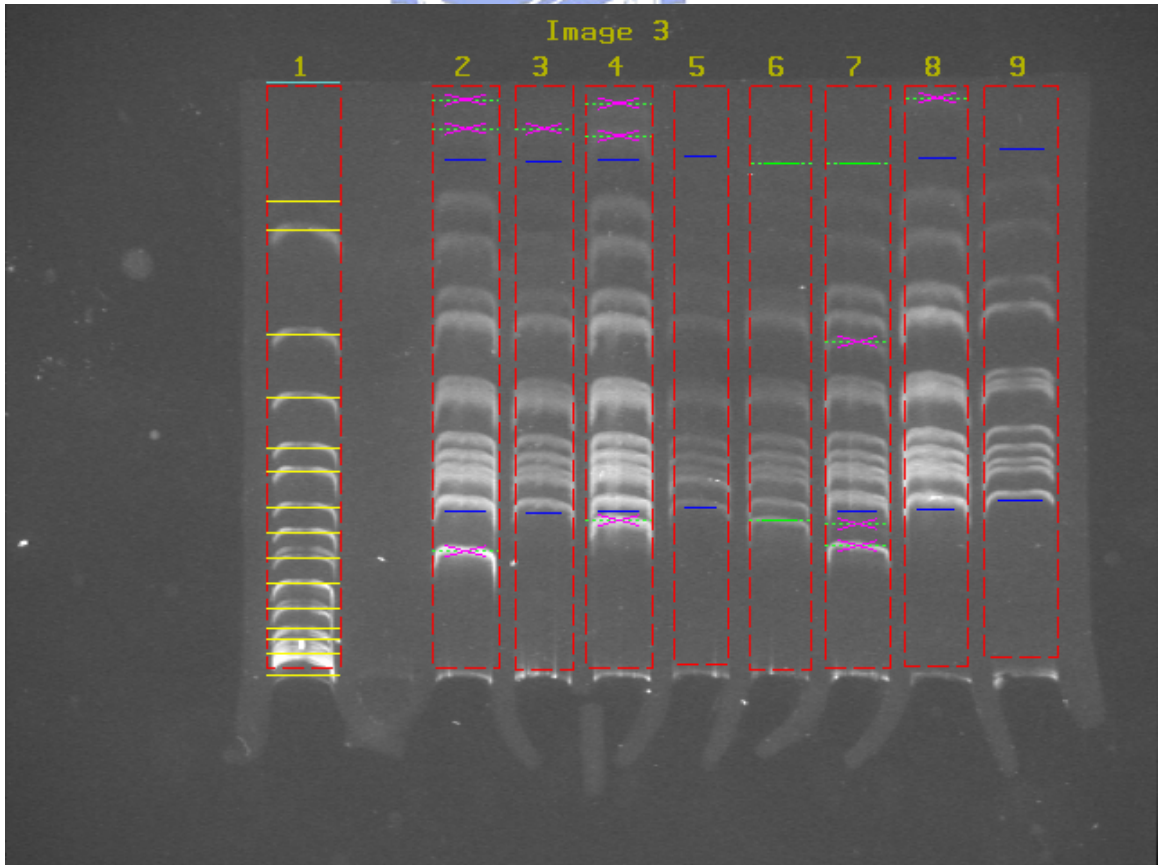
A screen shot of the developed software system is shown in Fig. 3-22. We verified the results using human comparisons. The correctness was above 97%. This method was implemented on a PC with a Pentium III (800 MHz) CPU running on the Windows 2000 operating system. The overall execution time for a 640x480 image took less than 8 seconds. If there are 140 images (about 1200 lanes), the total computing time is less than 19 minutes. The time needed for comparing the position vectors can be ignored and a report can be generated in seconds. This system will help biologists save great effort in comparing PFGE images.



(a)



(b)



(c)

Fig. 3-21. The software system shows the differences between the selected lane and the other lanes in the images. (a) Using the mouse to select lane 5. (b) Lane 3 is identical to lane 5 in (a). (c) Lane 6 is also identical to lane 5 in (a)

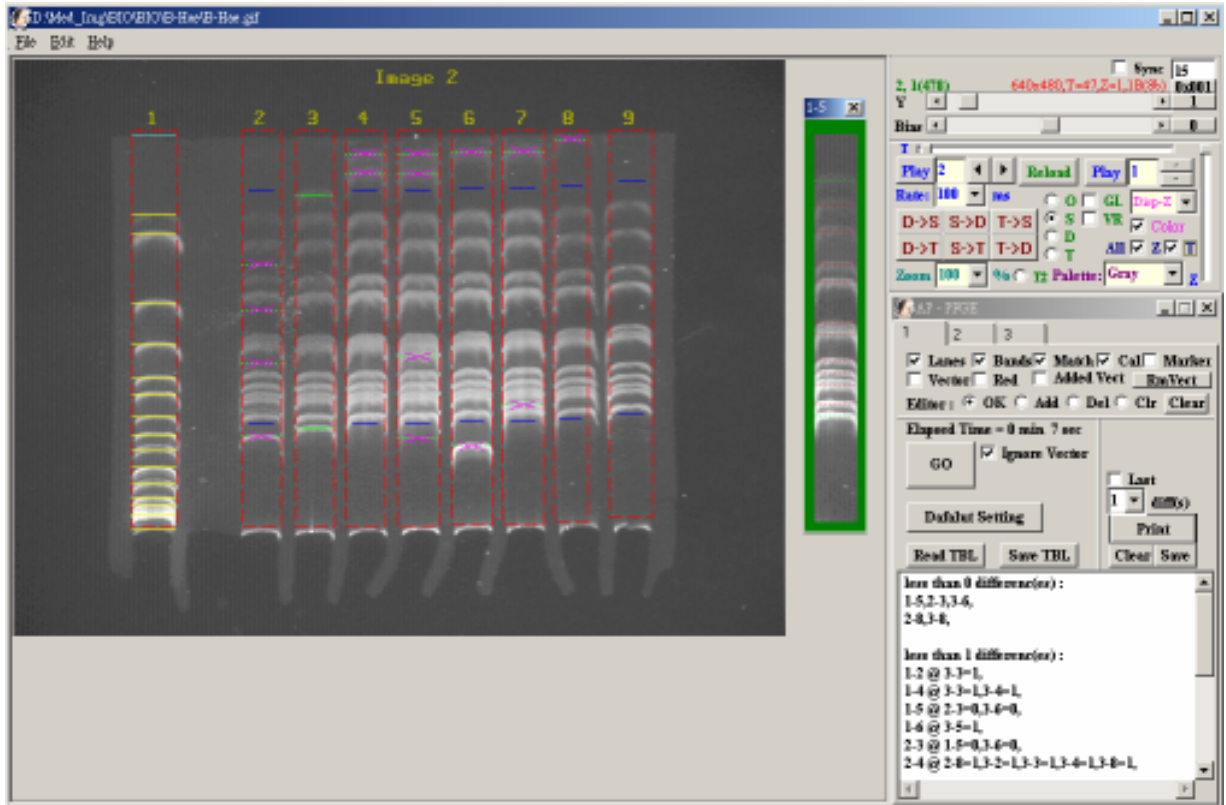


Fig. 3-22. A screen shot from the developed software system.

CHAPTER 4

A Computer Method for ELISA Spot Assay Analysis

The ELISA (Enzyme-Linked Immuno-sorbent Assay) Spot Assay is a method widely used by immunologists to enumerate cytokine-producing cells within a specific cell population. The ELISA results are presented in an image containing numerous colored spots. We present a method to identify the spots in the image and report on important statistics regarding the spots in the image. The proposed method employs color analysis in the CIE $L^*u^*v^*$ color space and matched filter technique. The system is trained to obtain a standard color for the spots and calculate the color differences between the spots and background in the $L^*u^*v^*$ space. Matched filters are then used to remove noise and enhance the spots in the color difference map. Intensity thresholding is applied to obtain a binary image in which the pixels in the spots have a gray scale of 1 while the gray scale of the other pixels is depicted as 0. A software system is implemented based on this method to help immunologists analyze the results obtained from the ELISA Spot Assay.

1. INTRODUCTION

The ELISA Spot Assay is designed to detect cells that produce cytokines [36]-[38]. Cytokines are proteins readily secreted by immune cells upon stimulation by the antigens they recognize or by mitogens. The experimental steps are described as follows. Test wells are coated with anti-cytokine antibody (capturing antibody) before the cells are added. A certain number of cells and antigen are added to the pre-coated wells. During incubation the cells are stimulated to secrete cytokine. The precoated antibody captures the secreted cytokine. After washing, a biotinylated secondary anti-cytokine antibody (detecting antibody that recognizes different epitopes on the cytokine from the capturing antibody) and enzyme-avidin

complex are added in sequence. A color reaction (red in this case) specific to cytokine-secreting cells occurs as a result of this enzymatic reaction. Each red spot represents one cytokine-secreting cell.

To analyze ELISA Spot Assay results, immunologists must know the numbers of spots, the distribution and size of the spots, and the mean and standard deviation of the spot sizes. Because these spots can number in the hundreds in each 70 mm diameter well, counting the spots is labor intensive work even when one uses a dissecting microscope. To overcome this problem, a computer method, that helps immunologists calculate the important spot statistical values, is needed.

Previous related works can be found in [39-40]. In [39], an automatic method for particle detection from electron micrographs was proposed. Distance transform and the Voronoi diagram were used for detection of critical features as well as for accurate location of particles from the images or micrographs. The method could only find fixed size disks. In our case, size of spots is not fixed. In [41], an automatic circular decomposition algorithm applied to blood cells image was proposed. The method used polygonal approximation, curve segmentation, circle modeling, circle adapting, and circle merging to find various sizes of circles. The method needed edge detection as the first step for preprocessing. Unfortunately, in most of the cases, spots do not have obvious edge. In [42], automatic particle detection through efficient Hough transforms was proposed. The method could find various size circles. But this method also needed edge detection before the Hough transform can be applied. In [40] a clustering-based method for particle detection is proposed. This method used a clustering-based method based on the gravitation to classify discrete points into a particle. It worked quite well for detecting particles from images with very low SNR. Before running the clustering algorithm, intensity thresholding is required. Since the boundaries for the spots are not clear, an appropriate threshold value is hard to determine.

In this chapter, we present a method for ELISA spot assay analysis. The proposed method employs techniques that include illumination variation elimination, color analysis in the CIE $L^*u^*v^*$ color space, and matched filter to enhance the spots in the image. After the preprocessing steps, intensity thresholding can effectively segment the spots in the image. In this chapter, the proposed method is presented in Section 2. In Section 3, we briefly describe the software developed for this method. The results are shown in Section 4 and the conclusions are in Section 5.

2. METHOD

The most fundamental task involves segmenting the red spots in the well. The proposed segmentation method was designed based on color analysis and the matched filter technique. There are 5 steps in the proposed method. The first step is image preprocessing. Because a light source cannot be placed on the top of the well, the illumination is not evenly distributed over the well surface. The preprocessing step eliminates illumination variations. The second step involves color space conversion. The objective is to determine a uniform color space to linearize the perceptibility of color differences. The third step has two stages. The training stage involves training the system to recognize the color of the spots. In the recognition stage, a color difference map of the image is calculated according to the standard spot color. The fourth step applies a matched filter to identify the spots and remove the undesired noise in the color difference map. Intensity thresholding is then applied to obtain a binary image in which the pixels in the spots are depicted as 1 while the other pixels are depicted as 0. The pseudo code steps of our proposed method are shown in Fig. 4-1.

```
Find Spots(Image I) //Determine the spots in Image I;  
{  
    Eliminate illumination variation;  
    Color space conversion;
```

```

If ( $I$  is obtained from new experiment)
Train the system to establish a standard color;
Compute the color difference map;
Enhance the spots using a matched filter;
Identify the spots in image  $I$ ;
}

```

Fig. 4-1. The pseudo code for the proposed method

2.1 Variable Illumination Removal

Variable illumination causes problems when the intensity threshold is applied. It is necessary to remove these illumination variations. Let $f(x,y)$, $0 \leq x \leq M-1$ and $0 \leq y \leq N-1$, denote an M by N spot image. $f(x,y)$ is the product of the reflectance $r(x,y)$ and the illumination $i(x,y)$ [43] as shown in Eq. (31),

$$f(x, y) = i(x, y)r(x, y). \quad (31)$$

Suppose that the illumination is not evenly distributed over an image. The variation in illumination over the image consists of a low frequency component in the frequency domain. Elimination of illumination variation is carried out using the following steps. We first use a logarithmic operation on both sides of Eq. (31) to obtain Eq. (32). Note that, the right hand side of Eq. (31) is transformed from multiplication to addition.

$$\ln f(x, y) = \ln i(x, y) + \ln r(x, y). \quad (32)$$

We then transfer $\ln f(x, y)$ into the frequency domain,

$$\ln F(m, n) = \sum_{x=0}^{M-1} \sum_{y=0}^{N-1} \ln f(x, y) e^{-2\pi j \left[\frac{xm}{M} + \frac{yn}{N} \right]}. \quad (33)$$

In the frequency domain, a high-pass filter is employed to suppress the low frequency components. We then add a compensation operation back into the image to compensate for the suppressed signal. The high-pass filter, shown in Eq. (34), suppresses the low frequencies and enhances the high frequencies so that the variation in the illumination can be reduced while the edges are sharpened.

$$H(\omega_x, \omega_y) = \frac{1}{1 + e^{-s(\sqrt{\omega_x^2 + \omega_y^2} - \omega_0)}} + A. \quad (34)$$

The response of $H(\omega_x, \omega_y)$ and its cross-section are shown in Fig. 4-2.

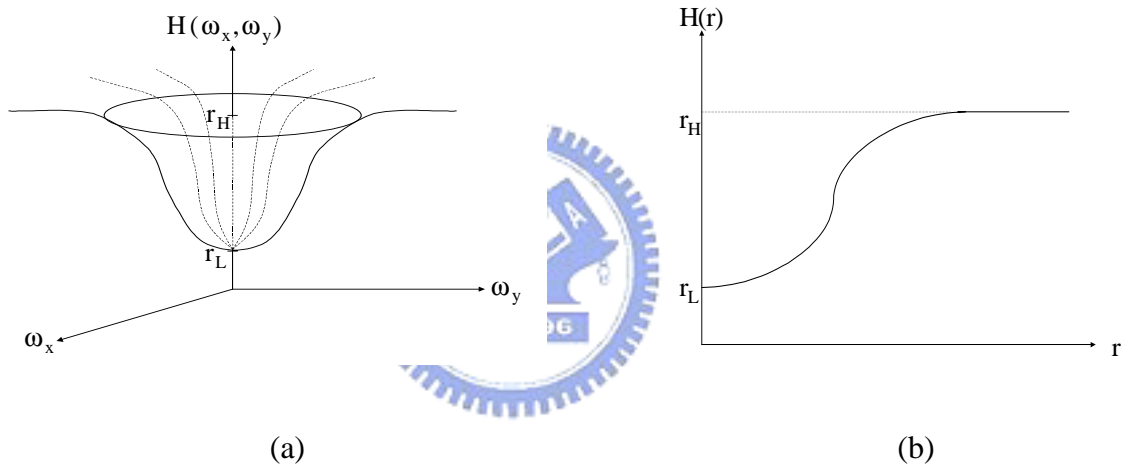


Fig. 4-2 (a) The high-pass filter spectrum. (b) A cross-section of the high-pass filter as a function of the polar angle and frequency. In these figures $r = \sqrt{\omega_x^2 + \omega_y^2}$, $r_L = 1/(1 + e^{s\omega_0})$,

$$\text{and } r_H = 1 + A.$$

Because the spot edges contain high frequency information and the illumination variations usually contain very low frequency information, if the cutoff frequency of $H(\omega_x, \omega_y)$ is not too high, we can preserve the edge information and remove the illumination variation. We used $0.1 f_s$ as the cutoff frequency where f_s is the sampling frequency. In Eq. (35), ω_0 is the cutoff frequency and A is the compensation.

Compensation is required because the high-pass filter removed the low frequencies including the DC term. A is automatically estimated by

$$A = 1 - \frac{1}{1 + e^{(sw_0)}}. \quad (35)$$

Applying the high pass filter (Eq. (34)) to $\ln F(m, n)$ is presented in Eq (36)

$$\ln F_i(m, n) = H(m, n) \ln F(m, n), \quad (36)$$

where $F_i(m, n)$ denotes the filtered image in frequency domain.

The inverse Fourier transform is then applied, as shown in Eq. (37).

$$\ln f_i(x, y) = \sum_{x=0}^{M-1} \sum_{y=0}^{N-1} \ln F_i(m, n) e^{2\pi j \left[\frac{xm}{M} + \frac{yn}{N} \right]} \quad (37)$$

Using an exponential operation restores the filtered signal.

2.2 Color Space Conversion

The spots are extracted based on the differences between the colors of the spots and the background. A proper color space must be chosen before we can calculate the difference between colors. Over 40 color difference formulas were used before the CIE (Commission Internationale de l'Eclairage) recommended two standard color difference formulas, i.e., the CIE $L^*a^*b^*$ and the CIE $L^*u^*v^*$ for surface and lighting industries [44]. These two color difference formulas provide uniform color space. We chose the $L^*u^*v^*$ space [45]. Because video cameras use RGB representation for colors, we converted the color representation from the RGB space into the $L^*u^*v^*$ space [45]. Before the coordinates in the $L^*u^*v^*$ space can be obtained, the representation from the RGB space must be converted into the XYZ space using Eq. (38).

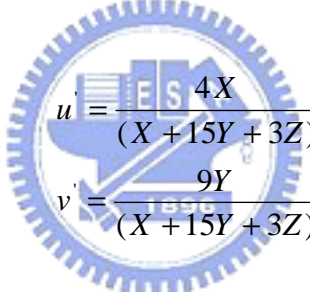
$$\begin{bmatrix} X \\ Y \\ Z \end{bmatrix} = \begin{bmatrix} 0.412453 & 0.357580 & 0.180423 \\ 0.412453 & 0.357580 & 0.180423 \\ 0.019334 & 0.119193 & 0.950227 \end{bmatrix} \begin{bmatrix} R \\ G \\ B \end{bmatrix}. \quad (38)$$

The $L^* u^* v^*$ is based directly on the CIE XYZ. The non-linear relations for L^* , u^* , v^* , X , Y , and Z are given below:

$$L^* = \begin{cases} 116\left(\frac{Y}{Y_n}\right)^{1/3} - 16 & \text{if } \frac{Y}{Y_n} > 0.008856 \\ 903.3\left(\frac{Y}{Y_n}\right) - 16 & \text{if } \frac{Y}{Y_n} \leq 0.008856 \end{cases}, \quad (39)$$

$$\begin{aligned} u^* &= 13 \cdot L^* (u' - u'_n) \\ v^* &= 13 \cdot L^* (v' - v'_n) \end{aligned} \quad (40)$$

In Eq. (40), (X_n, Y_n, Z_n) is the reference white in CIE XYZ. u' , v' , u'_n , and v'_n are given in the following equations,



$$\begin{aligned} u' &= \frac{4X}{(X + 15Y + 3Z)} \\ v' &= \frac{9Y}{(X + 15Y + 3Z)} \\ u'_n &= \frac{4X_n}{(X_n + 15Y_n + 3Z_n)} \\ v'_n &= \frac{9Y_n}{(X_n + 15Y_n + 3Z_n)} \end{aligned}, \quad (41)$$

The daylight standard D_{65} [44] was used as the reference illuminant. The non-linear relationship for Y is intended to mimic the logarithmic response of the eyes. The converted image in color space $L^* u^* v^*$ is denoted $f(x, y)_{L^* u^* v^*}$.

2.3 Train the System and Obtain an Image of the Color Differences

To train the system to recognize a standard spot color, a user interface method is used to select an area $A(x, y)$ in the spot. Suppose there are N pixels in $A(x, y)$, the standard color

$(\mu_{L^*}, \mu_{u^*}, \mu_{v^*})$ is obtained using the equations shown in Eq. (42).

$$\begin{aligned}\mu_{L^*} &= (\sum A(x, y)_{L^*}) / N \\ \mu_{u^*} &= (\sum A(x, y)_{u^*}) / N \\ \mu_{v^*} &= (\sum A(x, y)_{v^*}) / N\end{aligned}\quad (42)$$

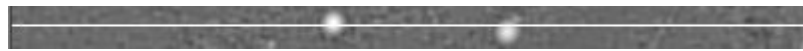
The difference between the two measured colors in the CIE color difference formula is given by

$$\Delta E_{uv}^* = ((\Delta L^*)^2 + (\Delta u^*)^2 + (\Delta v^*)^2)^{0.5} \quad (43)$$

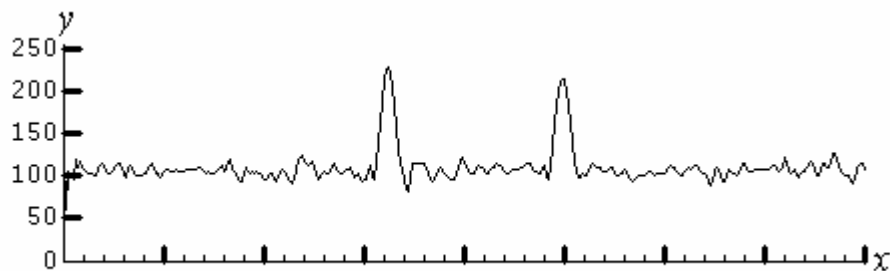
Given an image $f(x, y)_{L^*u^*v^*}$ and a standard color $(\mu_{L^*}, \mu_{u^*}, \mu_{v^*})$, we can use Eq. (43), to obtain a color difference map, $\Delta f(x, y)$. $\Delta f(x, y)$ is a gray scale image in which the differences between the $f(x, y)_{L^*u^*v^*}$ and $(\mu_{L^*}, \mu_{u^*}, \mu_{v^*})$ are shown.

2.4 Matched Filter for Spots Segmentation

We used the matched filters [46]-[49] to enhance the spots in the color difference map $\Delta f(x, y)$. As shown in Fig. 4-3, the shape of a spot in $\Delta f(x, y)$ is roughly a circle and its gray-level profile of the cross section follows the Gaussian distribution.



(a)



(b)

Fig. 4-3 (a) A portion of the color difference map. The white line denotes a cross section. (b) The gray-level profiles of the cross section in (a). The x -coordinate denotes the pixels along the cross section. The y -coordinate denotes the gray-level. .

Indeed, the intensity profile of a spot nearly follows a 2-D Gaussian intensity distribution [53] as shown in Eq. (44)

$$g_1(x, y) = e^{-(x^2+y^2)} = e^{-r^2}. \quad (44)$$

In Eq. (44), r is the radial distance measured from the center of a spot. If we define R as the radius at which the intensity drops to a half of its maximum value, we can rewrite the spot profile function as

$$g_1(x, y) = e^{-(r/R)^2 \ln(2)} = e^{\ln(2^{-r^2/R^2})}. \quad (45)$$

Eq. (45) can be simplified to obtain Eq. (46):

$$g_1(x, y) = 2^{-(x^2+y^2)/R^2}. \quad (46)$$

To obtain a zero mean filter, $g_1(x, y)$ is subtracted by m , the mean of the filter, as shown in Eq. (47),

$$g(x, y) = g_1(x, y) - m = 2^{-(x^2+y^2)/R^2} - m. \quad (47)$$

Because the radii of different spots vary, we employed a set of different sized matched filters. The radii of the spots range between 4 and 16 pixels. We therefore used pixel sizes 4, 8, 12 and 16 as the radii to design the kernels of the matched filers. Fig. 4-4 shows two of the four matched filter kernels. After applying the matched filters to $\Delta f(x, y)$, most of noise can be removed and the spots are enhanced.

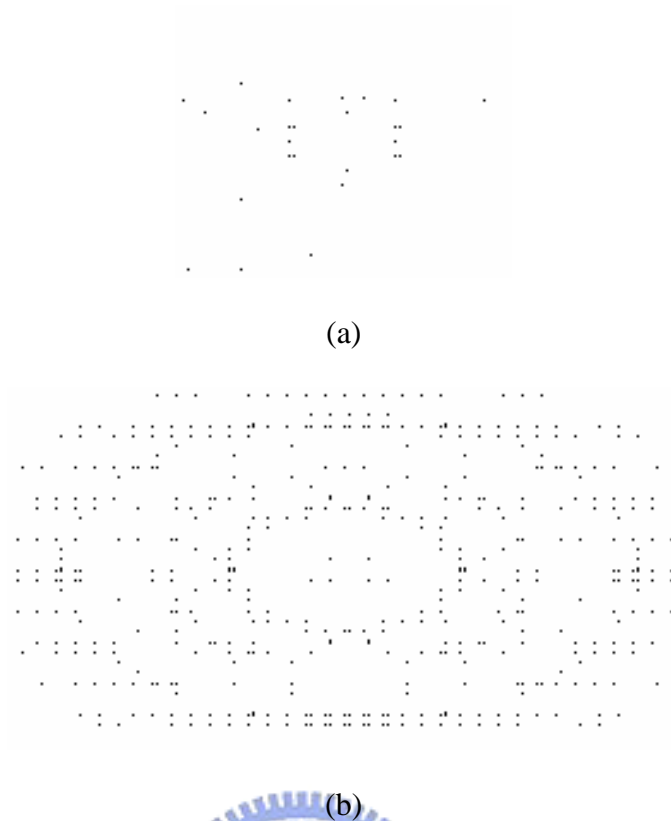
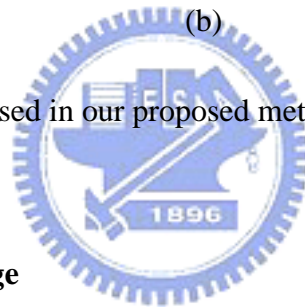


Fig. 4-4. 2-D matched filters used in our proposed method. The radius size is (a) 4, and (b) 8.



2.5 Compute the Binary Image

We set a threshold value for the resulting images. The threshold is determined either by the minimum error thresholding method [50] or by user intervening to decide a good threshold value. A binary image, in which the gray level for the pixels in the spots is depicted as 1 and the other pixels are depicted as 0, is obtained. The important statistical values are then derived from this binary image.

Before calculating the statistical values, we first compute the well regions. There are two reasons for computing the well regions. The first is that the area outside of the well is unwanted. Secondly, because we know that the well size is 7 mm, the pixel size can be derived from the segmented well region. Thus we are able to know the true sizes of the spots. We first convert the original image shown in Fig. 4-5 (a) into a gray-scale image and

apply the Sobel filter [52] to the gray-scale image. An edge map is obtained (Fig. 4-5 (b)). Applying the randomized algorithm for circle detection [51] on the edge map computes the well shown in Fig. 4-5 (c). The area outside the circle is removed to obtain the region inside the well, shown in Fig. 4-5 (d).

Finally, we segment the spots. Only the pixels in the well are considered. We compute the connected components formed by the pixels having value 1 after thresholding in the well. Each connected component is a spot. The size of a connected component is the size of the spot. The statistical values are then calculated.

3. A SOFTWARE TOOL

Based on the method stated above we implemented a software system that provides a friendly user interface for ELISA spot image analysis. A user can easily set experimental parameters such as the well diameter and the spot template. If the image intensity is too bright or too dark, the system provides window sliders to adjust the intensity and contrast. Because the colors of the spots vary between assays, the system provides a user interface method to establish the users' own customized parameters. Size-gated analysis (size filtering) enables a user to selectively count only the large spots. Other statistical analysis such as calculating the standard deviation and the mean are also provided. Fig. 4-6 shows a screenshot of our software system.

4. RESULTS

Several images were tested and the results obtained using the proposed method is presented in this section. The input images were color images in BMP format of size 1600

by 1200 pixels, shown in the first row in Fig. 4-7. The images in second row of Fig. 4-7 show the color difference maps. The results after applying the matched filtering are shown in the third row in Fig. 4-7. The binary images after intensity thresholding are shown in the fourth row in Fig. 4-7. The boundary points of the spots and the initial image are shown simultaneously in the fifth row in Fig. 4-7. The well diameters in Fig. 4-7 (a), (b), and (c) are 7.0 mm. The numbers of spots and other statistical values such as the mean, standard deviation, and coefficient of variance are shown in Table 4-1.

Table 4-1. The important statistical values.

	Well Diameter (mm)	Number of Spots	Mean (μm^2)	SD (μm^2)	CV
Fig. 4-7 (a)	7.0	62	0.1023	0.1262	1.2339
Fig. 4-7 (b)	7.0	70	0.1970	0.2120	1.0762
Fig. 4-7 (c)	7.0	66	0.1989	0.2624	1.3188

We evaluated the accuracy of the proposed computer method by comparing the number of spots identified by humans and the computer. Table 4-2 shows the results. A human could find more spots because humans can discern overlapping spots. The error rate was defined as the difference between the number of spots found over the spots identified by a human. The error rates were less than 3% in our experiment.

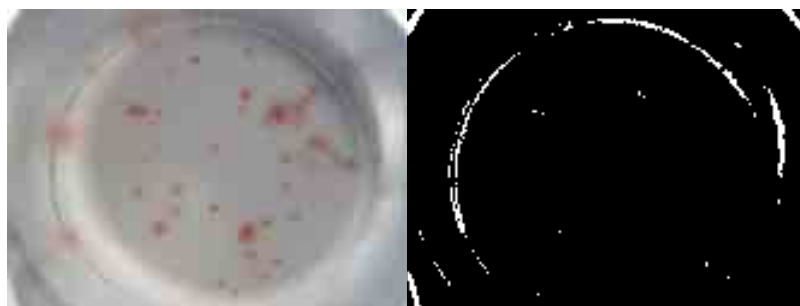
Table 4-2. Comparison of our inspection method and human.

	# of Spots by Our Method	# of Spots by Human	% of Error
Fig. 4-7 (a)	62	63	1.5 %
Fig. 4-7 (b)	70	71	1.4 %

The proposed methods were implemented on a PC with a Pentium 4(2.2 GHz) CPU running on Windows XP operating system. The overall execution time for a 1600×1200 pixels image took 5 seconds.

5. CONCLUSIONS

We presented a computer method for ELISA spot analysis in this chapter. The proposed method employs techniques such as color analysis and matched filtering to enhance the spots in the image. After preprocessing, intensity thresholding can effectively segment the spots. The experimental results showed that the error rate of the proposed method was less than 3%. This method can help immunologists to reduce time in analyzing the ELISA spot assay. Since the errors occur when there are overlapping spots, in order to improve the accuracy, to develop an intelligent method to separate the overlapping spots is our future work.



(a)

(b)

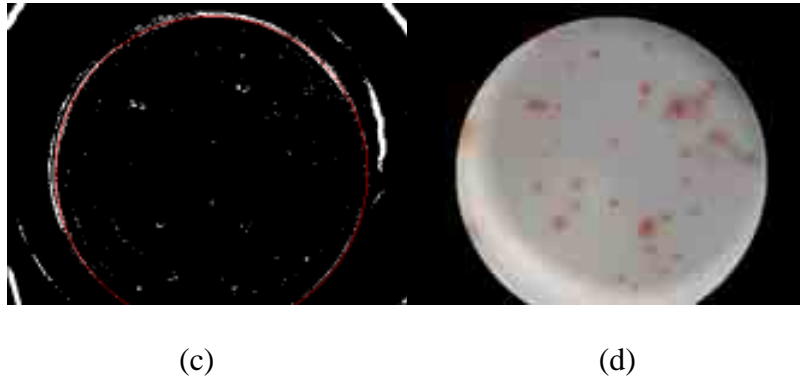


Fig. 4-5. (a) The original image. (b) Image after applying the Sobel filter. (c) After circle detection. (d) Remove the region outside the circle.

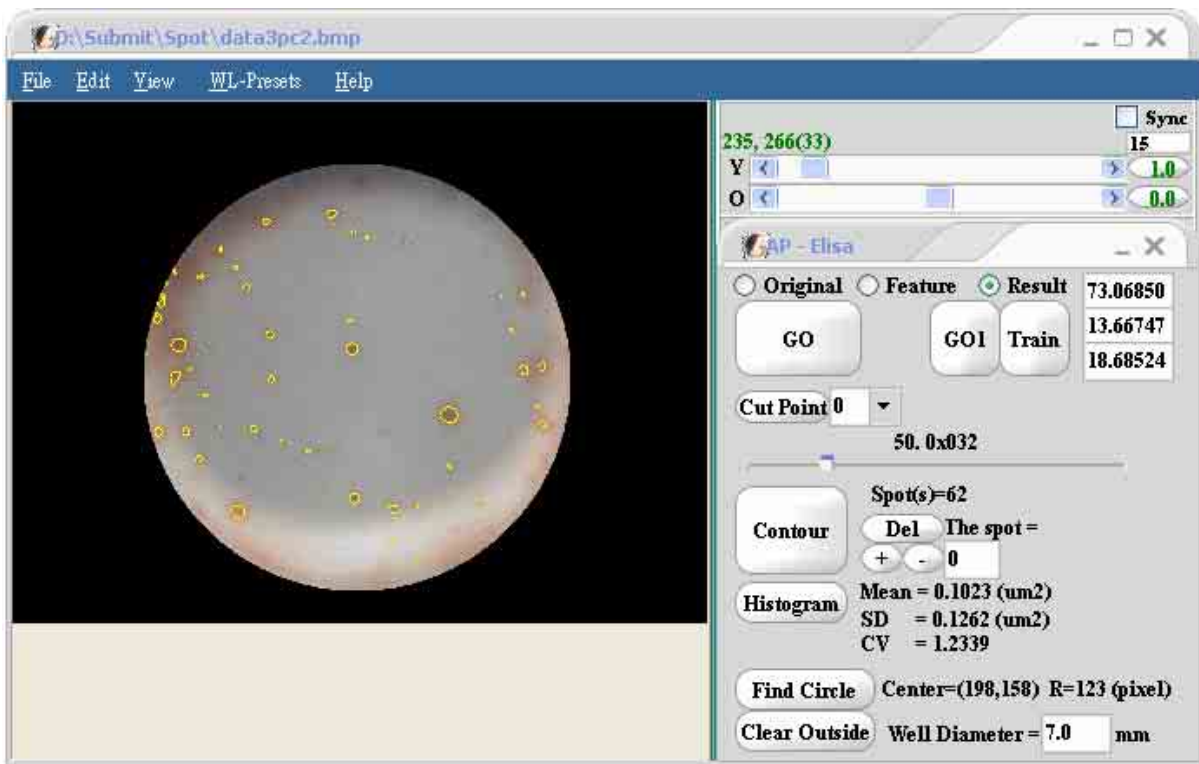
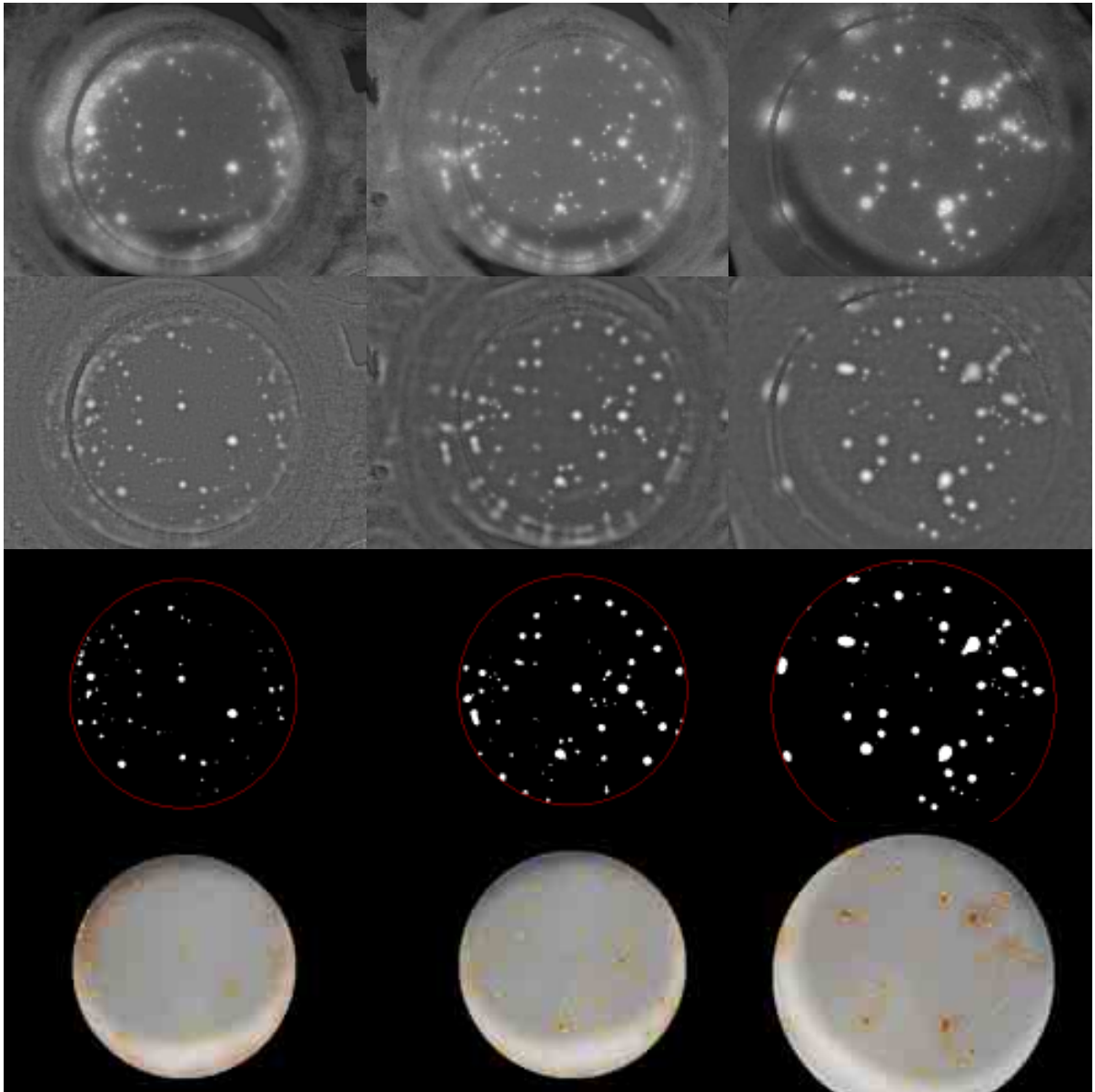


Fig. 4-6. A screenshot of the software system.





(a)

(b)

(c)

Fig. 4-7. First row, the three tested images from the proposed method. Second row, the color difference maps. In these images, the pixels with less difference are shown in the brighter intensity. Third row, the results after applying the matched filters. The 4th row, the final results. The last row, the original images overlying the results obtained in the images shown in 4th.

CHAPTER 5

Extraction of Coronary Arterial Tree Using Cine X-Ray Angiograms

An efficient and robust method for identification of coronary arteries and evaluation of the severity of the stenosis on the routine X-ray angiograms is proposed. It is a challenging process to accurately identify coronary artery due to poor signal-to-noise ratio, vessel overlap, and superimposition with various anatomical structures such as ribs, spine, or heart chambers. The proposed method consists of two major stages: (a) signal-based image segmentation and (b) vessel feature extraction. The 3D Fourier and 3D Wavelet transforms are first employed to reduce the background and noisy structures in the images. Afterwards, a set of matched filters was applied to enhance the coronary arteries in the images. At the end, clustering analysis, histogram technique, and size filtering were utilized to obtain a binary image that consists of the final segmented coronary arterial tree. To extract vessel features in terms of vessel centerline and diameter, a gradient vector-flow based snake algorithm is applied to determine the medial axis of a vessel followed by the calculations of vessel boundaries and width associated with the detected medial axis.

1. INTRODUCTION

Coronary angiography is still the most common modality for physicians to assess the severity of vessel narrowing or stenosis during percutaneous coronary intervention procedure. Accurate quantitative analysis of coronary arteries in digital angiographic images is valuable and important to clinical needs. Computer-assisted extraction of a set of major arteries or

the entire coronary arterial tree from two-dimensional (2-D) angiograms is regarded as a crucial process. Once the vessels are identified, additional techniques may be applied to obtain quantitative information including severity of stenosis, three-dimensional representation of the vascular tree, motion analysis of the coronary arteries, or blood-flow analysis [61-68].

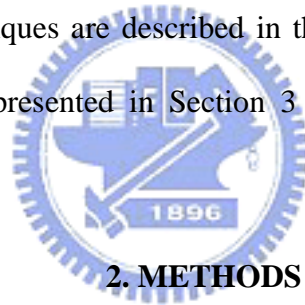
The major difficulty in automatic extraction of coronary arterial structures in angiogram lies in (1) low signal-to-noise ratio due to poor X-ray penetration, (2) vessel overlaps, and (3) superimposition of other tissues such as ribs, spine, or cardiac chambers. Traditional signal-based edge detection algorithms [69-75] were unable to effectively or accurately detect the desired structures. The existing methods specific to vessel extraction can be categorized into (i) model-based [76-78] (ii) tracking-based [79-81], (iii) classifier-based [82], and (iv) filter-based [83-85] techniques. In model-based methods, the coronary arterial tree is produced based on a pre-defined coronary artery model in the form of a “graph” structure. In tracking-based methods, the process proceeds with an initial start-of-search location followed by an automatic tracking process by exploiting the spatial continuity of the vessel's centerline, orientation, diameter, and density. In classifier-based methods, a clustering algorithm is employed with properly preprocessed data to differentiate vessel or non-vessel regions. In filter-based methods, the coronary arteries are enhanced and located so that they can be subsequently detected in the image.

The segmented vessel can then be used to facilitate quantitative coronary analysis such as the severity of stenosis in terms of length and diameter at the narrowing segment. The width can be obtained by calculating the boundary of the vessel. The other approach can be obtained by first calculating the medial axis of the artery then computing the width. Both approaches need to segment the coronary artery first.

In this chapter, a technique is proposed to first automatically segment the coronary arteries from cine angiogram followed by accurate extraction of vessel features. By use of the inherent nature of coronary cine angiography, the temporal information was incorporated to facilitate elimination of the background and noises. Such a preprocessing in conjunction with the matched filter can greatly improve the results. The proposed segmentation method consists of three major processes: (1) background and noise removal, (2) vessel enhancement, and (3) vessel identification.

The identified vessel structures are represented as a set of pixels in a binary image. The Gradient Vector Flow (GVF) Snake is then employed to calculate the medial axis of the vessel followed by determination of vessel diameters.

The details of proposed techniques are described in the next section. Experimental results and accuracy evaluation are presented in Section 3 to demonstrate the robustness of the proposed techniques.



2. METHODS

Let T denote the number of frames in the cine angiograms during the cardiac cycle, *i.e.*, the images acquired from end-diastole to end-systole and then back to end-diastole. Each image is defined by the function $f(x, y, t)$, where $t = 0, \dots, T-1$ with x and y denoting the two-dimensional (2-D) coordinates of a pixel in the given M by N image. The proposed method consists of several steps. Let $f_{i-1}(x, y, t)$ and $f_i(x, y, t)$ denote the respective input and output images for the intermediate process at the i -th step. The original raw image is defined by $f_0(x, y, t)$.

2.1 Background Removal

A temporal Fourier analysis is employed to eliminate the stationary background and slowly moving objects in the cine-angiographic images. The Fourier transformation of an image

sequence may result in a single peak at a frequency of 0, *i.e.*, a single direct current (DC) term, associated with stationary tissues [86]. Moreover, the band near the DC term corresponds to the slowly moving (due to respiration) objects in the image. The stationary or slowly moving objects are commonly ribs, spine, lung, or other internal structures appearing as background in the image, and can be eliminated by use of a temporal Fourier transformation. Given a sequence of T images $f_0(x, y, t)$, $0 \leq t \leq T-1$, the discrete Fourier transformation pairs are defined as

$$F_0(x, y, k) = \sum_{t=0}^{T-1} f_0(x, y, t) e^{-j2\pi kt/T} \quad 0 \leq k \leq T-1, \quad (48)$$

and

$$f_0(x, y, t) = \sum_{k=0}^{T-1} F_0(x, y, k) e^{j2\pi kt/T} \quad 0 \leq t \leq T-1. \quad (49)$$

The temporal Fourier transform defined in Eq. (48) is first applied to the image sequence followed by a high pass temporal filtering process $H(x, y, k) = (1 - e^{-\beta t})$ as follows

$$\bar{F}(x, y, k) = F_0(x, y, k)(1 - e^{-\beta t}), \quad 0 \leq k \leq T-1, t = \begin{cases} k & \text{when } k < \frac{T}{2} \\ T - k & \text{when } k \geq \frac{T}{2} \end{cases}, \quad (50)$$

where β is a given constant that controls the size of the background to be removed. The main effect of the high pass filter is to retrench the low-frequency terms. After the inverse Fourier transformation defined in Eq. (49) is employed, a new sequence of images $f_1(x, y, t)$, $0 \leq t \leq T-1$, is obtained in which the structures on the background (such as ribs and tissues) are suppressed. If the value of β is too large, only the stationary background will be removed. Therefore, an appropriate β is chosen to remove both the slowly moving structures as well as stationary background. An appropriate β is between 8 and 10.

2.2 Noise Removal

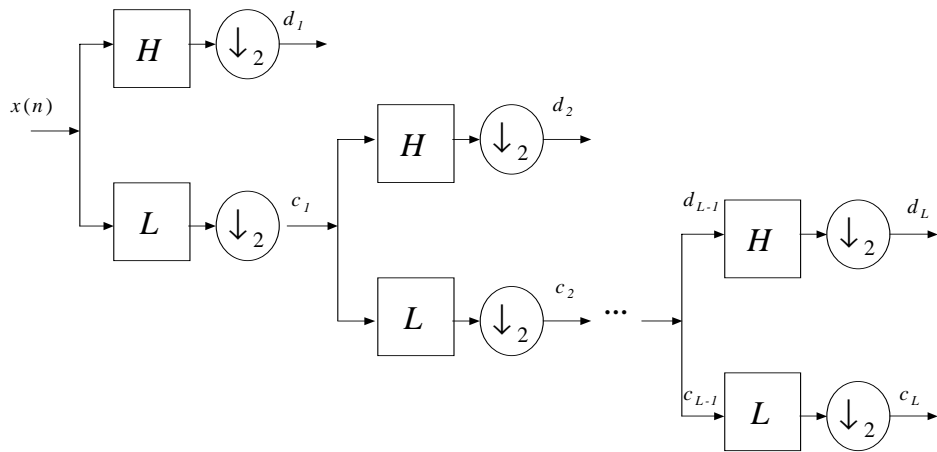
The resultant images after the previous processing may contain some spikes or noise. This is due to that the isolated noise cannot be detected and removed using the pure frequency domain based Fourier transforms. To overcome this problem, a “temporal” wavelet transformation is used. The definition of an ordinary Discrete Wavelet Transform (DWT) is summarized as follows and the details can be found in [87-89].

Let $L(\omega) = \sum_k l_k e^{-jk\omega}$ and $H(\omega) = \sum_k h_k e^{-jk\omega}$ denote the respective low-pass and high-pass

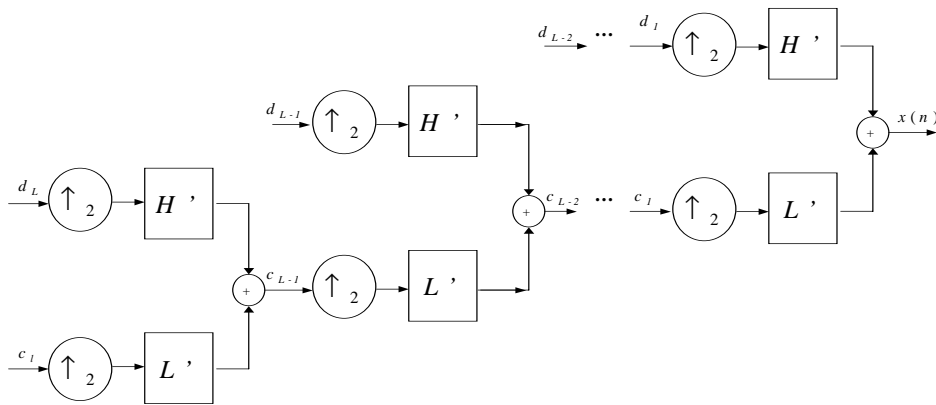
filters that satisfy the condition of orthogonality as shown in the following equation

$$|L(\omega)|^2 + |H(\omega)|^2 = 1. \quad (51)$$

The DWT employs the pair of orthogonal high-pass and a low-pass filter to decompose an input signal into the high frequency and low frequency components in different resolutions according to the number of levels employed. In the one-dimensional (1-D) case, a signal $x(n)$ is decomposed iteratively by applying the low-pass and the high-pass filters as shown in Fig. 5-1 (a). Let $x(n) = c_0$. $c_i, i=0, \dots, L-1$ is decomposed into a low frequency component c_{i+1} and a high frequency component d_{i+1} . Both c_{i+1} and d_{i+1} are down sampled by 2 from c_i . The coefficients $d_i, i=1, \dots, L$, are called the DWT wavelet coefficients of $x(n)$. The signal $x(n)$ can be reconstructed from its DWT coefficients as shown in Fig. 5-1 (b). The reconstruction process is the inverse discrete wavelet transform (IDWT).



(a)



(b)

Fig. 5-1. Multi-level wavelet (a) decomposition and (b) reconstruction for a 1-D case.

A two-dimensional discrete wavelet transform and its inverse are the extension of the one-dimensional transform. It is implemented by applying a one-dimensional DWT and IDWT along each of x and y coordinates. In other words, we apply a low-pass filter and a high-pass filter along each of the two coordinates. The original 2-D signal in the form of an image is then divided into four regions:

1. LL : obtained by applying two low-pass filters on both coordinates,

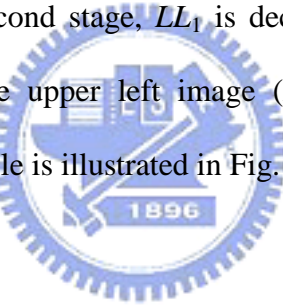
2. *HL* and *LH*: obtained by applying high-pass filters on one coordinate and a low-pass filter on the other coordinate, and

3. *HH*: obtained by applying two high-pass filters on both coordinates.

The *LL* component can be recursively decomposed by using the pair of low-pass and the high-pass filters to establish a *k*-stage discrete wavelet transform. A 3-stage discrete wavelet transformation is defined as

$$W(x, y, t) = DWT^3(f(x, y, t)), \quad 0 \leq t \leq T - 1. \quad (52)$$

The first stage of the transform is to decompose the image into four equal size sub-images corresponding to the upper left (*LL*₁), the upper right (*HL*₁), the lower left (*LH*₁), and the low right (*HH*₁) regions. In the second stage, *LL*₁ is decomposed into four sub-images again. For the subsequent stage *j*, the upper left image (*LL*_{*j*-1}) is further decomposed to four sub-images. The typical example is illustrated in Fig. 5-2.



<i>LL</i> ₃	<i>HL</i> ₃	<i>HL</i> ₂	<i>HL</i> ₁
<i>LH</i> ₃	<i>HH</i> ₃		
<i>LH</i> ₂		<i>HH</i> ₂	
<i>LH</i> ₁		<i>HH</i> ₁	

Fig. 5-2. A 2-D 3-stage discrete wavelet transformation.

In the proposed method, we applied a 3D 3-stage discrete wavelet transform (or a temporal wavelet transform). Orthogonal low-pass and a high-pass filters were applied along *x*, *y*, and *T* (*i.e.*, temporal) to decompose the original image into 8 components, *LLL*₁, *LHL*₁, *LLH*₁,

$LHH_1, HLL_1, HHL_1, HLH_1,$ and HHH_1 . Similar to that in the 2D case, the LLL component is recursively decomposed into 8 components as shown in Fig. 5-3.

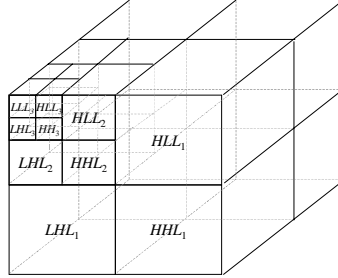


Fig. 5-3. A 3-D 3-stage discrete wavelet transformation.

Since noise commonly manifests as fine-grained structures in the image, the wavelet transform provides a scale-based decomposition by which the noisy signals can be represented by the finer scaled wavelet coefficients. In other words, LLL_3 is the region most unlikely containing noise. All the other 7 regions except LLL_1 in the first-stage wavelet transform likely contain noise. Because the coefficients at such scales may possibly denote the edge information, a threshold should be carefully selected to remove the noise while the edge information can be maintained. In the proposed method, each band except LLL_3 has its own threshold. The threshold, $0.5\sigma_1$, is selected based on the standard deviation σ_1 of the band. Finally, the inverse three-stage wavelet transform is applied to the image with the selected thresholds applied. The resultant images can be obtained using the following equation:

$$f_2(x, y, t) = IDWT^3(W(x, y, t)), 0 \leq t \leq T - 1. \quad (53)$$

By use of Eq. (53), the unwanted noise is removed but the local features of vessel structures are preserved.

2.3 Vessel Enhancement

Matched filters with multiple sizes and orientations are employed to identify and enhance the contexts or gray scales of coronary arteries. A matched filter is designed by assuming that the image background has constant intensity contaminated by white Gaussian noise [83]. The blood vessel can be regarded as a series of rectangular segments. By assuming the intensity profile of the arterial segments a Gaussian distribution, it can be written in the following equation:

$$g_1(x, y) = 1 - e^{-x^2/2\sigma^2}, \quad (54)$$

where σ^2 denotes the variance and σ is known as the standard deviation. Table 5-1 lists the values of a Gaussian distribution at several points.

Table 5-1. Values of the Gaussian Function

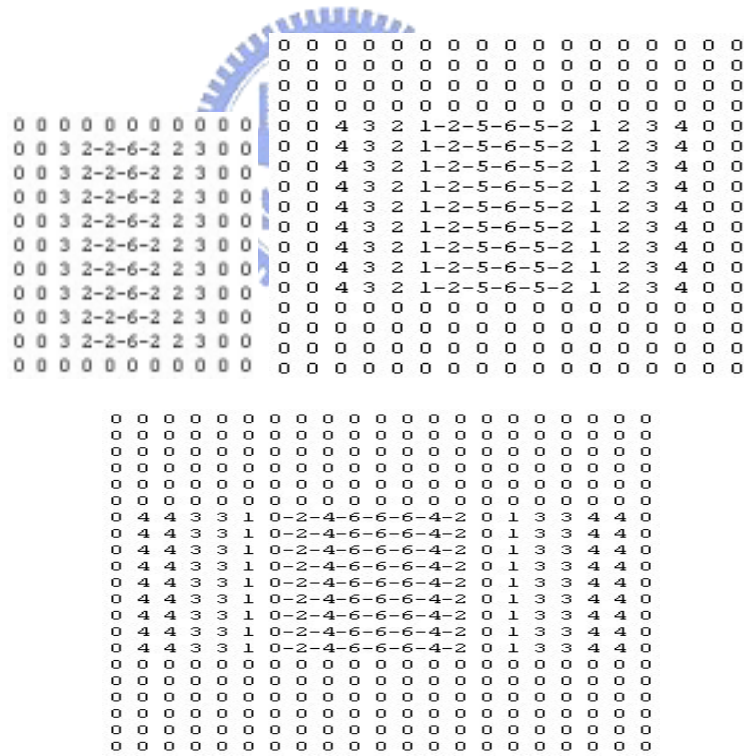
x	$e^{-x^2/2\sigma^2}$
0	1
0.5σ	0.8825
1.0σ	0.6065
1.5σ	0.3247
2.0σ	0.1353
3.0σ	0.0111

Since a Gaussian curve is infinite at the two ends, an appropriate range for the kernel designation is determined for computational efficiency. As shown in Table 5-1, when x is equal to 3.0σ , $e^{-x^2/2\sigma^2}$ is a small number (0.0111). The cutting threshold at 3σ was selected. Since the arteries have different width (ranging from 2 to 18 pixels in the image), kernel sizes ranging from 1σ to 6σ were chosen for the employed matched filers. In general, increasing the number of kernels yields better accuracy but more computational time

is required.

The proposed matched filter consists of two parameters, orientation θ and size σ . An angular resolution of 15° was used in the implementation. Six matched filters with various widths of σ in each orientation were employed. Fig. 5-4 shows a set of zero-degree matched filters with different values of σ . The matched filters in the other orientation are obtained by applying the transformation

$$R_\theta = \begin{bmatrix} \cos \theta & \sin \theta \\ -\sin \theta & \cos \theta \end{bmatrix}. \quad (55)$$



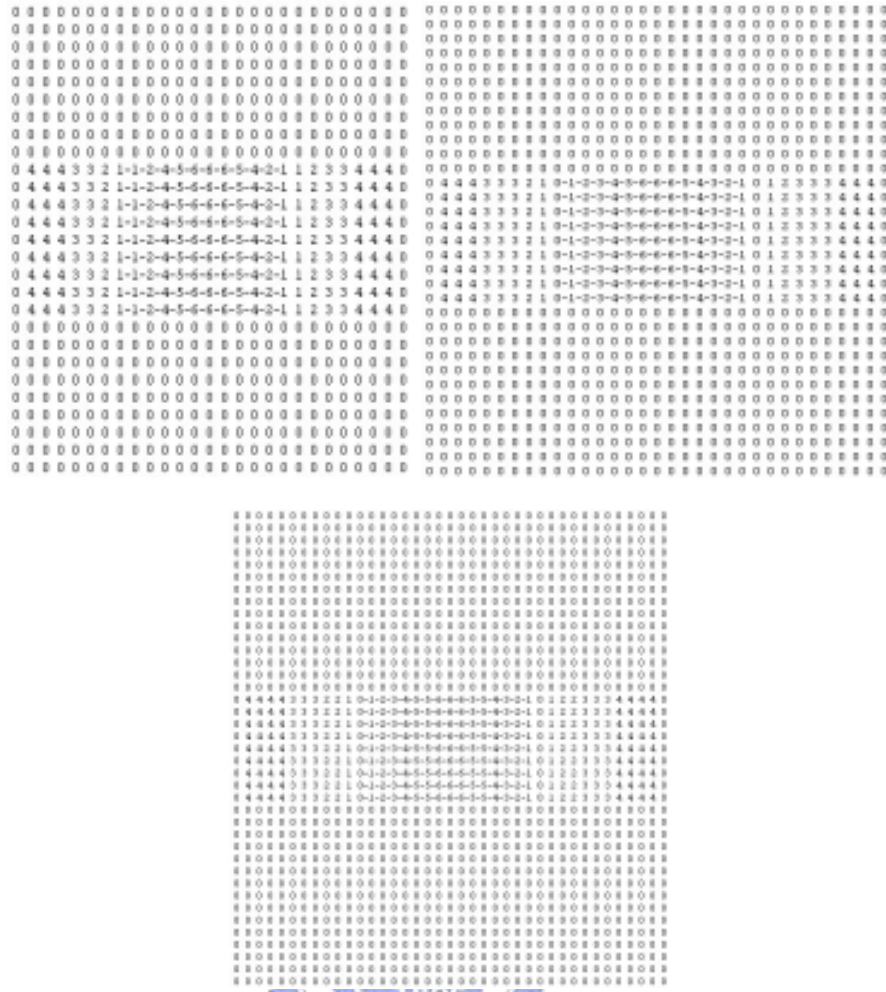


Fig. 5-4. Six matched filters ($\sigma = 1, 2, \dots, \text{and } 6$) with zero orientation.

On the basis of twelve orientations and six sizes, 72 filters were defined and employed. Given an image $f_2(x, y, t)$, the maximum response from the matched filters is retained for each orientation. Twelve images $f_2(x, y, \theta, t)$, $\theta = 0, 15, \dots, \text{and } 165^\circ$, are obtained to define a three-dimensional (3-D) space volume where the orientation is the third dimension. Let $f_{mo}(x, y, t)$ denote the projection of these 12 images onto the xy -plane. Both $f_2(x, y, \theta, t)$ and $f_{mo}(x, y, t)$ are utilized to identify the vessel in the next step.

2.4. Vessel Identification

The clustering analysis based on a stencil mask $S(x, y)$ and the vessel continuity properties are applied to further refine the results of segmentation. Note that $f_{mo}(x, y, t)$ is a gray scale image. Given a threshold value Δ , a binary image $B(x, y)$ is established according to Eq. (56).

$$B(x, y) = \begin{cases} 0 & \text{if } \max(f_{mo}(x, y, t)) < \Delta, \text{ for } t = 0, 1, \dots, T-1 \\ 1 & \text{otherwise} \end{cases} \quad \forall x, y, \quad (56)$$

The pixels of value 1 form connected components. The area occupied by the largest connected components in $B(x, y)$ forms the stencil mask, $S(x, y)$, as shown in Fig. 5-9. $S(x, y)$ is the area covered by the motion of coronary arterial structures. Therefore, those connected components formed by ribs, tissues, and noise can be removed based on the stencil mask as the following equations:

$$f_3(x, y, \theta, t) = \begin{cases} f_2(x, y, \theta, t), & \text{if } S(x, y) = 1, \\ 0 & \text{otherwise} \end{cases} \quad \forall x, y, \theta, t \quad (57)$$

Afterwards, a series of processes are applied to identify the vessels. They are detailed in the following.

1. A histogram analysis is applied to $f_3(x, y, \theta, t)$ for determination of a threshold value ξ , which is used to separate coronary arterial structures from the background in each orientation. Let $f_4(x, y, \theta, t)$ denote the image function after this process.
2. If the intensity of a pixel $p(x, y)$ is greater than a given threshold ξ in three consecutive images at orientation θ , that pixel is a part of the artery. Otherwise, its value is set to zero. The resultant image is denoted by $f_5(x, y, \theta, t)$.

3. Since arteries are structured connected in consecutive orientations, a 3-D 18-adjacency clustering analysis is applied to $f_5(x, y, \theta, t)$. A size filter is then applied to remove smaller connected components. A new image function $f_6(x, y, \theta, t)$ is obtained where the coronary arterial structures are maintained at each orientation.

The final segmentations of coronary arterial structures are obtained after projection of $f_6(x, y, \theta, t)$ onto the xyt -plane for all the orientations. The final segmentations of coronary arterial structure is denoted $f_7(x, y, t)$. Two segmented results are shown in Fig. 5-12.

2.5. Extraction of Vessel features

The final goal is to calculate the width of the vessel. We use $f_7(x, y, t)$ to determine the medial axis of the vessel first. We then calculate the width based on the medial axis. Snake method was first proposed in 1987 as an image segmentation algorithm [90]. A snake, S $v(s) = (x(s), y(s))$, is associated with a cost function E . E is written in the form

$$E = \int_0^1 E_{int}(v(s)) + E_{ext}(v(s)) ds, \quad (58)$$

where E_{int} represents the internal energy of the snake due to bending, and E_{ext} the external force that is derived from image features. E_{int} serves to impose smoothness constraint on the snake. E_{ext} pushes or pulls the snake toward desired features such as edges. Given an initial contour, the contour deforms under the control of the external and the internal forces. When the energy associated with the contour reaches the minimal, the contour is considered the best approximation of the boundary of the region of interest.

Xu and Prince proposed the Gradient Vector Flow (GVF) snake in 1998 [91]. In GVF snake, a vector field is created to serve as the external force. The GVF field is defined to be a vector field $p(x,y) = [g(x,y),h(x,y)]$ that minimize the energy

$$\xi = \iint \mu(g_x^2 + g_y^2 + h_x^2 + h_y^2) + |\nabla f|^2 |p - \nabla f|^2 dx dy. \quad (59)$$

Using calculus of variations [91], it can be shown that the GVF field can be found by solving the following Euler equations:

$$\mu \nabla^2 g - (g - f_x)(f_x^2 + f_y^2) = 0, \text{ and}$$

$$\mu \nabla^2 h - (h - f_y)(f_x^2 + f_y^2) = 0, \quad (60)$$

where ∇^2 is the Laplacian operator.

Using GVF to server as external forces, we can move the snake to minimize the energy of the contour shown in Eq. (58). The solution can be solved by using the greedy approach [92] or the finite difference method [90].

The GVF field is generally obtained from an edge map. An important property of the vector flow is that a vector close to an edge points to the center of the edge. The proposed medial axis finding algorithm is based on this property.

The resulted arterial tree in $f_7(x, y, t)$ is a binary image. The vectors in the GVF field created from $f_7(x, y, t)$ point to the medial axis of the vessel. Given a polygonal path with two end points on the medial axis of a vessel (the initial snake), the vector flow pushes the polygonal path toward the center of the vessel. When the snake converge to it minimum cost, we have the medial axis of the vessel.

Given the medial axis $\langle p_1, p_2, \dots, p_m \rangle$, let $\overline{q_i, q_i}$ be a line segment passing through p_i and

perpendicular to the polygonal path $\langle p_1, p_2, \dots, p_m \rangle$. The two end points q_{l_i} and q_{r_i} are respectively to the left and right of the polygonal path from p_1 to p_m . The polygonal paths $\langle q_{l_1}, p_{2_1}, \dots, p_{m_1} \rangle$ and $\langle q_{r_1}, p_{2_r}, \dots, p_{m_r} \rangle$ are approximations of the left and right boundaries of the vessel obtained from $f_7(x, y, t)$. The accuracy of these boundaries can be further improved by applying the GVF snake method again. The edge map is obtained by applying the canny edge operator followed by intensity thresholding. The polygonal path $\langle q_{l_1}, p_{2_1}, \dots, p_{m_1} \rangle$ and $\langle q_{r_1}, p_{2_r}, \dots, p_{m_r} \rangle$ serve as the initial snakes. The resulted boundaries accurately present the true boundaries. The width of the vessel diameter is the distance along normal direction from centerline point to $\langle q_{l_1}, p_{2_1}, \dots, p_{m_1} \rangle$ plus centerline point to $\langle q_{r_1}, p_{2_r}, \dots, p_{m_r} \rangle$

3. RESULTS

Two cases are studied to demonstrate the results obtained using the proposed technique. Fig. 5-5 (a) and (b) show the cine angiograms of a left coronary artery (LCA) tree and a right coronary artery (RCA) tree. Each sequence of X-ray angiograms consists of 30 images from end-diastole through end-systole then back to end-diastole. Each image has the size of 512 \times 512 pixels with 8-bit gray scales per pixel. Fig. 5-6 shows one exemplar frame of the entire sequence in Fig. 5-5 (a). Fig. 5-7 shows the result after background removal. The results after applying the DWT de-noise process and applying the 72 matched filters are shown in Fig. 5-8. The results after the stencil masking process are shown in Fig. 5-9 where only one connected component exists. Fig. 5-10 shows the result of the projection onto the xyt -plane along θ -axis. The final segmentation of moving coronary arterial structures is shown in Fig. 5-11. In Fig. 5-13, we superimpose the boundaries of the results shown in Fig. 5-12 to

the original images. As shown in Fig. 5-13, almost the whole arterial structures are extracted.

The magnitude of the vector field created from Fig. 5-12 (b) is shown in Fig. 5-14. The initial snake is provided by a user interface method. As shown in Fig. 5-15, the initial snake is given for finding the media axis of the vessel. Fig. 5-16 shows the media axis found by the GVF snake. We also provide a user interface method to trace the pixels on the media axis. The system computes the diameter of vessel in pixel where mouse select. Fig. 5-16 shows the diameters for some selected points on the medial axis.

4. CONCLUSION

In this chapter, we present an efficient and robust method for segmentation of coronary arteries from the cine angiogram in conjunction with GVF snake based method to extract the width of the artery in the angiographic image. The signal-based segmentation algorithm provides the initial results of identified coronary arterial tree. The details of vessel features (e.g., lesion length and vessel narrowing) can be accurately calculated by the GVF snake method to facilitate coronary quantitative analysis.

The proposed methods were implemented on a PC with a Pentium 4 (2.2 GHz) CPU running on Windows XP operating system. The overall execution time for a sequence of 30 512×512 pixels images took less than 3 minutes..

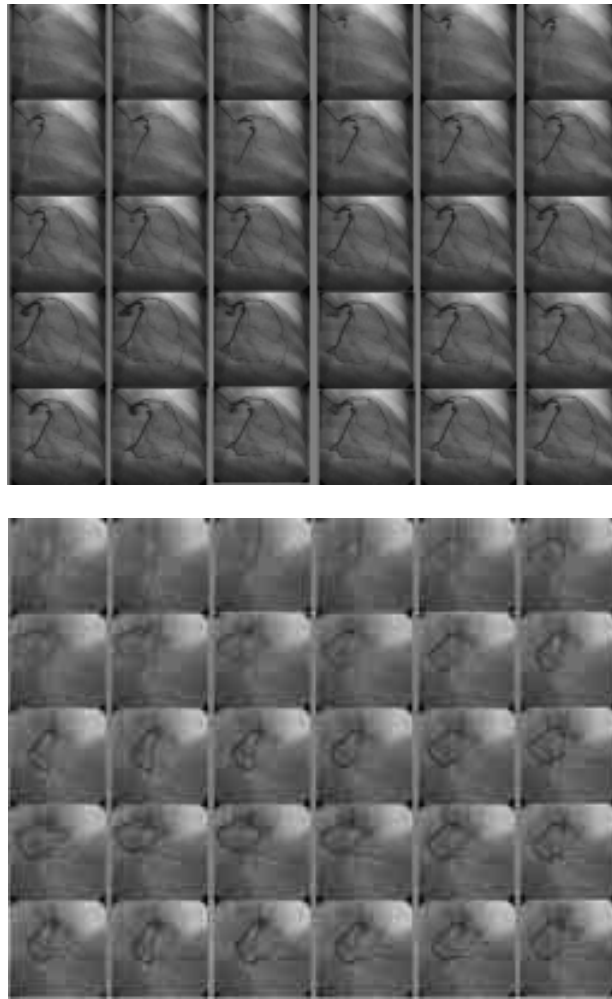


Fig. 5-5. (a) The cine angiograms of a left coronary artery (LCA). (b) The cine angiograms of a right coronary artery (RCA).

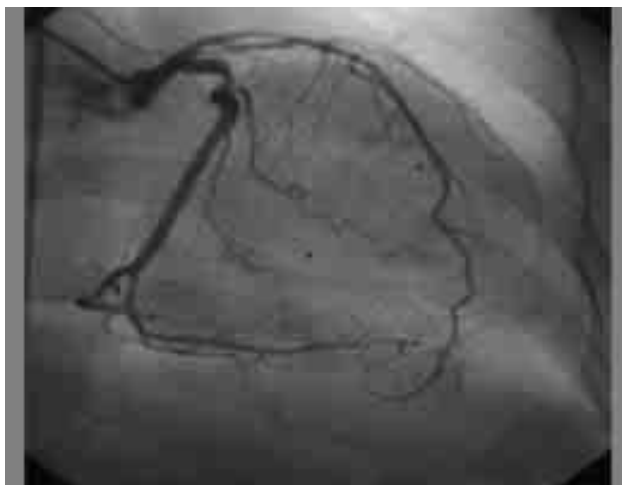


Fig. 5-6. The typical example of one frame in the cine angiograms of Fig. 5-5 (a).



Fig. 5-7. One of the resultant images after the background removal process.

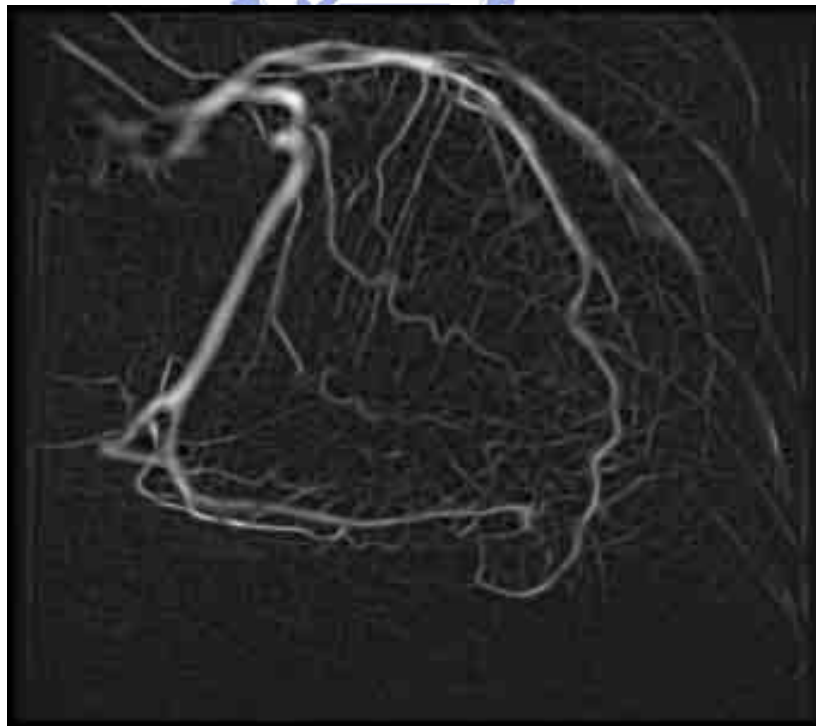


Fig. 5-8. The resultant image after applying the DWT de-noise process and applying the matched filter.



Fig. 5-9. The resultant binary image after the 2-D stencil masking process where the black pixel is denoted by zero and the white pixel is denoted by 1.

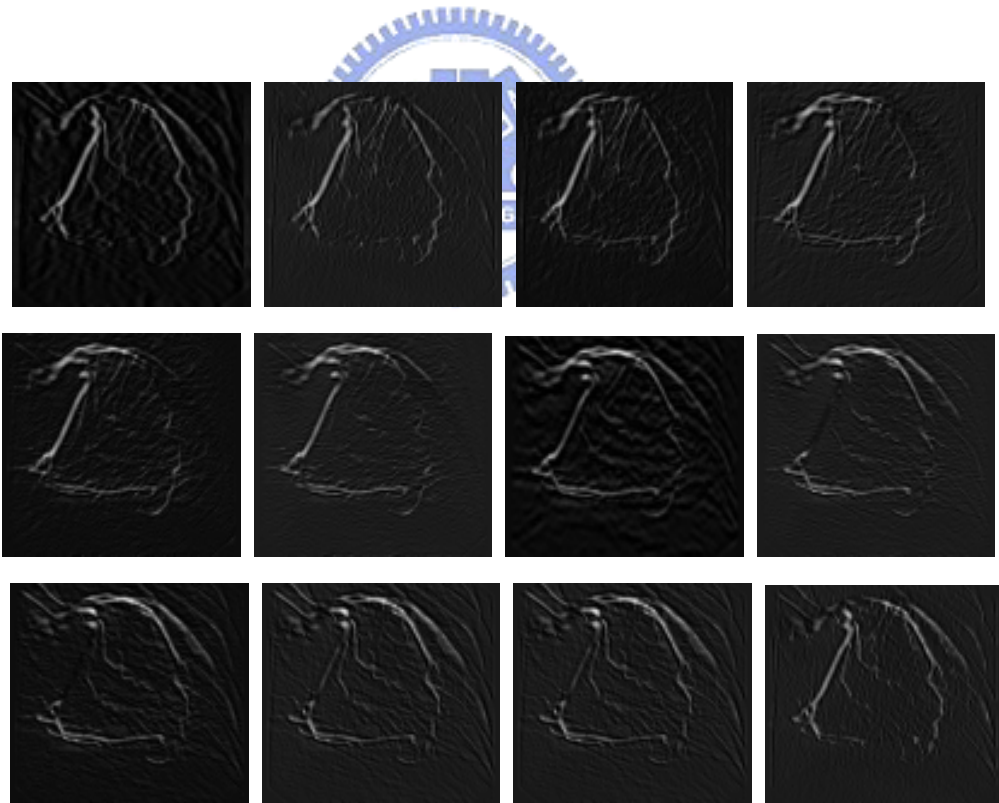
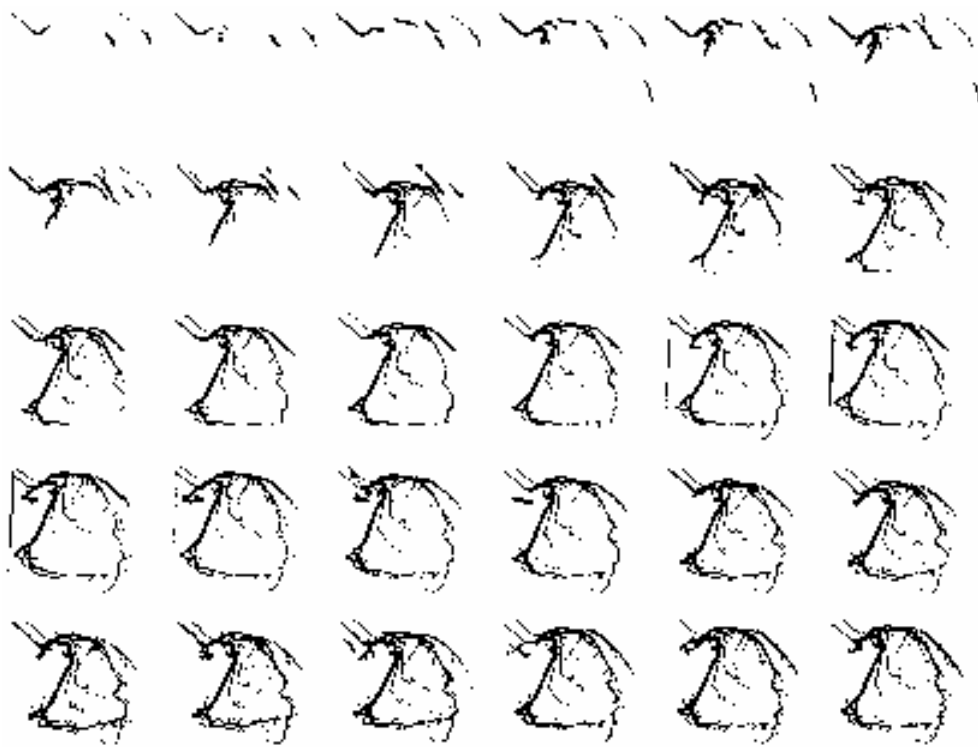
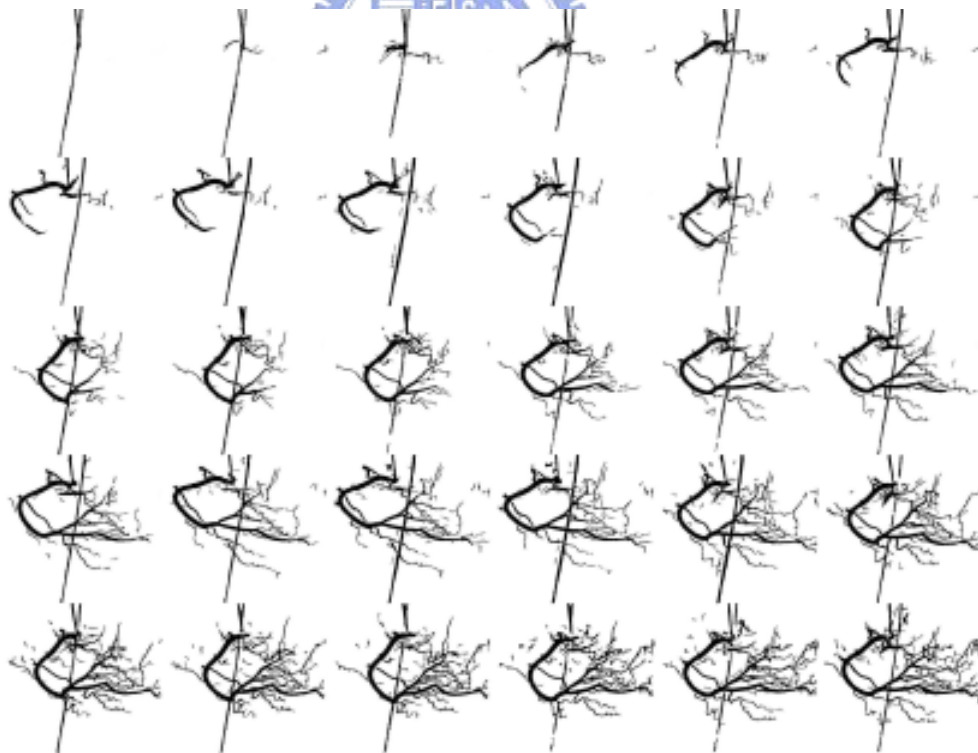


Fig. 5-10. The projection onto xy -plane along θ -axis



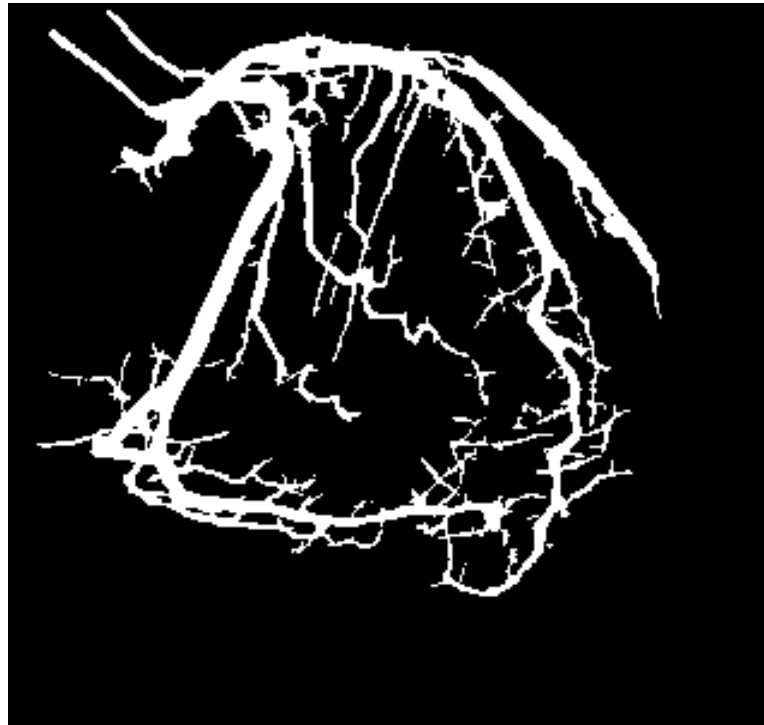
(a) LCA



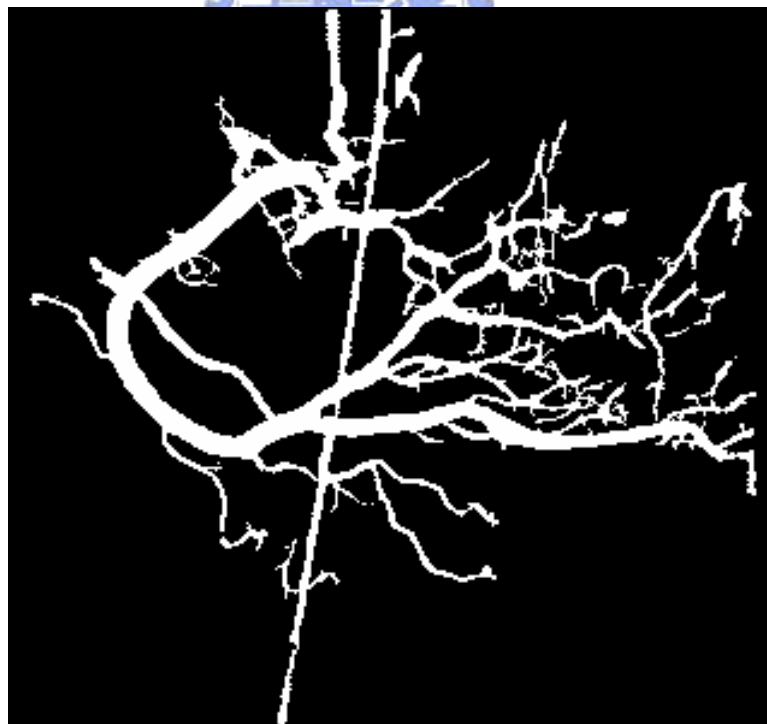
(b) RCA

Fig. 5-11. The final segmentation results on a sequence of X-ray angiographic images on Fig.

5-5.

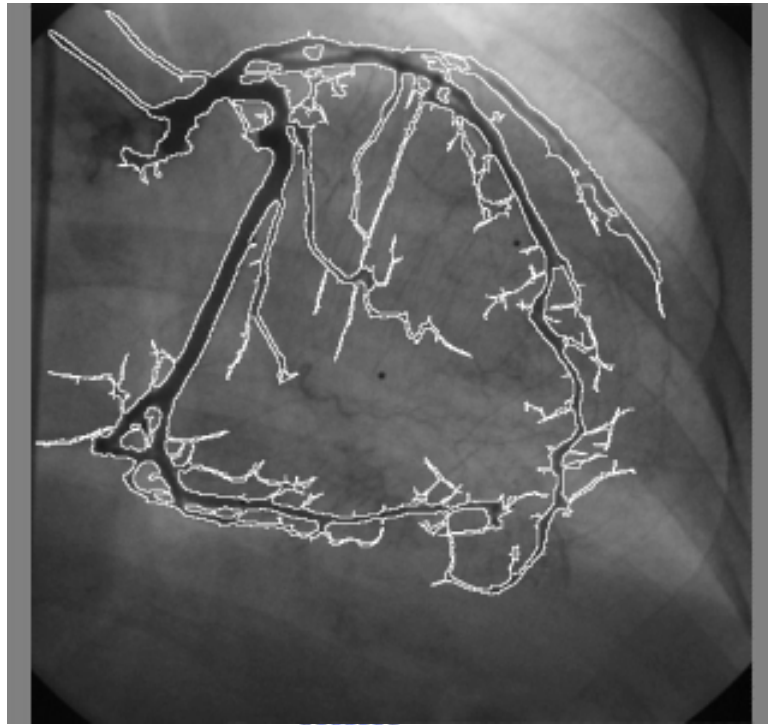


(a)



(b)

Fig. 5-12. Two segmented results. (a) The last image in Fig. 5-11 (a). (b) The last image in Fig. 5-11 (b).



(a)



(b)

Fig. 5-13. The original images are overlaying the results obtained in Fig. 5-12.

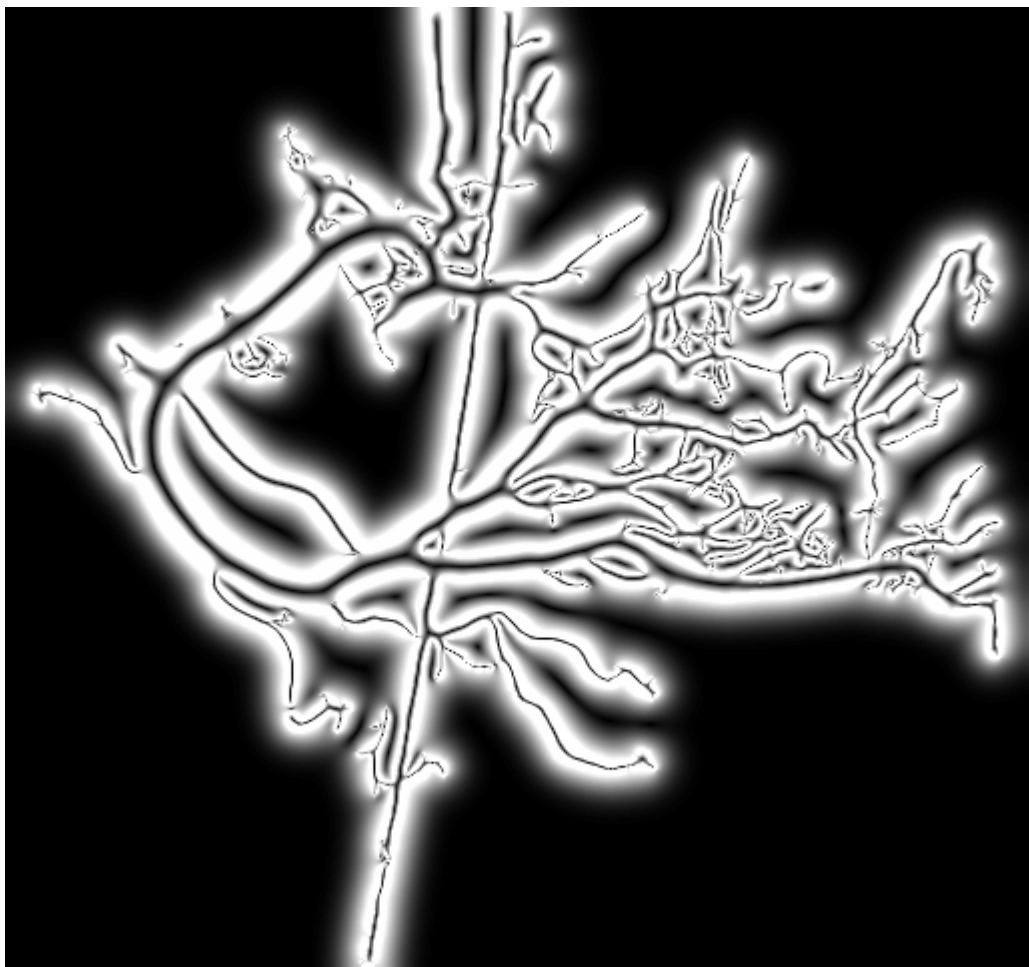


Fig. 5-14. The magnitude of GVF in Fig. 5-12 (b)

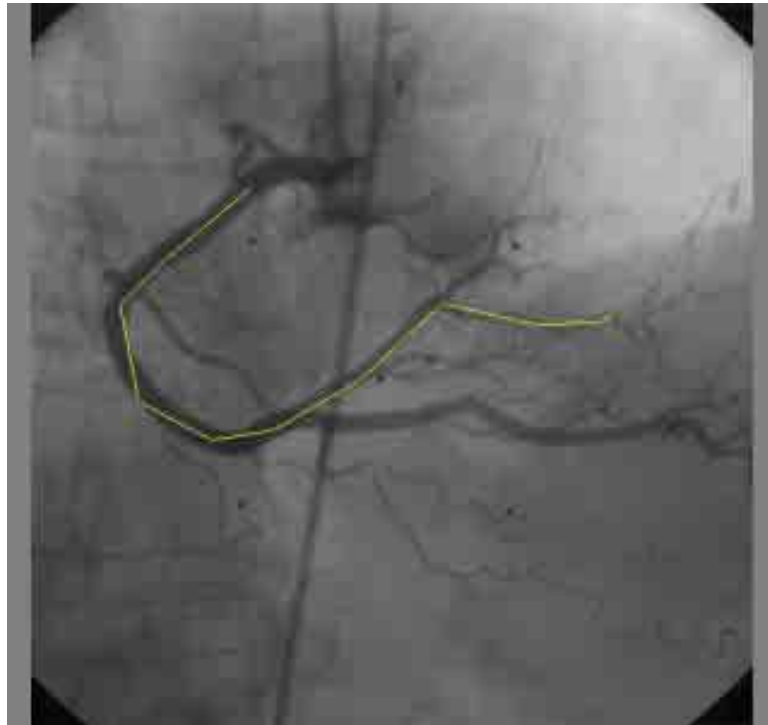


Fig. 5-15. Initial snake for finding the medial axis of vessel.

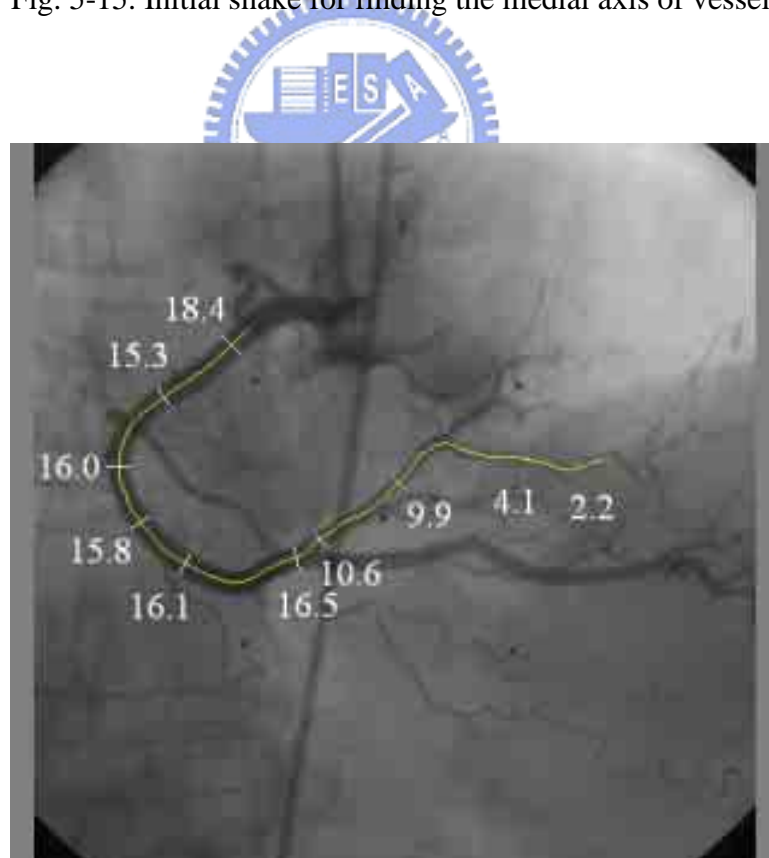


Fig. 5-16. The result of the centerline of vessel with widths for some selected points on the medial axis marked.

APPENDIX

1. Grid Artifacts Removal Using Bucky

To explain a Bucky can reduce the grid artifacts, considering a similar phenomenon, photograph degradation [54]-[60] caused by the relative motion between the camera and the scene. There are a moving scene (the grid) and a fixed camera. The grid image after degradation, denoted $g(x,y)$, can be modeled using Eq. (61)

$$g(x, y) = \iint h(x - x', y - y') I_p(x', y') dx' dy', \quad (61)$$

where $h(x,y)$ denotes the system response of the motion degradation.

Fourier transforming both sides of Eq. (61), we obtain

$$G(u, v) = H(u, v) \tilde{I}_p(u, v). \quad (62)$$

The total exposure at any point in the imaging plate can be obtained by integrating the instantaneous exposures over the time interval. If $\alpha(t)$ and $\beta(t)$ are the displacement along the x and y directions, respectively, we have

$$g(x, y) = \int_{-T/2}^{T/2} I_p(x - \alpha(t), y - \beta(t)) dt, \quad (63)$$

where T is the duration of the exposure.

Fourier transforming both sides of Eq. (63), we obtain

$$G(u, v) = \iint \int_{-T/2}^{T/2} I_p(x - \alpha(t), y - \beta(t)) e^{-j2\pi(u\alpha(t) + v\beta(t))} dt dx dy. \quad (64)$$

Replacing the variables $x - \alpha(t)$ with ξ and $y - \beta(t)$ by η , Eq. (64) becomes

$$\begin{aligned} G(u, v) &= \iint \int_{-T/2}^{T/2} I_p(\xi, \eta) e^{-j2\pi(u\xi + v\eta)} e^{-j2\pi(u\alpha(t) + v\beta(t))} dt d\xi d\eta \\ &= \tilde{I}_p(u, v) \int_{-T/2}^{T/2} e^{-j2\pi(u\alpha(t) + v\beta(t))} dt. \end{aligned} \quad (65)$$

According to Eq. (62) and (65), the transfer function $H(u,v)$ of this moving degradation is given by

$$H(u, v) = \int_{-T/2}^{T/2} e^{-j2\pi(u\alpha(t)+v\beta(t))} dt. \quad (66)$$

Suppose that the motion is uniform in the x -direction with velocity V , then

$$\alpha(t) = Vt, \quad \beta(t) = 0. \quad (67)$$

Substituting Eq. (67) into Eq. (66), we obtain

$$H(u, v) = \frac{\sin \pi u VT}{\pi u V} = T \text{sinc}(uVT). \quad (68)$$

The PSF, $h(x, y)$, is obtained by inverse Fourier transforming Eq. (68) into Eq. (69)

$$h(x, y) = \frac{1}{V^2 T} \cdot \text{rect}(x/VT), \quad (69)$$

where $\text{rect}(x)$ is given as

$$\text{rect}(x/VT) = \begin{cases} 1 & \text{for } |x/VT| \leq \frac{1}{2} \\ 0 & \text{otherwise} \end{cases}. \quad (70)$$

Eq. (69) is actually a mean filter that has the effect of smoothing the grid artifacts. The size of the mean filter kernel depends on $\text{rect}(x/VT)$, i.e., for large exposure time (T) or fast Bucky movement speed (V) we obtain a large kernel. If

$$VT \geq T_g, \quad (71)$$

the size of the kernel covers all T_g , the grid artifacts of T_g is blurred out completely.

REFERENCES

- [1] L. J. Cesar, B. A. Schueler, F. E. Zink, T. R. Daly, J. P. Taubel, and L. L. Jorgenson, "Artifacts found in computed radiography," *The British Journal of Radiology*, pp. 195-202, 2001.
- [2] Jun Wang, and H.K. Huang, "Film Digitization Aliasing Artifacts Caused by Grid Line Patterns," *IEEE Trans. Med. Imaging*, pp. 375-385, 1994.
- [3] L. L. Barski and X. Wang, "Characterization, detection and suppression of stationary grids in digital projection radiography imagery," *Proceedings of SPIE*, pp. 502-519, 1999.
- [4] I. N. Belykh and C.W. Cornelius, "Antiscatter stationary grid artifacts automated detection and removal in projection radiography images," *Proceedings of SPIE*, pp. 1162-1166, 2001.
- [5] R. Sasada, M. Yamada, S. Hara, H. Takeo, "Stationary grid pattern removal using 2-dimensional technique for Moire-free radiographic image display," *Proceedings of SPIE*, 2003.
- [6] Kenneth R. Castlenman, "Digital Image Process," Prentice Hall International Editions, p. 41, 1996.
- [7] Editor: J. Beutel, H. L. Kundel, and R. L. V. Metter, "Handbook of Medical Imaging: Physics and Psychophysics," *SPIE Press*, 2000.
- [8] J. T. Bushberg, "The essential physics of medical imaging," 2nd Edition, 2002.
- [9] J. A. Rowlands, "The physics of computed radiography," *Physics in Medicine and Biology*, pp. 123-166, 2002.

- [10] M. Ganten, B. Radeleff, A. Kampschulte, M. D. Daniels, G. W. Kauffmann, and J. Hansmann, "Comparing Image Quality of Flat-Panel Chest Radiography with Storage Phosphor Radiography and Film-Screen Radiography," *American Roentgen Ray Society*, pp. 171-176, 2003.
- [11] C. Chaefer-Prokop, M. Uffmann, E. Eisenhuber, and M. Prokop, "Digital Radiography of the Chest: Detector Performance Parameters," *Journal of Thoracic Imaging*, pp. 124-137, 2003.
- [12] G. Harrell, Chotas, T. James, Dobbins, E. Carl, and Ravin, "Principles of Digital Radiography with Large-Area, Electronically Readable Detectors: A Review of the Basics," *Review of Principles of Digital Radiography*, pp. 595-599, 1999.
- [13] J. A. Cadzow and H. F. Van Landingham, "Signals, Systems, and Transform," *Prentice-Hall*, Englewood Cliffs, New York, 1974.
- [14] D. A. Linden, "A Discussion of Sampling Theorems," *Proc. IRE*, pp. 1219-1226, 1959.
- [15] J. W. Goodman, "Introduction to Fourier Optics," *McGraw-Hill*, New York, 1968.
- [16] O. Kafri and I. Glatt, "Topography and Spinal Deformity," *Wiley*, New York, 1990.
- [17] M. Lia, D. Wilsona, M. Wonga, A. Xthona, "The evolution of display technologies in PACS applications," *Computerized Medical Imaging and Graphics*, pp. 175-184, 2003.
- [18] "CR & PACS: Insights & Images-Grids for Computed Radiography," *The User's Publication of Computed Radiography*, fall 2000.
- [19] F. Detrick, "PACS Planning Guide," *Air Force Medical Logistics Office / FOE, Technology Integration and Support Team*, pp. 7-8, 2001.
- [20] "DICOM Standard: Digital Imaging and Communications in Medicine (DICOM) Part 3: Information Object Definitions," *National Electrical Manufacturers Association*, 2004.
- [21] "Fujifilm Standard: DICOM Comformance Statement Fuji Computed Radiography QA-WS771," *Fuji Photo Film Co. Ltd*, Japan, 2001.

- [22] "AGFA: Healthcare DICOM Conformance Statement: ADC-QS Version 2.1," *HealthCare Glasgow Business Community*, Sep., 2002.
- [23] S. C. Bushong, "Physics, Biology, and Protection," *Radiologic Science for Technologists*," 7th Edition, 2001.
- [24] J. Sambrook and D. W. Russell, "Molecular cloning: A laboratory manual. Third Edition," *Cold Spring Harbor Laboratory Press. Cold Spring Harbor, New York.*, 2001.
- [25] W. Z. Cheng, K. S. Yen, C. Y. Lin, Y. T. Ching, Y. L. Yang, "Comparing lanes in the pulsed-field gel electrophoresis (PFGE) images," *23rd annual international conference of the IEEE engineering in medicine and biology society*, 2001
- [26] R. A. J. V. Daelen, and P. Zabel, "Preparation of high molecular weight plant DNA and analysis by pulsed-field gel electrophoresis," In *Plant Molecular Biology Manual* (S.B. Gelvin, R.A. Schilperoort, and D.P.S. Verma, eds.), pp. A15/1-25. Kluwer Academic Publishers, the Netherlands, 1991
- [27] B. Birren, L. Hood, and E. Lai, "Pulsed field gel electrophoresis: Studies of DNA migration made with the programmable, autonomously-controlled electrode electrophoresis system." *Electrophoresis* 10, pp. 302-309, 1989.
- [28] C. A. Glasbey, "An analysis of histogram-based thresholding algorithms," *CVGIP-Graphical Models and Image Processing*, pp. 532-537, 1993.
- [29] L. A. Wainstein and V.D., Zubakov, "Extraction of Signals from Noise, and D. Hildereth, " *Prentice-Hall, Englewood Cliffs, NJ*, 1962.
- [30] G. L. Turin, "An Introduction to Matched Filter," *IRE Transactions in Information Theory*, June 1960.
- [31] D. Middleton, "On New Classes of Matched Filters and Generalizations of the matched filter concept," *IRE Transactions on Information Theory*, pp. 349-360, June 1960

- [32] G. Lohmann, "Volumetric Image Analysis," *Wiley & Sons Ltd.*, 1998.
- [33] J. B. T. M. Roerdink and A. Meijster, "The watershed transform: Definitions, Algorithms and Parallelization Strategies," *Fundamenta Informaticae*, Institute for Mathematics and Computing Science University of Groningen, pp. 187-228, 2000.
- [34] L. Vincent and P. Soille, "Watersheds in Digital Space: An Efficient Algorithm Based on Immersion Simulations," *IEEE Trans. PAMI*, Vol. 13, pp. 583-598, Jun. 1991.
- [35] T. Corman, C. Leiserson, R. Rivest, "Introduction to Algorithms, 2nd edition," *MIT Press*, 2001
- [36] K. Fujihashi, J. R. McGhee, K. W. Beagley, D. T. McPherson, S. A. McPherson, C-M, Huang, and H. Kiyono, "Cytokine-specific ELISPOT assay. Single cell analysis of IL-2, IL-4 and IL-6 producing cells." *J. Immunol. Methods*, Vol. 160, 1993, pp. 181-189.
- [37] K. Murali-Krishna, J. D. Altman, M. Suresh, D. J. D. Sourdive, A. J. Zajac, J. D. Miller, J. Slansky, and R. Ahmed, "Counting antigen-specific CD8 T cells: a reevaluation of bystander activation during viral infection." *Immunity*, Vol. 8, 1998, pp. 177-187.
- [38] A. Y. Karulin, M. D. Hesse, M. Tary-Lehmann, and P. V. Lehmann, "Single-cytokine-producing CD4 memory cells predominate in type 1 and type 2 immunity," *J. Immunol*, Vol. 164, 2000, pp. 1862-1872.
- [39] Z. Yu and C. Bajaj, "Detecting circular and rectangular particles based on geometric feature detection in electron micrographs," *Journal of Structural Biology*, Vol 145, 2004, pp. 168-180.
- [40] L. V. Guimaraes, A. A. Suzim and J. Maeda, "A New Automatic Circular Decomposition Algorithm Applied to Blood Cells Image," *1st IEEE International Symposium on Bioinformatics and Biomedical Engineering*, 2000, pp. 277-280.

- [41] Y. Zhu, "Automatic Particle Detection through Efficient Hough Transforms," *IEEE Transactions on Medical Image*, Vol. 22, No.9, Sep. 2003, pp. 1053-1062.
- [42] Z. Yu and C. Bajaj, "A Clustering-Based Method for Particle Detection in Electron Micrographs," *Fifth International Conference on Advances in Pattern Recognition*, Dec., 2003, pp. 10-13.
- [43] P. Bosdogianni, "Image Processing-Fundamentals," *John Wiley & Sons Ltd*, 1999, pp.149-151.
- [44] "Commission Internationale de l'Eclairage Colorimetry," *2nd edn, CIE publication 15.2*. Paris: CIE, 1986.
- [45] G. Wyszecki, W.S. Stiles, "Color Science: Concepts and Methods," *Quantitative Data and Formulae*, Second Ed. New York: Wiley, 1982
- [46] S. Haykin, "Communication Systems," *New Delhi: Wiley Eastern*, 1979.
- [47] D. H. Friedman, "Detection of Signals by Template Matching," Baltimore, MD., Johns Hopkins University Press, 1969.
- [48] G. L. Turin, "An Introduction to Matched Filter," *IRE Transactions on Information Theory*, June 1960.
- [49] D. Middleton, "On New Classes of Matched Filters and Generalizations of the matched filter concept," *IRE Transactions on Information Theory*, Jun. 1960, pp. 349-360
- [50] J. R. Parker, "Algorithms for image processing and computer vision," *Willey Computer Publishing*, 1997, pp. 126-127.
- [51] T. C. Chen and K. L. Chung, "An efficient randomized algorithm for detection circles," *Computer Vision and Image Understanding*, Vol. 83, 2001, pp. 172-191.
- [52] L. S. Davis, "A Survey of Edge Detection Techniques," *CGIP*, Vol. 4, pp. 248-270.
- [53] K. R. Castleman, "Digital Image Processing," Prentice Hall International Editions, 1996 p. 41.

- [54] J. W. Goodman, "Use of a large-aperture optical system as a triple interferometer for removal of atmospheric image degradations, in Evaluation of motion-Degraded Images," *NASA Pub.*, SP-193, pp. 89-93, Dec. 1968.
- [55] E. M. Granger, "Restoration of images degraded by spatially varying smear, in Evaluation of motion-Degraded Images," *NASA Pub.*, SP-193, pp. 161-174, Dec. 1968.
- [56] D. L. Fried, "Optical resolution through a randomly inhomogeneous medium for very long and very short exposures," *J. Opt. Soc. Amer.*, 56, 1966, 1372-1379.
- [57] D. L. Fried, "Limiting resolution looking down through the atmosphere," *J. Opt. Soc. Amer.*, 56, 1966, 1380-1384.
- [58] R. E. Hufnagel and N. R. Stanley, "Modulation transfer function associated with image transmission through turbulent media," *J. Opt. Soc. Amer.*, 54, 1964, 52-61.
- [59] R. E. Hufnagel and N. R. Stanley, "An improved model for turbulent atmosphere, Restoration of Atmospherically Degraded Images," *NSF Summer Study Rep.*, 1966.
- [60] R. F. Lutomirski and H. T. Yura, "Modulation-transfer function and phase-structure function of an optical wave in a turbulent medium-1," *J. Opt. Soc. Amer.*, 59, 1969,
- [61] C. Seiler, R. L. Kirkeeide, and K. L. Gould, "Basic structure - function relations of the epicardial coronary vascular tree: basis of quantitative coronary arteriography for diffuse coronary artery disease," *Circulation*, vol. 85, no. 6, pp. 1987-2003, 1992.
- [62] M. J. Potel, J. M. Rubin, S. A. Mackay, A. M. Aisen, J. Al-Sadir, and R. E. Sayre, "Methods for evaluating cardiac wall motion in three dimensions using bifurcation points of the coronary arterial tree," *Investigative Radiology*, vol. 18, no. 1, Jan-Feb, pp. 47-56, 1983.
- [63] G Coppini, M. Demi, A. L'abbate, and G. Vallio, "Computational geometry of heart surfaces," *Computers in Cardiology, IEEE Computer Society*, pp. 293-296, 1989.

- [64] A. A. Young and P. J. Hunter, "Epicardial surface estimation from coronary angiograms," *Computer Vision, Graphics, and Image Processing*, vol. 47, pp. 111-127, 1989.
- [65] J. L. Coatrieux, M Garreau, S Ruan, and F Mao, "On motion analysis in medical imaging," *Innovation and Technology in Biology and Medicine*, vol. 15, no. 3, pp. 253-267, 1994.
- [66] J Meunier, M Verreault, J Lesperance, and M Bertrand, "Estimating epicardial dynamics from the coronary arterial tree motion in cineangiography," *Innovation and Technology in Biology and Medicine*, vol. 15, no. 3, pp. 282-292, 1994.
- [67] A. Wahle, E. Wellnhofer, I. Mugaragu, H.U. Sauer, H. Oswald, and E. Fleck, "Assessment of diffuse coronary artery disease by quantitative analysis of coronary morphology based upon 3-D reconstruction from biplane angiograms," *IEEE Trans. on Med. Imag.*, vol. 14, no. 2, pp. 230-241, 1995.
- [68] JHC Reiber, "How far are we in the discussion about 3-D versus 2-D QCA?" *International Journal of Cardiac Imaging*, vol. 15, pp. 355-356, 1999.
- [69] D. Marr and D. Hildreth, "Theory of edge detection," *Proc. Roy Soc, Ser. B*, vol. 207, pp. 187-217, 1980.
- [70] J. Canny, "A computational approach to edge detection," *IEEE Trans. PAMI*, vol. 8, pp. 679-697, Nov. 1986.
- [71] T. Elfving, J. O. Eklundh and S. Nyberg, "Edge detection using the Marr-Hildreth operator with different sizes," in *Int. Conf. On Pattern Recognition*, pp. 1109-1112, 1982.
- [72] W. Frei and C. C. Chen, "Fast boundary detection: A generalization and a new algorithm," *IEEE Trans. Comput.*, vol. 8, pp. 988-998, Oct. 1977.

- [73] F. M. Dickey, K. S. Shanmuugam, and J. A. Green, "An optimal frequency domain filter for edge detection in digital pictures," *IEEE Trans. Anal. Machine Intell.*, vol. PAMI-1, pp. 37-49, Jan. 1979.
- [74] J. W. Modestino, and R. W. Fries, "Edge detection in noisy images using recursive digital filtering," *Comput. Graphics Image Processing*, vol. 6, pp. 409-433, 1977.
- [75] V. Torre and T. A. Poggio, "On edge detection," *IEEE PAMI.*, vol. PAMI-8, pp. 147-163, Mar. 1979.
- [76] P. H. Eichel, E.J. Delp, K. Koral, and A. J. Buda, "A method for fully automatic definition of coronary arterial edges from cineangiograms," *IEEE Trans. Med. Imaging*, vol. 18, pp. 313-320, 1988.
- [77] K. Haris, S. N. Efstratiadis, N. Magkaveras, C. Pappas, J. Gourassas, and G. Louridas, "Model based morphological Segmentation and labeling of coronary artery angiograms," *IEEE Trans. Med. Imaging*, vol. 18, pp. 1003-1015, 1999.
- [78] N. Ezquerro, S. Capell, L. Klein, and P. Duijves, "Model-Guided Labeling of Coronary Structure," *IEEE Trans. Med. Imaging*, vol. 17, no. 3, Jun. pp. 429-441, 1998.
- [79] R. C. Chan, W. C. Karl, and R. S. Lees, "A New Model-Based Technique for Enhanced Small-Vessel Measurements in X-Ray Cine-Angiograms," *IEEE Trans. Med. Imaging*, vol. 19, pp. 243-255, Mar., 2000.
- [80] Y. Sun, "Automated identification of vessel contours in coronary arteriograms by an adaptive tracking algorithm," *IEEE Trans. Med. Imaging*, vol. 8, pp. 78-88, Mar., 1989.
- [81] S. Tamura, K. Tanaka, S. Ohmori, K. Okazaki, A. Okada, and M. Hoshi, "Semiautomatic leakage analyzing system for time series fluorescein ocular fundus angiography," *Pattern Recognition*, vol. 16, no. 2, pp. 149-162, 1983.
- [82] Y. Tolia and S. Panas, "A fuzzy vessel tracking algorithm for retinal images based on fuzzy clustering," *IEEE Trans. Med. Imaging*, vol. 17, pp. 263-273, Apr., 1998.

- [83] S. Chaudhuri, S. Chatterjee, N. Katz, M. Nelson, and M. GOLDBAUM, "Detection of blood vessels in retinal images using two-dimensional matched filter," *IEEE Trans. Med. Imaging*, vol. 8, pp. 263-269, 1989.
- [84] A. Hoover, V. Kouznetsova, and M. Goldbaum, "Locating Blood Vessels in Retinal Images by Piecewise threshold probing of a matched filter response," *IEEE Trans. Med. Imaging*, vol. 8, pp. 203-210, 2000.
- [85] Y. Sun, R. J. Lucariello, and S. A. Chiaramida, "Directional Low-Pass Filtering for Improved Accuracy and Reproducibility of Stenosis Quantification in Coronary Arteriograms," *IEEE Trans. Med. Imaging*, vol. 14, No. 2, pp. 242-248, Jun., 2000.
- [86] R. C. Gonzalez, and R. E. Woods, "Digital Image Processing," *Addison-Wesley Publishing Company*, pp 81-125, 1992.
- [87] S. Mallat, "A Theory fro Multiresolution Signal Decomposition: The Wavelet Representation," *IEEE Trans.PAMI*, vol. 11, pp. 647-693, 1999.
- [88] P. P. Vaidyanathan, "Multirate Systems and Filter Banks", *Prentice Hall, Inc.*, 1993.
- [89] L. Cohen, "Time-Frequency Distributions - A Review," *Proc. IEEE, Vol. 77*, pp. 941-981, 1989.
- [90] M. Kass, A. Witkin, and D. Terzopoulox, "Snakes: Active Contour Models," *Int. J. Comput. Vis*, vol. 1, pp. 321-331, 1987
- [91] C. Xu, J.L. Prince, "Snakes, shapes, and Gradient Vector Flow," *IEEE Trans, on Image Process.* pp. 359-369, Mar., 1998.
- [92] D. J. Williams and Mubarak, "A Fast Algorithm for Active Contours and Curvature Estimation," *CVGIP:Image Understanding*, vol. 55, No. 1, pp. 14-16, 1992.

VITA

Chih-Yang Lin received the Master degree in computer science and engineering from Yuan-Ze University, Taiwan, in 1996. He was an assistant manager at R&D department of Chilong Co. Ltd. from 1988 to 1993. He was a senior engineer at Motorola Electronics Ltd. in Taiwan from 1993 to 1996. Currently he is a Ph.D candidate in computer and information science at the National Chiao-Tung University. His current research interests include medical imaging, signal process, and wavelets.



Publication List of Chih-Yang Lin

A. Jurnal papers

Accepted or published :

1. Chih-Yang Lin, Yu-Tai Ching, Betty A.Wu-Hsieh, "A Computer Method for ELISA Spot Assay Analysis," *Optical Engineering*. (**Accepted, SCI, IF:0.877**)
2. Chih-Yang Lin, Yu-Tai Ching, "Extraction of Coronary Arterial Tree Using Cine X-Ray Angiograms," *Biomedical Engineering Applications, Basis Communications*, (**Accepted, EI**)
3. Hsiu-Jung Lo, Jang-Shiun Wang, Chih-Yang Lin, Chia-Geun Chen, Tin-Yi Hsaio, Chia-Tung Hsu, Chia-Li Su, Ming-Ji Fann, Yu-Tai Ching, and Yun-Liang Yang, "Efg1 Involved in Drug Resistance through Regulating the Expression of ERG3 in *Candida albicans*," *Antimicrobial Agents and Chemotherapy*, Vol. 49. No, 3, Mar., 2005, pp. 1213-1215. (**SCI, IF:4.246**)
4. Yu-Tai Ching, Shyh-Jye Chen, Chew-Laing Chang, Chih-Yang Lin, Yu-Hsian Liu, "Finding the Mitral Annular Lines from 2D+1D Precordial Echocardiogram Using Graph-Search Technique," *IEEE Transactions on Information Technology in Biomedicine*, Vol. 8, No. 1, 2004, pp. 1-4. (**SCI, IF:1.274**)
5. Chih-Yang Lin, and Yu-Tai Ching, "A Robust Images Hiding Method Using Wavelet Techniques," *Journal of Information Science and Engineering*. (**Accepted, SCI, IF:0.140**)
6. Chi-Feng Lin, Chih-Yang Lin, "A new approach to a high precision 3-D measuring system," *Image and Vision Computing* 17, 1999, pp. 805-814. (**SCI, IF:1.169**)

Submitted or Revised:

7. Chih-Yang Lin, Wen-Jeng Lee, Shyh-Jye Chen, Ching-Hwa Tsai, Jei-Han Lee, Chia-Hung Chang, Yu-Tai Ching, "A Computer Method to Remove Grid Texture and Moiré Pattern Artifacts in Computed Radiographic Images," *IEEE Transactions on Information Technology in Biomedicine*, (2005/6, **SCI, IF:2.305**)
8. Chih-Yang Lin, and Yu-Tai Ching, Yun-Liang Yang, "A Method to Extract the Lanes and the Bands in the Pulsed-field Gel Electrophoresis (PFGE) Images and Remove the Vector from Lanes," *IEEE Transactions on Information Technology in Biomedicine*. (2002/10, **Revised, SCI, IF:1.274**)
9. Yu-Tai Ching, Chih-Yang Lin, and Shih-Shen Yang, "Medical Image Segmentation using the Shortest Path Technique," *Optical Engineering*. (2004/8, **Revised, SCI, IF:0.877**)
10. Yu-Tai Ching, Chih-Yang Lin, Kheng-Chong Tan, Kiang-Long Lau, Cheng-Hsiu Yang, and Chao-An Lin, "Rectangular Meshes Construction of Cylindrical Structure Organ from Computed Tomographic Images," (2004, **EI**)
11. Min-Jin Wu, Chih-Yang Lin, Yu-Tai Ching, Ann-Shyn Chiang, Chang-Huain Hsieh, "Segmentation of the Mushroom body in the Insect Brain in Confocal Microscopic Images", *Computer Methods & Programs in Biomedicine*. (2002/12, **Revised, SCI, IF:0.724**)

B. Conference papers

Published :

1. Yu-Tai Ching, Chih-Yang Lin, C. H. Yang, and C. A. Lin, " Rectangular Meshes Construction of the Human Urethra Using 3-D GVF Snakes," *SPIE Medical Imaging*, Feb. 2004, pp. 539-549. (**EI**)

2. Chih-Yang Lin, and Yu-Tai Ching, "Reconstruction of the human brain from MRI-T1 using 3-D morphology and snake," *SPIE Medical Imaging*, Feb. 2002, pp. 317-323. (EI)
3. Ming-Jin Wua, Chih-Yang Lin, and Yu-Tai Ching, "Segmentation of confocal microscopic image of insect brain," *SPIE Medical Imaging*, Feb., 2002, pp. 1563-1570. (EI)
4. Wei-Zen Cheng, Kue-Sai Yen, Chih-Yang Lin, Yu-Tai Ching, Yun-Liang Yang, "Comparing lanes in the pulsed-field gel electrophoresis (PFGE) images," *23rd annual international conference of the IEEE engineering in medicine and biology society*, 2001, pp. 2911-2913. (EI)
5. Chih-Yang Lin, Yu-Tai Ching, A.Wu-Hsieh, "A method to extract spots from the image of the ELISA (Enzyme-Linked Immunosorbent Assay) spot assay," *23rd annual international conference of the IEEE engineering in medicine and biology society*, 2001, pp. 2549-2552. (EI)
6. Chih-Yang Lin and Yu-Tai Ching, "Extraction of coronary arteries by using a sequence of X-Ray angiographic images," *Proceeding of SPIE* Vol. 4322, 2001, pp.1322-1328. (EI)
7. Chi-Fang Lin and Chih-Yang Lin, "A New Approach to a High Precision 3-D Measuring System," *Conference on Computer vision, Graphics, And Image Processing*, 1996.